INFRARED, OPTICAL, AND LUMINESCENT
PROPERTIES OF QUASI-ONE-DIMENSIONAL ORGANIC
CHARGE TRANSFER SALTS AND POLYMERS

By

JANICE LYNN MUSFELDT

A DISSERTATION PRESENTED TO THE GRADUATE SCHOOL
OF THE UNIVERSITY OF FLORIDA IN PARTIAL FULFILLMENT
OF THE REQUIREMENTS FOR THE DEGREE OF
DOCTOR OF PHILOSOPHY

UNIVERSITY OF FLORIDA

1992

To David

ACKNOWLEDGMENTS

In addition, I am also in the debt of Dr. J. Ruiz, Prof. J.R. Reynolds, J. Wang, and Prof. M. Pomerantz for the preparation of the various polymers used in these studies. A special thanks is due to John Reynolds for his interest, encouragement and support in the electro–luminescent polymer project. I have also greatly appreciated the use of the fluorimeter in the laboratory of Prof. K. Schanze for the steady state and time resolved photo–luminescent measurements. Nancy Thornton was a big help with the aforementioned measurements.

I have greatly appreciated the efforts of the technical staff members in the physics department machine shop, especially Ron Spencer and Ed Storch, the engineers in the condensed matter group for the reliable supply of liquid helium, and the staff in the electronics shop, particularly Larry Phelps.

I would also like to take this opportunity to thank my parents for their support, and my brother for his encouragement and practical advice.

A very special thanks is due to my husband, David, whose encouragement and understanding were essential to the completion of this work.

TABLE OF CONTENTS

Abstract of Dissertation Presented to the Graduate School
of the University of Florida in Partial Fulfillment of the
Requirements for the Degree of Doctor of Philosophy

INFRARED, OPTICAL, AND LUMINESCENT
PROPERTIES OF QUASI-ONE-DIMENSIONAL ORGANIC
CHARGE TRANSFER SALTS AND POLYMERS

By

Janice Lynn Musfeldt

December 1992

Chairman: David B. Tanner
Major Department: Chemistry

Polarized infrared and optical reflectance spectroscopies were used to study the structural phase transitions in two quarter-filled semiconducting organic charge transfer salts, N-propylquinolinium$(TCNQ)_2$ and N-dimethyl thiomorpholinium$(TCNQ)_2$; and two half-filled salts, Potassium-TCNQ and Rubidium-TCNQ.

The spectra of $NPrQn(TCNQ)_2$ display characteristics common to quarter-filled charge transfer salts. Various cluster models were applied to describe the electron-phonon coupling at 300 K. The weakly metallic transport properties above T_c in $NPrQn(TCNQ)_2$ are attributed to the uniform charge distribution within the tetramer and the high degree of overlap between the intra- and inter-tetramer charge transfer bands. Despite evidence for a larger intra-tetramer transfer integral below T_c, the transport properties are dominated by charge localization, as evidenced by the doublet pattern in the vibrational features.

In the $DMTM(TCNQ)_2$ salt, measurements were made on several faces of large single crystal samples. The electron-phonon coupling behavior was analyzed within

the framework of both an isolated dimer model and a twofold commensurate charge density wave model. Our data, polarized close to the b crystallographic axis, do not support the idea that the unusual transport properties of semiconducting DMTM(TCNQ)$_2$ are caused by low-energy inter-chain charge transfer.

The spectra of two closely related half-filled salts, K-TCNQ and Rb-TCNQ, were also investigated. The A_g features change gradually with temperature in the potassium sample, whereas in the rubidium sample little contrast was observed. The far infrared A_g vibrational features in K-TCNQ continue to change gradually above T_c. In contrast, the A_g vibrational modes in Rb-TCNQ vanish almost completely at T_c. These observations suggest that while the phase transition is strongly first-order for Rb-TCNQ, it is closer to second-order in K-TCNQ. The temperature dependence of the lattice modes is also discussed.

Finally, optical absorption, photo- and electro-luminescence measurements were performed on a series of semiconducting polymers based upon phenylene and thiophene. Visible light emission was observed from two materials with discrete emitter units, suggesting that intra-chain mobility of the charge defect may not be essential to radiative recombination of the exciton.

CHAPTER I
INTRODUCTION

This document describes the investigation of the spectroscopic properties of quasi-one-dimensional materials. It may be divided into two main components: the infrared and optical properties of semiconducting organic charge transfer salts, and the absorption, photo- and electro-luminescence properties of several phenylene and thiophene based polymers.

Quasi-One-Dimensional Organic Charge Transfer Salts

The organic molecule 7, 7', 8, 8' tetracyanoquinodimethane (TCNQ) was first synthesized by researchers at E.I. du Pont de Nemours and Company in 1960.[1] Neutral TCNQ molecules stack in a columnar manner to form a semiconducting, diamagnetic molecular crystal. However, the TCNQ molecule has a high electron affinity, and it is often involved in the formation of organic charge transfer salts.[2] These intrinsically conducting, quasi-one-dimensional organic salts have been the subject of intense study for the past three decades.

In recent years, a great variety of TCNQ salts have been synthesized with various donor molecules. The chemical identity of the donor cation and the stoichiometry of the salt determines the population of the conduction band. The ratio of donor to acceptor molecules and the degree of static charge transfer affect the details of the crystal structure. For example, simple 1:1 salts, such as K- or Rb-TCNQ, have one unpaired electron on each TCNQ molecule. Because of the large on-site Coulomb repulsion (Hubbard U) between the electrons, these materials display very low dc electrical conductivity at room temperature. Hence, they are often referred to as

"Mott-Hubbard" insulators. Electronically, they consist of either completely filled or completely empty bands. Thus, electrical conduction can occur only by thermal activation. For the complex salts, the most common stoichiometric ratios are 1:2 or 2:3. The behavior of these salts is more complicated than the 1:1 insulators, as they can be insulating or conducting.

The strong anisotropy in these materials, from which the most interesting physical properties derive, is known to result directly from their distinctive structural architecture. In these materials, the TCNQ molecule acts as a monomer repeat unit, stacking in quasi-one-dimensional columns or chains. The columns are commonly segregated on the basis of donor or acceptor species. Within these stacks of TCNQ molecules, the distribution of molecules can be uniform or arranged in units of "dimers," "trimers," "tetramers," or "n-mers."[3] The structural overlap of the TCNQ molecules in the stack determines the overlap of the electronic wavefunction. Consequently, a uniform distribution of TCNQ molecules usually results in metallic properties, while a distorted stack has semiconducting properties.[4]

Many recent studies of quasi-one dimensional organic materials have concentrated upon structural and the metal-insulator phase transitions.[5-12] Detailed examination of the systematic transport, structural and spectral changes in the neighborhood of the critical temperature (T_c) has proved to be a useful tool in understanding various property changes through the phase transition. Spectroscopic methods have been used with particularly good success to probe the mechanisms and characteristics of structural phase transitions by understanding changes in electron-phonon coupling and the semiconducting gap.

Not only is it of fundamental scientific interest to understand the driving mechanism for these metal-insulator transitions, but it is of practical interest as well. With the understanding of the driving forces of the Peierls transition, it may become pos-

sible to inhibit such transitions, engineering conducting organic materials without metal-insulator transitions. Repression of a metal-insulator transition may lead to organic materials with metallic or superconducting properties at low temperature.

NPrQn(TCNQ)$_2$, DMTM(TCNQ)$_2$, K-TCNQ, and Rb-TCNQ have particularly interesting structural phase transitions. The NPrQn salt undergoes a typical metal-insulator transition at T_c,[13,14] while the dc conductivity of DMTM salt actually increases below T_c.[15,16] The K- and Rb-salts are interesting because of their chemical similarity and simplicity, combined with their strikingly different behaviors at T_c.[6,17] Figure 1 displays the chemical structure of the TCNQ molecule and the various cations used in this study. Each of these materials was available in high quality, single crystal form.

In order to provide further information on the nature of the high- and low-temperature phases as well as the structural phase transitions, we have investigated the infrared and optical properties of NPrQn(TCNQ)$_2$, DMTM(TCNQ)$_2$, K-TCNQ, and Rb-TCNQ. Spectroscopic methods are well suited to the study of highly anisotropic materials such as the TCNQ charge transfer salts, providing information on the electronic charge transfer and localized excitations at high energies, as well as the vibrational features, electron-phonon coupling, and lattice and libron modes at lower energies.[4,18,19,20,21] Infrared spectroscopy is an especially sensitive probe of the changes which accompany a structural phase transition, as the vibrational structure is a sensitive indicator of lattice and electronic variations. Our results, in particular the electron-phonon coupling in the chain direction, have been treated within the framework of molecular cluster models (such as the isolated dimer by Rice et al.[22] and the isolated tetramer model by Yartsev[23]), and in the case of DMTM(TCNQ)$_2$, a model for commensurate charge density waves in extended linear chains, initially devised by Rice[24] and developed further by Bozio et al.[25] In these models, the totally symmetric

A_g modes of the TCNQ molecule, normally infrared inactive, become optically active via coupling, either through a charge transfer process or with a charge density wave. Because of this coupling, these modes show unusually large oscillator strength, with polarization along the TCNQ stacking direction. Emphasis has been placed on the correlation of the spectral properties above and below T_c with available structural, transport, and band structure data, in order to obtain a greater understanding of the characteristics and mechanism of the structural phase transitions in these four materials.

In addition, our data on NPrQn(TCNQ)$_2$ is compared to previous spectroscopic results on the closely related, quinoid based compounds such as Qn(TCNQ)$_2$ and (NMP)$_x$(Phen)$_{1-x}$(TCNQ) by McCall et al.[26] We also compare our results for DMTM(TCNQ)$_2$ with the well-studied N-methyl-N-ethyl morpholinium(TCNQ)$_2$ system, MEM(TCNQ)$_2$.[22,27,28,29] The counterions in these two aforementioned materials are closely related, the most notable difference being the more polarizable sulfur atom on the DMTM ring, which is known to be responsible for many interesting two-dimensional effects in the family of ET salts.[30] These comparisons illustrate the important role of the cation in determining the transport and spectroscopic properties of quasi-one-dimensional materials.

For the half-filled salts (K- and Rb-TCNQ), we concentrate our discussion on a comparison between the two samples, once again illustrating the important effect of the counterion identity in these salts. Such a comparison is valuable in light of the recent and very thorough measurements of the temperature dependence of the near-infrared and visible spectra on these same crystals, by Okamoto et al.[6] Along the TCNQ stacking direction in the low-temperature phase, they clearly resolve the "two-oscillator" nature of the charger transfer (U-band) and follow its evolution through T_c. The strong temperature dependence of the U band in the near infrared was antici-

pated to result in interesting temperature dependence of the electron-phonon coupling and lattice modes in the middle and far infrared frequency regime, respectively. In addition to their work on the near-infrared and optical regime, the aforementioned authors[6] also examine changes in the electron-phonon coupling by monitoring changes in the CN stretching mode (A_g symmetry) as a function of temperature. To complement their work, we have done systematic measurements in the complete infrared frequency range. This is the first far-infrared work on the well studied K- compound. We are presently unaware of any infrared measurements on single crystal Rb-TCNQ samples. Here, our discussion will concentrate upon the far-infrared results in these two materials.

Furthermore, the combined study of these quasi-one-dimensional salts will highlight the importance of electron correlation effects, which are expected to be large. In addition, I hope to briefly discuss the role of disorder in the structural phase transitions of these materials.

Luminescent Polymers

Recently, there has been a great deal of interest in the photo-physical properties of conjugated polymers, particularly since the discovery in 1991 of visible light emission from a poly-phenylene-vinylene (PPV) based diode.[31,32] Blue-green light emission has also been reported for devices based upon both poly-p-phenylene (PPP) and poly-3-alkylthiophene, suggesting that electro-luminescence of conjugated polymers may be a more common phenomena than originally anticipated.[33,34] Based upon this supposition, researchers have begun to search for other potential light emitting polymers. Materials which can support the polaron or bipolaron defect state, thought to be important in the mechanism of visible light emission, are prime candidates for such a study. In this work, we examine several materials in which the bipolaron defect is electronically isolated.

The field of electro-luminescent polymers is relatively new, and thus many fundamental questions are not well understood. Many are long-term problems, and beyond the scope of this work; however, they are still interesting to consider. They include a concerted discussion of the mechanism of light emission, and a correlation of chemical structure to photo- and electro-luminescence properties—most specifically, emission frequency and efficiency.

The work detailed in this dissertation was motivated by several goals. The first was to characterize the absorption and emission properties of several potential electro-luminescent materials. Such characterization is a necessary preliminary for the investigation of electro-luminescence.

A second goal was the search for new electro-luminescent polymers amongst this class of materials with discrete emitter units. It is of particular interest to find a candidate material for use in a blue-emitting diode device. Blue-emitting materials are rare and have been reported primarily in inorganic materials.

It is also of general interest to begin to develop qualitative ideas for what aspects of the structure result in photo- as well as electro-luminescence. To this end, we have studied several materials; the chemical structure of the various polymer repeat units are displayed in Fig. 2, Fig. 3 and Fig. 4. These materials are primarily based upon poly-meta-phenylene, poly-para-phenylene, or a symmetrically substituted (2-thienyl)phenylene repeat unit.

The materials in Fig. 2 and Fig. 3 and allow the systematic examination of a series of discrete emitter units, establishing a fundamental link between the conjugation of the emitter unit and the related absorption and emission properties. It is also of interest how these chemical considerations affect the photo- and electro-luminescent lifetime and efficiency.

The side chains of the 1,4-bis(2-thienyl)phenylene (PBTB) based polymers Fig. 4 have been selected with a different goal in mind. Here, we seek to alter main-chain conjugation and the band gap of the polymer with the use of side chains. Two main effects are envisioned. First, the electron-donating or with-drawing character of the side chains may alter the character of the main chain conjugation, thus increasing or decreasing the semiconducting gap. Secondly, the hexyl side chains may cause steric hindrances, which twist the main-chain backbone from its more planar configuration, thus isolating the emitter unit; the increased ring torsion angle would also affect the size of the band gap. In contrast, the dodecyloxy side chains produce very little steric hindrance near the chain backbone.

It is a final goal in this study to demonstrate that electro-luminescence in polymers is not an isolated or rare phenomena, and that within certain limitations of chemical structure, photo- and electro-luminescence are intrinsic properties of many conjugated organic polymers.

Dissertation Outline

There are two main thrusts to this dissertation: (1) the infrared and optical investigations of quasi-one-dimensional organic charge transfer salts and (2) photo- and electro- luminescence measurements on various types of semiconducting polymers. Consequently, several Chapters (2, 3, 4, and 8) will be divided into separate sections, to address these two topics in an organized manner.

This document is organized in the following way. Chapter 2 presents the theoretical methods which pertain to the analysis of the results contained in this dissertation. Chapter 3 outlines previous experimental work in the areas of quasi-one-dimensional charge transfer salts and luminescent polymers, while Chapter 4 discusses the experimental apparatus and equipments used in these investigations. For continuity, the Results and Discussion of the quarter-filled charge transfer salts are presented in

Chapter 5, while the Results and Discussion of the half-filled charge transfer salts are given in Chapter 6. The Results and Discussion pertaining to the luminescent polymers are given in Chapter 7. The Conclusions are presented in Chapter 8.

TCNQ

N-PrQn

DMTM
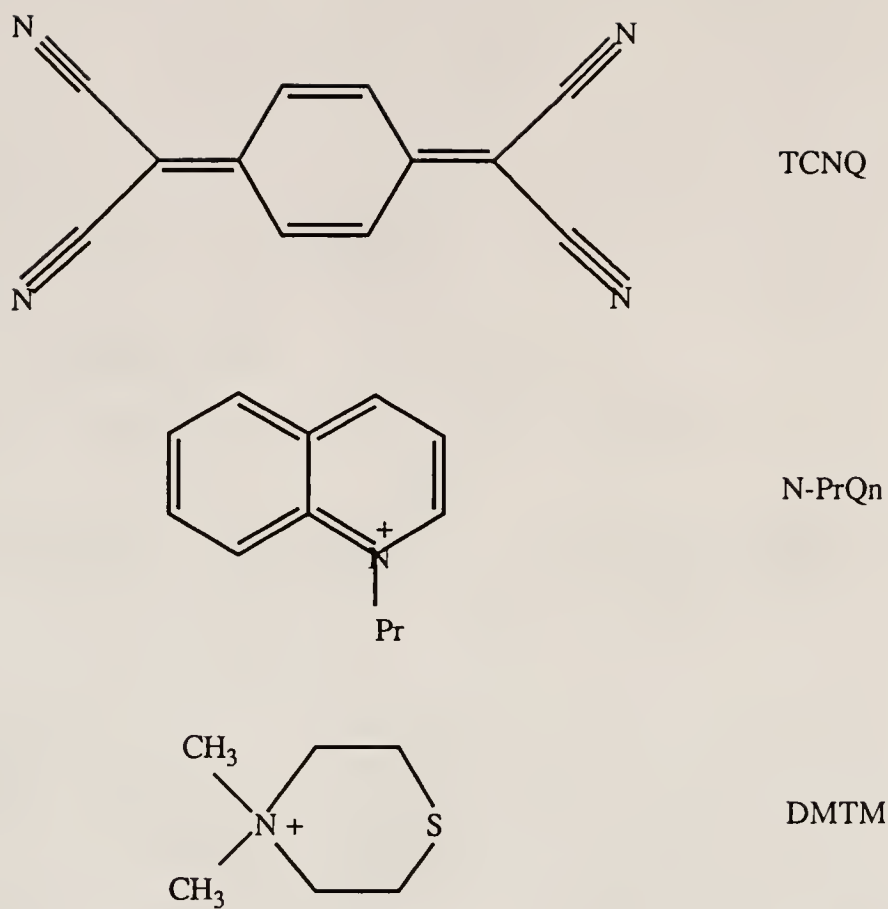
Fig. 1. Chemical structure of the TCNQ molecule and the various cations used in this study.
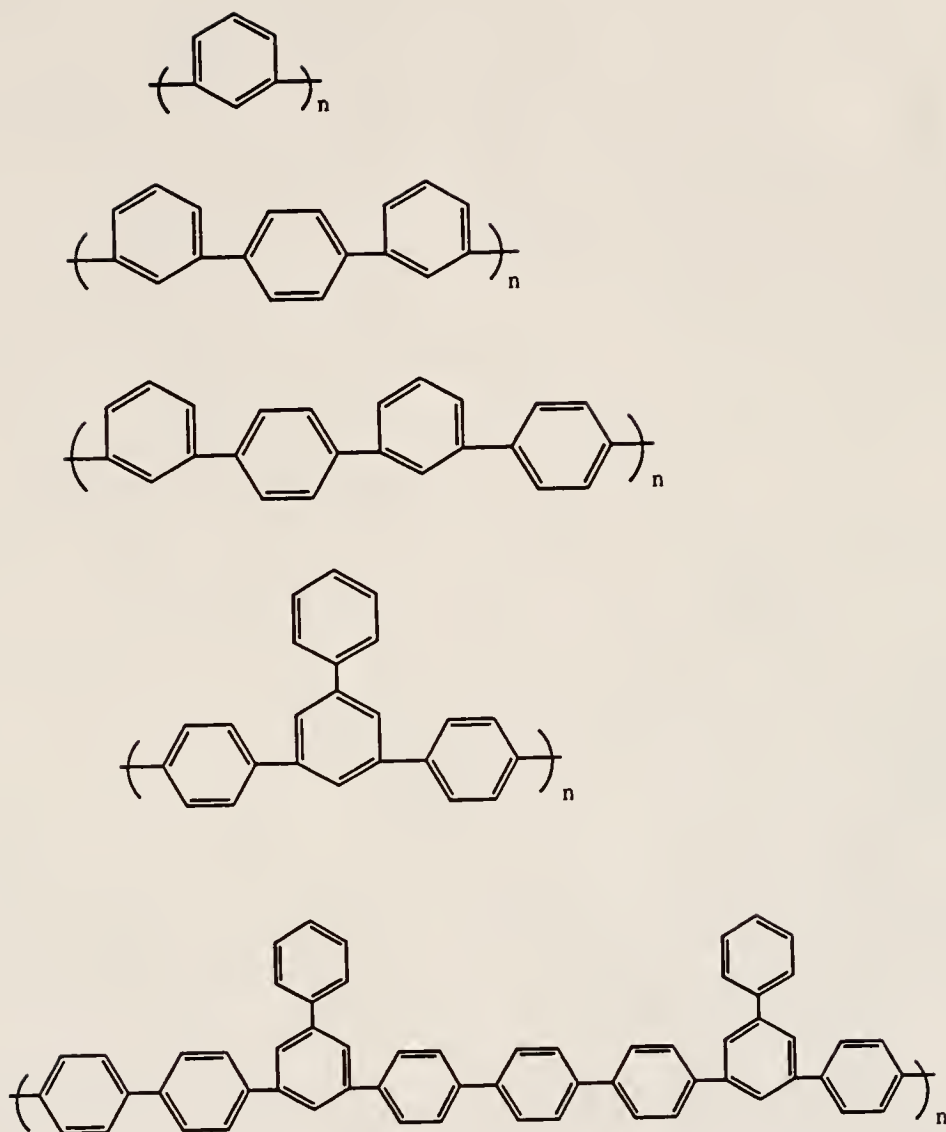
Fig. 2. Chemical structure of the phenylene based polymer repeat units used in this study.
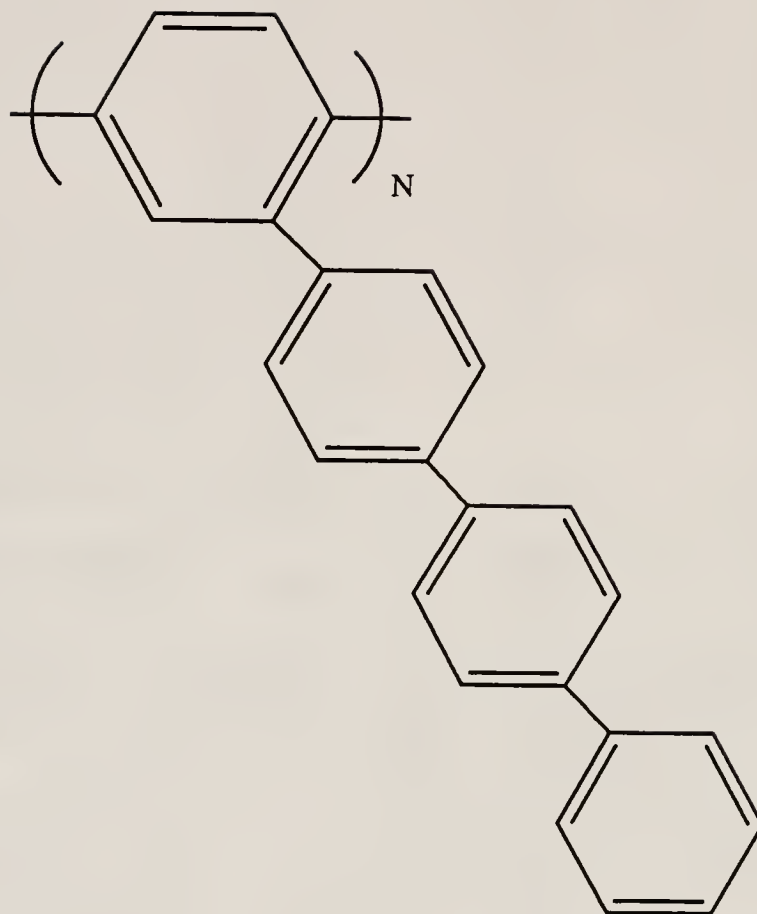
Fig. 3. Chemical structure of the quarterphenylene polymer repeat unit used in this study.

$$R = \text{--}C_6H_{13} \ \text{ or } \ \text{--}OC_{12}H_{25}$$
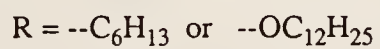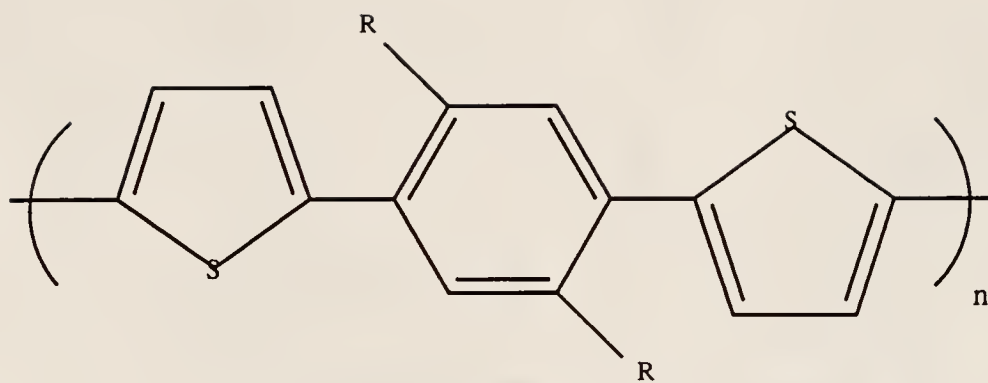
Fig. 4. Chemical structure of the 1,4-bis-(2-thienyl)phenylene polymer repeat unit and side groups used in this study.

CHAPTER II
THEORY

Organic Charge Transfer Salts

Due to their quasi-one-dimensional nature, organic charge transfer salts are a class of compounds which manifest many interesting aspects of one-dimensional physics. Consequently, the theoretical models which describe these interactions are an important component of this dissertation.

In these materials, interactions involving unpaired electrons in the highest occupied molecular orbital have especially important consequences.[35,36,37] The tight-binding model is often used to obtain a band structure from the overlap of TCNQ frontier molecular orbitals, while the extended Hubbard model describes the importance of Coulomb interactions in the chain. In the case of a highly correlated lattice, the tight-binding band is split into two bands, separated by a wide gap on the order U, the on-site Coulomb repulsion energy. Finally, the Peierls model serves to illustrate the the effects of electron-phonon coupling in these materials in two ways. First, the physical origin of the Peierls transition is a Kohn anomaly at $2k_F$ which causes band splitting and introduces a semiconducting band gap between the valence and conduction band. Secondly, the accompanying lattice distortion results in the formation of a charge density wave, which couples to several of the TCNQ vibrational modes. The final pages of this section detail several isolated cluster models of electron-molecular vibrational coupling; the accurate description of this coupling process for TCNQ, TMTSF, and ET based salts is still an active area of research.

Hubbard Model

The extended Hubbard Hamiltonian for a one dimensional band[38] is

$$H = t \sum_{i,\sigma} (c^{\dagger}_{i+1,\sigma} c_{i,\sigma} + c^{\dagger}_{i,\sigma} c_{i+1,\sigma}) + \frac{1}{2} \sum_{i,\sigma} U n_{i,\sigma} n_{i,-\sigma} + \frac{1}{2} \sum_{i \neq j} V_{i-j} n_i n_j. \qquad (1)$$

Here, $c^{\dagger}_{i,\sigma}$ and $c_{i,\sigma}$ are the creation and annihilation operators for an electron with spin σ on site i, respectively, and $n_{i,\sigma} = c^{\dagger}_{i,\sigma} c_{i,\sigma}$ is the number operator for site i.

The first term in Eqn. (1) is the "tight-binding" or "hopping" term. A complete discussion of the tight-binding method is presented elsewhere.[39] Briefly, the tight-binding model describes the overlap of molecular orbitals and subsequent band formation as a linear combination of atomic orbitals. As the TCNQ charge transfer salts are essentially molecular in nature, the tight-binding approximation is a reasonable starting point from which to think about the band structure. The tight-binding wavefunctions have the form

$$\psi(r) = \sum_R e^{ik \cdot R} \phi(r - R), \qquad (2)$$

where $\phi(r)$ is a linear combination of localized atomic wavefunctions,

$$\phi(r) = \sum_n b_n \psi_n(r), \qquad (3)$$

where $\psi(r)$ is a localized atomic wavefunction. In these equations, R is the set of all Bravais lattice vectors. Note that the wavefunction in Eqn. (2) satisfies the Bloch condition

$$\psi(r + R) = e^{ik \cdot R} \psi(r). \qquad (4)$$

The tight-binding energy bands take on the form

$$E(k) = 2t\cos(ka) + const,\tag{5}$$

where a is the interatomic spacing and t is the transfer integral, given by

$$t = \int \phi_i H \phi_{i+1} d\tau.\tag{6}$$

Eqn. (5) leads to the definition of the one dimensional bandwidth as $4t$. When the overlap of the basis functions is large, the bandwidth is large, and the mean velocity of an electron moving through the crystal is high. In this model, the higher energy atomic levels broaden into bands, while for the deep levels, the overlap is not of significant magnitude for band formation. Hence, the tight-binding model represents a very localized picture of a solid while at the same time, it preserves the Bloch condition of periodic wave functions.

It is well known that the tight-binding model is inappropriate for many systems because of the neglect of all but the nearest neighbor overlap integrals, the independent electron approximation, and the model's inability to treat cases in which there is a large on-site or near-neighbor Coulomb interaction. For strongly correlated systems such as charge transfer salts, the interaction terms in the Hubbard Hamiltonian, Eqn. (1), become important. Due to the difficulty of the fully correlated problem on an extended lattice, it is necessary to consider these problems in terms of limiting cases. Hence, the effect of electron correlations will be discussed with reference to the zero bandwidth approximation and the noninteracting dimer case.[38,22]

Because there is a great deal of evidence that the on-site and nearest-neighbor electrostatic interactions are much greater than the bandwidth in many TCNQ compounds, the zero bandwidth approximation[38] is a very important limiting case of the

full Hamiltonian (Eqn. (1)). In the zero bandwidth approximation, the ground state of the system is determined by minimizing

$$H = \frac{1}{2} \sum_{i \neq j} V_{i-j} n_i n_j \tag{7}$$

subject to the condition

$$\rho N = \sum_i n_i, \tag{8}$$

where ρ is the band filling and N is the total number of sites in the chain. Here, the on-site Coulomb term was also eliminated via the following reasoning: for $\rho < 1$, the electrons localize as one per site, thus eliminating a substantial contribution from the U term. For the case of $\rho > 1$, holes are the carrier of interest, and then the aforementioned condition is satisfied.

The ground state of the system has been obtained for a particular class of potentials which satisfy the following two conditions

$$V_n \to 0 \quad as \ n \to \infty, \tag{9}$$

and

$$V_{n+1} + V_{n-1} \geq 2V_n \quad \text{for all } n > 1. \tag{10}$$

Under these conditions, as well as the limitation of ρ being a rational fraction, the electrons are found to have a periodic arrangement within the chain. In fact, this arrangement can be regarded as a generalized Wigner lattice. These arrangements are also predicted to give rise to lattice distortions, such as dimers, trimers or tetramers.

Working with the idea of a distorted chain, we can examine the physics of different kinds of interactions. For example, Fig. 5 displays the progression from an isolated

dimer to that of a strongly interacting, large U, dimer. This diagram displays the increased band width associated with a larger inter-dimer transfer integral, t', and finally the effect of strong on-site electron-electron interactions, which result in a gap of order U, the on-site Coulomb repulsion energy.

First we turn our attention to the noninteracting dimer. Rice et al.[22,40] have discussed the case of the completely isolated quarter- and half-filled dimer. In the case of one electron per dimer, as shown in the left-most picture of Fig. 5, the Hamiltonian is simply

$$H = -t(c_1^\dagger c_2 + c_2 c_1^\dagger) \tag{11}$$

due to the absence of correlation effects and spin considerations. Eigenvalues of the interacting system are at $E_\pm = \pm t$. Note that this model contains only one transfer integral, so it is expected that this model will not provide a completely realistic solution for the extended chain. However, inclusion of a finite bandwidth is expected to preserve many of the rough features, as shown for the weakly coupled picture in Fig. 5. Here, inclusion of a finite inter-dimer overlap integral results in a broadening of the energy levels into bands of width $2t'$, where t' is the inter-dimer transfer integral. If the band motion is stronger still, the inter-dimer transfer integral increases even more (as shown in the strongly interacting picture in Fig. 5), until finally, $t = t'$, which is the tight-binding picture. The electron-phonon coupling within these isolated dimer models will be detailed in a subsequent section.

In the case of very large U (compared to t), the electrons are unlikely to doubly occupy sites. Hence, a gap develops which separates the one electron states from the two electron states. The gap between the lower and upper Hubbard bands is on the order of the on-site Coulomb repulsion, U. This localizes the electrons (one on each TCNQ molecule) in the chain. It is the tight-binding band structure modified by a large U consideration that is depicted in the final picture in Fig. 5.

Ultimately, it is the relative importance of electron-electron correlation effects (the size of U and also V) relative to the bandwidth ($4t$) which is the important consideration in the behavior of many quasi-one-dimensional charge transfer salts.[41,37] For example, it is the relative magnitude of the aforementioned terms combined with the band filling which determines the periodicity of the reciprocal lattice vector which couples the highest occupied states, and thus the nature of the Peierls distortion. This will be detailed in the next section. In metallic compounds, screening is also an important consideration.

Peierls Transition

Although the dc conductivity for many quasi-one-dimensional charge transfer salts increases with decreasing temperature to a certain point, the low-temperature dc conductivity of most such materials is low due to the onset of one or more phase transitions which culminate in a semiconducting ground state. The Peierls transition[42,35,36,43] is the most common type of metal-insulator transition.

The Peierls distortion is generally introduced by considering a one-dimensional lattice of atoms with uniform spacing, a. Peierls has shown[42] that a one dimensional electron gas at T $= 0$ K with finite electron-phonon coupling is unstable to a structural distortion of the form

$$u_n = na + u_0 \sin(2nk_F a + \phi), \tag{12}$$

with the constraint that the distortion, u_0, is much less than the lattice constant, a. Here, u_n designates the position of the nth atom.

Because the distortion occurs at k_F, the total electronic energy of the system is reduced as the band splits. The filled states are shifted lower in energy and the unfilled states are shifted higher in energy. Thus, a semiconducting gap is opened at

the Fermi surface. The size of the gap is given as

$$E_{gap} = 2te^{-(\frac{1}{\lambda})},$$ (13)

where λ is the dimensionless electron-phonon coupling constant. The progression of the band and geometric structure is diagrammed in Fig. 6 for the case of a half-filled band with no Coulomb interactions. Here, the $2k_f$ lattice distortion at reciprocal lattice vector $\frac{\pi}{2a}$ results in a doubling of the spatial periodicity and a reduction (by one half) of the Brillouin zone.

The formation of the charge density wave ground state is one of the most important consequences of the Peierls transition. This occurs in the following way. In the case of a half-filled band, the structural distortion of the uniform chain causes the grouping of sites into dimeric units (Fig. 6). This pairing alters the charge density along the chain. Starting from a uniform distribution of charge, the unpaired electrons contract to form regions of increased and decreased charge density. In an infinite system, the charge density is given by

$$\rho(r) = \rho_0 + \rho_1 \cos(q \cdot r + \phi),$$ (14)

where ρ_0 is the equilibrium charge density and the second term describes the variation of the charge density with position along the chain. This phenomena is called a "charge density wave." If the periodicity of the charge density wave is an integer multiple of the periodicity of the lattice, the charge density wave is said to be "commensurate," while it is classified as incommensurate if it cannot match a regular lattice interval.

For the quarter-filled band, small U case, a $2k_F$ lattice distortion at a reciprocal lattice vector of $\frac{\pi}{4a}$ results in a quadrupling of the spatial periodicity and a reduction

of the Brillouin zone size by a factor of four. The energy gap introduced due to the distortion at k_F has a form similar to that in Eqn. (13). As in the half-filled case, the distorted state is characterized by a charge density wave ground state. Introducing electron-electron correlation effects splits the tight-binding band into singly and doubly occupied states which are separated by the Hubbard gap of order U. Thus, at quarter-filling, k_F must be twice as large and it can be shown that the Peierls distortion is $4k_F$ in nature. The large U limit is an especially important limit for many quarter-filled semiconducting organic charge transfer salts, including those discussed in this dissertation.

The Peierls transition was a phenomena that was originally predicted to occur in purely one-dimensional systems at zero temperature. The presence of this type of metal-insulator transition in quasi-one-dimensional organic charge transfer salts and other materials at finite temperature is primarily a consequence of the weak three-dimensional interactions.

In a manner similar to the electronic Peierls distortion, described above, magnetic effects can cause a spin Peierls transition, where the opening of a spin density wave gap is accompanied by the formation of a spin density wave ground state. Several factors have been shown to influence the behavior of spin Peierls systems; among the most important are large Coulomb (U) interactions which essentially prohibit double occupation of sites and, in the presence of finite spin-phonon coupling, favor the spin density wave ground state. A good discussion of the spin Peierls transition and the resulting implications for the transport properties has been presented elsewhere.[44,36]

Models of the Electron-Phonon Interaction

In the past decade, there has been an extraordinary amount of interest in the phenomenon of electron-phonon coupling, as it has been observed in a wide variety of quasi-one-dimensional organic charge transfer salts. Several models have been

developed to aid in the understanding of the interesting manifestations of this coupling process. Isolated cluster models have enjoyed particular success due to their applicability combined with their relative simplicity. As isolated cluster models have been used extensively in this work to understand the infrared frequency dependent conductivity, they will be discussed here. Several good reviews of this subject are available.[20,19]

The solution of the electron-phonon interaction for an isolated TCNQ dimer with one electron per two TCNQ molecules has been presented by Rice et al.[22] This model is intended to mimic the behavior of a quarter-filled, infinite chain of poorly interacting, distorted dimers. The Hamiltonian in the isolated dimer model is

$$H = H_e + H_v + \sum_{i,n} g_n n_i Q_{n,i} - \vec{E} \cdot \vec{p}, \tag{15}$$

where H_e and H_v are the electronic and vibrational Hamiltonians, which describe the electronic and vibrational properties of the system in the absence of the vibronic coupling. These terms are given by

$$H_e = \sum_\sigma t(c_{2,\sigma}^\dagger c_{1,\sigma} + c_{1,\sigma}^\dagger c_{2,\sigma}) + (E_0 + \Delta_c)n_1 + (E_0 - \Delta_c)n_2 \tag{16}$$

and

$$H_v = \sum_{i,n} \frac{\omega_n}{4}(P_{n,i}^2 + Q_{n,i}^2), \tag{17}$$

respectively. Here, $(E_0 + \Delta_c)$ denotes the energy of the π orbital of monomer 1 before interaction, and $(E_0 - \Delta_c)$ is the energy of the π orbital in monomer 2, also before interaction. E_0 is the energy of the π orbital in the absence of charge asymmetry, while Δ_c refers to the site inequivalence, reflecting the fact that the unpaired electron is not shared evenly between the two sites. The linear electron-molecular vibrational

(EMV) coupling is described by the third term in Eqn. (15). Here, the g_n are the linear EMV coupling constants and the $Q_{n,i}$ are dimensionless normal mode coordinates of the A_g modes, and the $P_{n,i}$ are complex conjugates. Each normal mode is also characterized by a frequency, ω_n. The final term in Eqn. (15) describes the interaction of the unpaired electron with an externally applied field; $\vec{p}$ denotes the electric dipole moment of the n-mer, and is given by

$$\vec{p} = \frac{1}{2}(e\vec{a}(n_1 - n_2)).\tag{18}$$

In practice, $\vec{a}$ is the inter-dimer spacing. In the aforementioned equations. $c_{i,\sigma}^\dagger$ and $c_{i,\sigma}$ are the usual creation and annihilation operators for unpaired Fermions on site i, and $n_i = c_i^\dagger c_i$ is the occupation number operator. Indices are defined as follows: i denotes the monomer or site number, n indexes the vibrational modes, and σ refers to the electron spin. Note that only one electronic charge transfer excitation is allowed within this formalism, its strength determined by the transfer integral, t. Note also that the on-site Coulomb term, U, is zero in the quarter-filled case.

From Eqn. (15), the equations of motion for the dimensionless normal mode coordinates, $Q_{n,i}$,[22] are

$$\ddot{Q}_{n,i} + \omega_{n,i} = -2^{\frac{1}{2}}g_n\omega_n n_i.\tag{19}$$

Introducing dimeric normal mode coordinates, s_n and r_n, the equations of motion for the modes of interest are rewritten as

$$\ddot{s}_n + \omega_n^2 s_n = -2^{\frac{1}{2}}g_n\omega_n(n_1 + n_2),\tag{20}$$

and

$$\ddot{r}_n + \omega_n^2 r_n = -2^{\frac{1}{2}}g_n\omega_n(n_1 - n_2).\tag{21}$$

Noting that $(n_1 + n_2)$ is a constant of the motion, we conclude that the symmetric modes, s_n, are not coupled with the motion of the radical electrons.[22] These

symmetric modes are also called "amplitude modes," and can be observed in Raman spectroscopy. It is the antisymmetric or "phase phonon modes" which are of primary interest.[24] Referring to Eqn. (18), we note that any change in the dipole moment via interaction with the external field will excite the antisymmetric modes in the above fashion.[22]

The frequency dependent conductivity within the quarter-filled isolated dimer model[22] is given as

$$
\sigma(\omega) = -\left(\frac{i\omega e^2 a^2 N}{4\Omega}\right)\left(\frac{\chi(\omega)}{1 - D(\omega)\frac{\chi(\omega)}{\chi(0)}}\right),
\tag{22}
$$

where a is the dimer separation, N is the number of dimers per unit cell, and Ω is the volume of the unit cell. Here, $D(\omega)$ is the phonon propagator

$$
D(\omega) = \sum_n \frac{\lambda_n \omega_n^2}{\omega_n^2 - \omega^2 - i\omega\gamma_n},
\tag{23}
$$

where the λ_n are the dimensionless electron-phonon coupling constants, ω_n are the unperturbed frequencies, and γ_n are the phonon linewidths for each A_g mode, respectively. The reduced electronic polarizability, $\chi(\omega)$, is

$$
\chi(\omega) = \frac{\frac{8t^2}{\omega_{ct}}}{\omega_{ct}^2 - \omega^2 - i\omega\gamma_e},
\tag{24}
$$

where ω_{ct} is frequency and γ_e is the linewidth of the electronic charge transfer excitation. The dimensionless coupling constants are written as

$$
\lambda = \chi(0)\frac{g_n^2}{\omega_n} = \frac{8t^2 g_n^2}{\omega_{ct}^3 \omega_n},
\tag{25}
$$

where $\chi(0)$ is the zero frequency limit of Eqn. (24). It is the g_n which are most commonly cited (in a generic fashion) as the electron-molecular vibrational (EMV)

"coupling constants," and are the fundamental microscopic quantities of interest in this analysis. The units of $\chi(\omega)$ and $\chi(0)$ are centimeters, while $D(\omega)$ and λ_n are dimensionless; the g_n are in units of wavenumbers. Thus, the computed frequency conductivity spectrum, $\sigma(\omega)$, has units of Ω^{-1} cm^{-1}.

For the half-filled dimer, U is no longer zero.[40] Although Eqn. (22) and the expressions for the phonon propagator remain unchanged, $\chi(0)$ and $\chi(\omega)$ must be modified to account for the effect of Coulomb repulsion.[40] Thus,

$$\chi(\omega) = \frac{\frac{16t}{(\frac{U^2}{4}+4t^2)^{0.5}}}{(\omega_{ct}^2 - \omega^2 - i\omega\gamma)}. \tag{26}$$

Taking the zero frequency limit of the above expression, we find

$$\chi(0) = \frac{16t}{\omega_{ct}^2(\frac{U^2}{4} + 4t^2)^{0.5}}. \tag{27}$$

The expression for the dimensionless coupling constants,

$$\lambda_n = \chi(0)\frac{g_n^2}{\omega_n}, \tag{28}$$

is modified accordingly. These results were first presented by Rice,[40] as well, and saw rapid application to half-filled, dimerized TCNQ based systems.[45]

Interaction of the A_g phonon mode with the charge transfer excitation causes the resonance frequency of the vibration to be shifted to lower frequency from its unperturbed position in an isolated molecule. Within the isolated dimer model, we can calculate

$$\mathrm{Re}\left(\frac{1}{\sigma}\right) = A\left(B + \sum_n \frac{g_n^2\omega_n\gamma_n}{(\omega_n^2 - \omega^2)^2 + (\omega\gamma_n)^2}\right). \tag{29}$$

Here, A and B are constants, relating to the dimensions of the unit cell and the electronic parameters, respectively. Thus, by fitting a sum of Lorentzian oscillators

to this function, we can obtain the unperturbed frequencies of each A_g mode.[28] In the conductivity spectrum, these modes are generally observed to have Lorentzian line shapes; however, when they overlap with the electronic band, they have a Fano type[46] (or derivative) line shape. The isolated dimer model was also used as a basis for the first proposal as to the origin of the fine structure in the conductivity spectrum.[47]

In addition to presenting a model of the infrared conductivity, the dimeric cluster models have been used to describe charge transport in semiconducting salts via an activated hopping mechanism and to estimate the activation energy for that charge transfer.[48,49] This approach is valid for strongly localized salts.

In order to describe a wider variety of materials, the ideas of electron-phonon coupling in isolated dimeric clusters were extended by Vartsev to include trimers, tetramers and n-mers.[23,3] The Hamiltonian for the isolated tetramer model is

$$H = H_e + H_v + \sum_{n,i} g_n n_i Q_{n,i} - \vec{E} \cdot \vec{p}. \tag{30}$$

For the case of the quarter-filled tetramer,

$$H_e = t \sum_{\sigma} (c_{1,\sigma}^\dagger c_{2,\sigma} + c_{2,\sigma}^\dagger c_{1,\sigma} + c_{3,\sigma}^\dagger c_{4,\sigma} + c_{4,\sigma}^\dagger c_{3,\sigma}) + t'(c_{2,\sigma}^\dagger c_{3,\sigma} + c_{3,\sigma}^\dagger c_{2,\sigma})$$

$$+ \frac{U}{2} \sum_{i,\sigma} n_{i,\sigma} n_{i,-\sigma} + V(n_1 n_2 + n_2 n_3 + n_3 n_4) + \Delta(n_1 + n_4) + \Delta(n_2 + N_3) \tag{31}$$

and

$$H_v = \sum_{n,i} \frac{1}{4}(P_{n,i}^2 + Q_{n,i}^2)\omega_n \tag{32}$$

describe the behavior of the unpaired electrons and the symmetric intra-molecular vibrations of the uncoupled material. As before, the electron-phonon coupling is incorporated in a linear manner with the third term in Eqn. (30). In this model, the

TCNQ molecules are arranged as $ABBA$ within the tetramer. It is assumed that t, the transfer integral within the AB molecular pairs, is larger than t', the transfer integral within the BB molecular pairs; a negligible transfer integral is assumed between AA moieties. As the solution for this case of two electrons per tetramer is similar, although more complicated, to that outlined above for the quarter-filled dimer,[23] only the final results will be presented here.

The frequency dependent conductivity for the isolated tetramer model[23] is given as

$$\sigma(\omega) = -i\omega N_t e^2 \left(\frac{\chi_{11} A^2 + 2\chi_{12} AB + \chi_{22} B^2 + (\chi_{12}^2 - \chi_{11}\chi_{22})(A^2 D_b + B^2 D_a)}{1 - \chi_{11} D_a - \chi_{22} D_b + (\chi_{11}\chi_{22} - \chi_{12}^2) D_a D_b} \right). \tag{33}$$

The phonon propagator has a similar form as in the isolated dimer model,

$$D_{a,b} = \sum_n \frac{g_{n;a,b}^2 \omega_{n;a,b}}{\omega_{n;a,b}^2 - \omega^2 - i\omega\gamma_n}, \tag{34}$$

but the subscripts a and b allow for charge differences on the A and B molecules. The parameters A and B are defined $A = (2x + x')/2$ and $B = x'/2$, where x and x' are the molecular overlaps for the AB and BB molecular pairs, respectively. The reduced electronic polarizabilities are given by

$$\chi_{11}(\omega) = \sum_\beta \frac{|\langle \beta | n_1 - n_4 | 1 \rangle|^2 2\omega_{\beta 1}}{\omega_{\beta 1}^2 - \omega^2 - i\omega\gamma_\beta}, \tag{35}$$

$$\chi_{12}(\omega) = \chi_{21}(\omega) = \sum_\beta \frac{\langle 1 | n_1 - n_4 | \beta \rangle \langle \beta | n_2 - n_3 | 1 \rangle 2\omega_{\beta 1}}{\omega_{\beta 1}^2 - \omega^2 - i\omega\gamma_\beta}, \tag{36}$$

and

$$\chi_{22}(\omega) = \sum_\beta \frac{|\langle \beta | n_2 - n_3 | 1 \rangle|^2 2\omega_{\beta 1}}{\omega_{\beta 1}^2 - \omega^2 - i\omega\gamma_\beta}. \tag{37}$$

Here, $\omega_{\beta 1}$ is the energy of transition from the excited state, β, to the ground electronic state. Matrix elements in the χ_{ij} are calculated as described in Ref. 23, with

the coefficients for the ground state wavefunction chosen based upon the relative size of various parameters such as U, V, $\frac{t'}{t}$, and $\frac{\Delta}{t}$. In practice, the initial choice of the aforementioned parameters is based upon chemical considerations, and these parameters are varied by trial and error to obtain the best fit. The coefficients for the excited state wavefunctions are determined from the equations presented in the Appendix of Ref. 23. In this model, parameters are generally chosen to allow two low energy electronic excitations in the mid-infrared, which couple strongly to the A_g vibrational modes, and two excitations at much higher energies.

The success of the isolated cluster models[22,40] and the phase phonon theory[24] at explaining the physics of the electron-phonon interaction in a variety of quasi-one-dimensional charge transfer salts has been well documented. Discrepancies have generally been attributed to the extended nature of the compound under study. To this end, periodic cluster models were developed.[50,51] To obtain a more complete understanding of the electron-molecular vibration interaction in less localized systems, several additional models have been put forward. Of particular note is a two-fold degenerate charge density wave model by Bozio et al.[25] This model has been applied to several materials with notable success, allowing an investigation as to the nature of the gap as well.[9,8,52] Finally, it has also been noted that the aforementioned models have difficulty with regard to the intermediate Coulomb interaction limit.

However, just as important as a perfect model fit is the physical insight and increased understanding of the microscopic parameters that even simple cluster models bring to polarized infrared measurements on quasi-one-dimensional materials with unpaired radical electrons.

Luminescent Polymers

Photo-luminescence

When a material absorbs a photon of energy greater than the band gap, an electron is promoted to the excited state. Relaxation of the excited state may occur through a number of competing processes which may be characterized as being either "radiative" or "nonradiative." Radiative processes occur with the spontaneous emission of light, whereas nonradiative processes involve dissipation of energy through a variety of internal conversion mechanisms, including multiphonon processes (heat), intersystem crossing, Auger processes, and other complicated internal conversion mechanisms involving collisions or impurities.[53,54,55,56]

The most basic model of fluorescence considers only the radiative process. A simplified energy diagram is shown in Fig. 7 for a spin singlet material. Absorption of light excites an electron from its ground state, S_0, to a higher energy singlet surface, S_1 (or S_2). After a brief lifetime in the excited state, the electron can decay back to the ground state by emitting light (fluorescence).[57,58] Emission can occur from either an intrinsic band or an impurity level.[56] Of course, transition to an excited state and subsequent re-emission from that same state, such as a band-to-band transition, is not generally useful, as the emitted light is simply reabsorbed. This simplified picture in Fig. 7 is greatly affected by competition from nonradiative processes.

A more realistic picture of the energy levels of a molecule and the available pathways of decay from the excited state is displayed in Fig. 8. Note that there are two distinctly different pathways of radiative decay: fluorescence and phosphorescence.

The fluorescence emission process becomes more complicated due to vibrational considerations.[54] This is because, in practice, the electron is promoted to an excited vibrational level on the S_1 surface. Decay rarely occurs from here. Instead, the molecule may loose energy via nonradiative vibrational processes, cascading down-

ward toward the lowest energy vibrational state on the excited surface.[53,54,55] The final return to the ground state electronic surface may occur via radiative or nonradiative mechanisms. Thus, the frequency of emitted light is less than that of the exciting source due to losses associated with vibrational motion.[57,58]

The alternate mechanism of radiative decay, phosphorescence, is more complicated. Excitation of the electron to the S_1 surface proceeds with the absorption of light as described in the preceding paragraphs. However, before phosphorescence can be observed, the system must convert from a singlet to a triplet spin state. This radiationless process is called intersystem crossing.[53,54,55] (Note that excitation directly to T_1, the excited triplet surface, is spin-forbidden unless the original ground state is a triplet.) The electron can decay from the excited triplet state with the emission of light. Because of Hund's rule considerations, the triplet spin state is more energetically favorable than the singlet state. Consequently, phosphorescence emission is commonly observed at a lower energy than fluorescence.

The spin selection rules of these two radiative processes are reflected in the luminescent lifetimes and efficiencies. The lifetime of fluorescence is normally on the order of 10^{-11} to 10^{-7} seconds, whereas phosphorescence occurs over a time span of 10^{-3} seconds to several hours.[53,55,59]

Finally, it is interesting to note that although the intensity of emission is commonly a function of excitation energy, it almost always occurs at the same energy, with similar spectral shape. This is because decay always occurs from the lowest vibrational state on the S_1 or T_1 surface (or an impurity level) after suffering nonradiative vibrational losses—regardless of the excitation energy.[53,54]

In many cases, neither fluorescence nor phosphorescence is observed. This indicates that the nonradiative processes are occurring more rapidly than the radiative ones. One mechanism of nonradiative decay is "internal conversion," in which the

absorbed energy is completely converted to heat by using intersystem crossings, collision processes, conformational changes and vibrational losses to cascade down to the S_0 state.[53,54,55] In this manner, an excited electron may make its way down to the ground state without emitting any light at all! Thus, the relative rates of internal conversion and spontaneous emission are very important.

Fluorescence is known to be a first-order rate process[53,54] with rate constant given as k_f. This decay process may be represented as:

$$A^* \rightarrow A + h\nu. \tag{38}$$
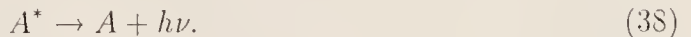
The nonradiative decay processes (internal conversion and intersystem crossing) are also described by a pseudo first order rate expression

$$A^* \rightarrow A + heat, \tag{39}$$
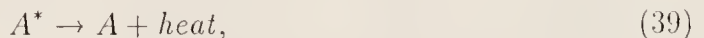
with rate constant k_{nr}. Quenching is a third possible mechanism for molecular relaxation, but it will not be included in this discussion.[53,54,55] The two aforementioned competing processes can be modeled as two first-order reactions in parallel. Hence, the overall rate expression for decay is given by:

$$-\frac{dA^*}{dt} = k_f A^* + k_{nr} A^*. \tag{40}$$

Separation and integration yields the usual first-order exponential decay:

$$A^* = A_0^* e^{-Kt}, \tag{41}$$

where K is the combined rate constant $(k_f + k_{nr})$.

At this point, it is natural to define an emission efficiency (or "quantum yield") as the number of quanta emitted by fluorescence divided by the number of quanta initially absorbed.[55] The quantum yield, Φ_0, is give by

$$\Phi_0 = \frac{k_f A^*}{k_f A^* + k_{nr} A^*}. \tag{42}$$

Thus, as the radiative emission pathway becomes more favorable, Φ_0 increases. Although the intrinsic fluorescence efficiency of many materials is very high, self-absorption, surface scattering, and partial reflection at various device interfaces significantly reduce the external device efficiency.[53,56]

It is an active area of research to identify the structural elements in materials which affect this balance between radiative emission and internal conversion.[54,55,59] Aromatic rings and other double bond combinations are known to facilitate fluorescence due to their rigidity and resonance character. Molecular rigidity diminishes the rate of internal conversion as well as intersystem crossings—thus reducing losses due to both internal vibrations and decay via phosphorescence. Electrons in conjugated bonds facilitate radiative recombination as they are easily promoted to the excited state. The electron donating or withdrawing substituents affect the resonance characteristics of a ring or double bond structure and, thereby, the emission intensity. In addition, samples in the solid state have lost additional degrees of freedom, with the result that internal conversion is less probable. Finally, impurities such as halides, metals, residual monomer or solvent molecules may act to reduce or "quench" fluorescence intensity via a second order rate process.

One of the most common uses of luminescence spectroscopy is to understand the excited state geometry and electronic properties relative to those in the ground state. The theoretical basis for such studies derives from the Franck-Condon Principle.[53,54] The Franck-Condon Principle is based upon the idea that electronic motion is much

faster than nuclear motion; thus, the electronic charge density is always assumed to be at a stationary state with respect to the nuclear skeleton. Four distinct steps characterize the total absorption and emission process. Immediately after excitation, the molecule is in the excited electronic state, although it is still in the ground state geometry. This is called the Franck-Condon excited state. Within a short time, the molecule relaxes to the lowest energy vibrational state on the S_1 surface (the "equilibrium excited state"), having acquired a more energetically favorable geometry which is compatible with the new distribution of electron density. Upon emission of a photon, the molecule decays to the Franck-Condon ground state, which, immediately after emission, is the same as that in the equilibrium excited state. Upon thermal relaxation, the molecule reaches the lowest energy equilibrium ground state, characterized by the equilibrium ground state geometry.

As the radiative decay occurs from the equilibrium excited state geometry, the emission spectra itself is characteristic of the changes in geometry, electron and vibrational structure between the ground and excited state.[53,55] These changes are evaluated in two ways. First, the magnitude of the energy difference between the absorption and emission band maxima, the Stokes shift, reflects the extent of geometry relaxation between the ground and excited states. A large (greater than 1eV) Stokes shift is indicative of large relaxation effects and geometry changes between the ground and excited state. Secondly, the "mirror image" relationship is used to compare the shape of absorption and emission spectra.[53,59] Similarly shaped curves imply a similar spacing of vibrational levels, while large differences in the emission spectra suggest significant changes in the vibrational structure in the equilibrium excited state as compared to the ground state. These differences are most often due to anharmonic effects in the upper energy bands. Consequently, measurements of ab-

sorption and photo-luminescence are commonly combined to access both structural, electronic and vibrational differences between the ground and excited states.

For semiconducting polymers with non-degenerate ground states, such as those in this study, the radiative decay process is more complicated than described above due to the role of intra-chain defects.[60,61,62,63] A simplified diagram of the likely excitation and decay process is shown in Fig. 9. The initial excitation promotes an electron from the valence to the conduction band. This is a (π,π^*) excitation which relaxes into positively and negatively charged polaron sites. Due to the quasi-one-dimensional nature of the chain and the strong electron-phonon interactions inherent in such systems, the charge is thought to relax (by a nonradiative process) into a localized polaron exciton (or neutral bipolaron exciton) state. The formation of such a charge defect is also accompanied by a lattice distortion. A diagram of a neutral bipolaron (or polaron exciton) charge defect is shown in Fig. 10 for poly-p-phenylene. This singlet polaron exciton is thought to be the luminescent center in these materials.[60,32] Note that the neutral bipolaron exciton is lower in energy than two polaron defects because of the Coulomb attraction of an electron and a hole.[64] After a short lifetime, the singlet exciton decays to the ground state with the emission of light. Nonradiative relaxation lowers the energy to the equilibrium ground state. Note that radiative decay will always occur at energies less than the band gap, thus highlighting the importance of a large gap for the attainment of visible light emission. The depth of the polaronic levels within the gap (with respect to the valence and conduction band) is also an important consideration. If these levels were positioned too close to the band edges, self-absorption would interfere with the decay process.

There are many fast nonradiative decay mechanisms which can complicate this picture. Several, such as conjugation length and interrupting defects, multiphonon processes and conformational effects, are particular to or more pronounced in macro-

molecular systems.[60] The degree of conjugation affects the confinement and mobility of the exciton, whereas vibrational and configurational considerations dictate the number of available nonradiative relaxation pathways. The complexity of the polymeric material clearly provides an increased number of internal conversion pathways due to additional vibrational and configurational degrees of freedom. Conjugated polymers can also undergo intersystem crossing to the triplet state and subsequent radiationless decay. In addition, Friend et al.[60] suggested that various collisions between polaron pairs or between polarons and bipolarons lead to the destruction of these excitons resulting in radiationless decay via multiphonon processes. Such a mechanism has been shown to be very efficient in highly conjugated polymers.

Electro-luminescence

Photo-luminescence is a necessary condition for electro-luminescence. Thus, a steady state photo-luminescence measurement is a useful screening process in which to sort out potential electro-luminescent light emitters. However, not all materials which photo-luminesce display electro-luminescence, primarily due to the different manner in which the excitation is achieved. In electro-luminescence, the electrons in the excited state originate from charge injection rather than photoexcitation. Thus, in electro-luminescence, electrical energy is converted to light.

Charge injection generally proceeds through a forward biased pn junction.[56] A simplified diagram of a pn junction (with zero applied voltage) is shown in Fig. 11. The region of interest is the "depletion region," on either side of $x = 0$. In the depletion layer, there are no free carriers—only ionized impurities or bound charges, with a distinct concentration profile through the depletion regime[39] caused by the difference in chemical potential (Fermi level) of the two materials. The spatial arrangement of the ionized impurities produce an electric field across this region resulting in a potential barrier, V_0, between the n and p sides of the contact (Fig. 11). This voltage

difference represents a barrier to the movement of positive charge toward the n-doped region and vice versa. A wider depletion layer results in a larger potential barrier.

Upon application of an external voltage, the carrier acquires the necessary kinetic and potential energy to overcome the depletion layer barrier, V_0. Hence, it is "injected" into the conduction band of the other layer. The size of the applied voltage modifies the voltage across the depletion layer, as well as significantly affecting the width.[39,65] Charge injection is facilitated if the electrons move in the direction of the barrier (positive bias), while if the carriers move against the barrier, they must overcome the potential V_0 (negative bias). This is the origin of the rectifying behavior of a pn junction.

At a sufficiently high voltage, the depletion layer becomes so wide that a new mechanism begins to supply the charge carriers.[65] Under these conditions, the current/voltage relationship develops large non-linearities so that a small increase in the applied voltage results in a large increase in the diode current. The two possible "breakdown mechanisms" generally occur between 5 to 7 V, or greater than 7 V, for the Zener and avalanche effects, respectively.[65] The Zener breakdown mechanism seems most applicable to our studies. It occurs when the electric field in the depletion layer becomes so large that covalent bonds are broken, resulting in the generation of electron-hole pairs. The large number of electrons and holes created in this way are swept (by the field) across the junction to the opposite side, where they may recombine.[65] The avalanche breakdown is a collision process, whereby the carriers themselves break bonds. The exciton pairs created in a breakdown process can recombine with the emission of light.[56]

For two equally doped semiconductors, the width of the depletion layer is the same on either side of $x = 0$. However, in cases of unequal doping, the depletion layer will extend more deeply into the more lightly doped material.[65] In the extreme

case of a metal/semiconductor contact (such as in our samples), the metal has no depletion layer. Thus, the depletion region and potential barrier exists entirely on the "polymer side" of the junction. This limiting case is called a Schottky diode.[65]

The mechanism of charge injection in polymer based diodes is less well understood than those involving conventional semiconductors due to the increased complexity of the exciton being formed. In the case of a conjugated polymer with a non-degenerate ground state, the exciton is thought to be a neutral bipolaron exciton (also called a polaron exciton). It has recently been suggested that charge injection in PPV may proceed via tunneling through the potential barrier directly into the upper polaron gap state in PPV and a modified PPV system.[32] It is not known if this is a general mechanism for light emission in conjugated polymers. The authors[32] also report that thermal activation plays no role in the emission process in these PPV based systems. It remains to be investigated for other materials via EL intensity *vs.* temperature measurements.

There is generally good correlation between the photo- and the electro-luminescence spectrum for a wide variety of materials. Stokes shift and mirror image similarity considerations have also been reported to be nearly identical in the PPV based systems.[31,32] It remains to extend these preliminary investigations to luminescent polymers of varying chemical structure to ascertain whether this is a general phenomena for these materials. The similarity between photo-and electro-luminescence spectra has suggested that the same luminescent center and pathway of decay may at work in both cases, although, as indicated above, the manner in which the exciton is obtained is quite different in the two cases.[56,60,32]
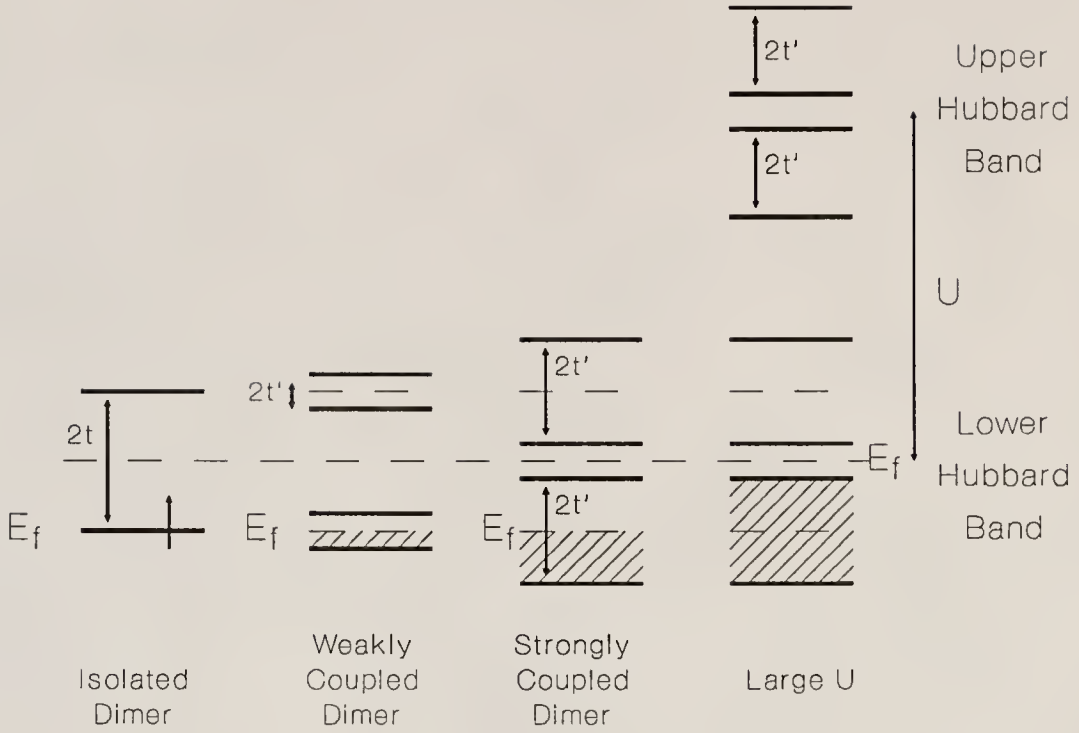
Fig. 5. Evolution of the band structure with the degree of interaction. This figures displays the progression from the zero bandwidth picture to the finite bandwidth picture, and finally to the large U picture. Note that $V = 0$ here.
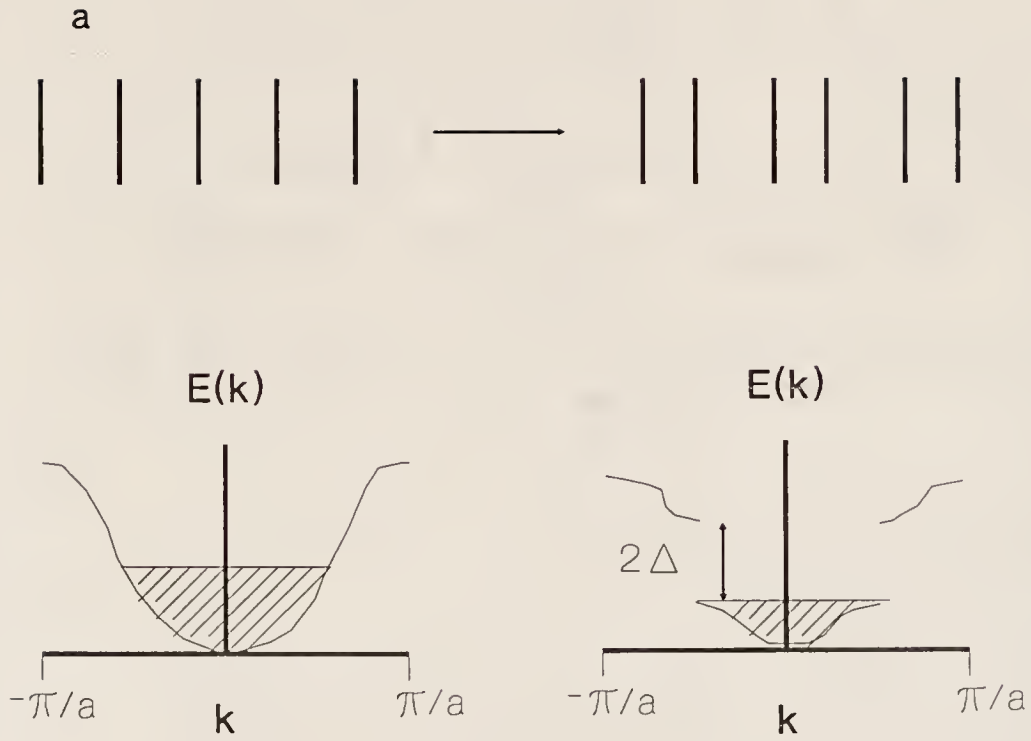
Fig. 6. Structural distortion and band structure modification due to a Peierls distortion on a half-filled uniform chain.
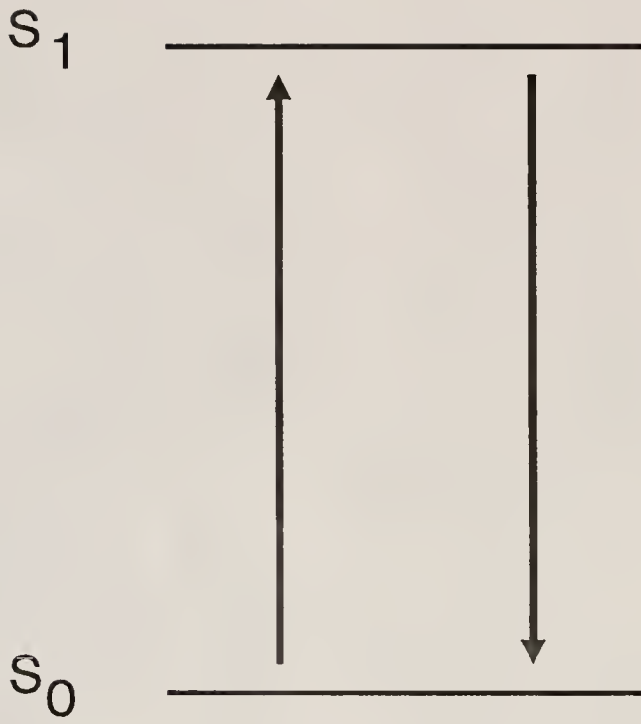
Fig. 7. Simplified picture of the band-to-band radiative decay process.
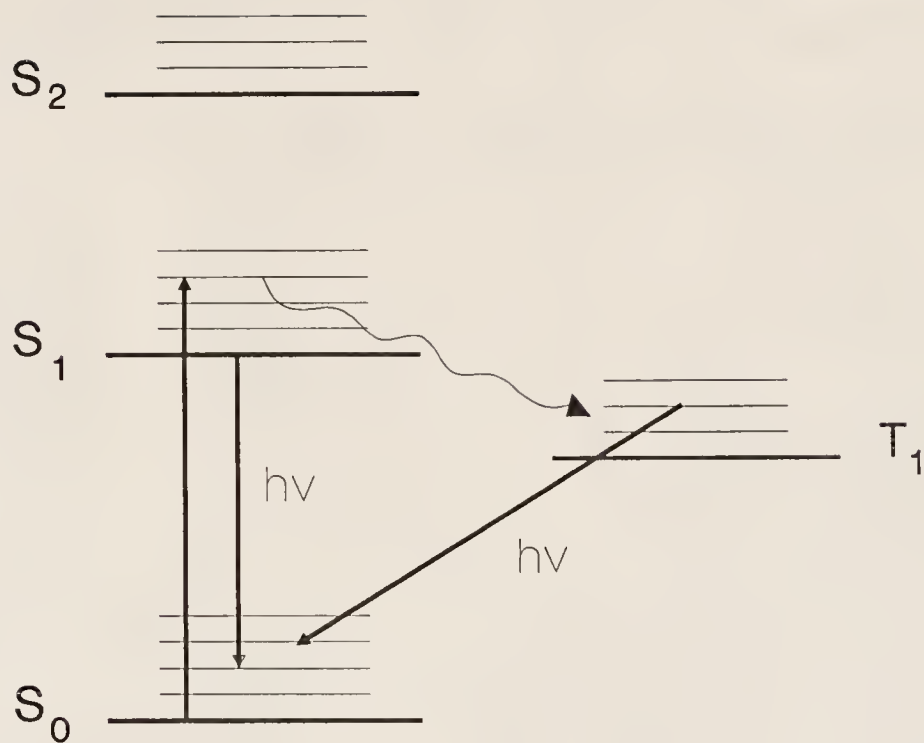
Fig. 8. Two pathways of radiative decay (fluorescence and phosphorescence) are illustrated. Nonradiative decay can also take place after excitation.
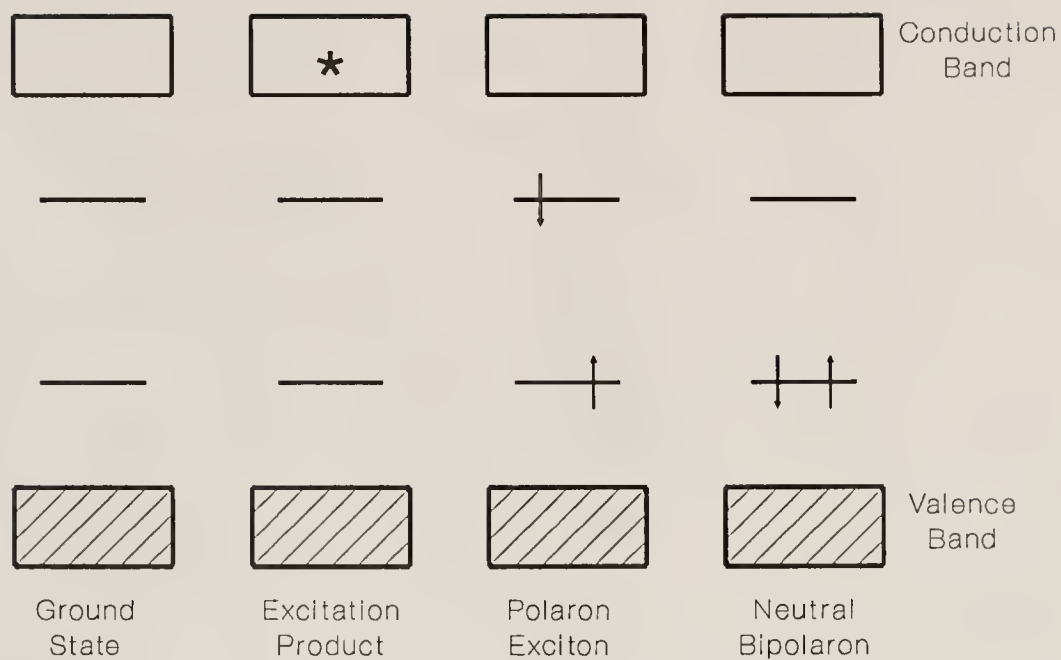
Fig. 9. Possible decay mechanism in conjugated polymers. Note that the levels within the gap arrise due to the formation of polaronic excitations.
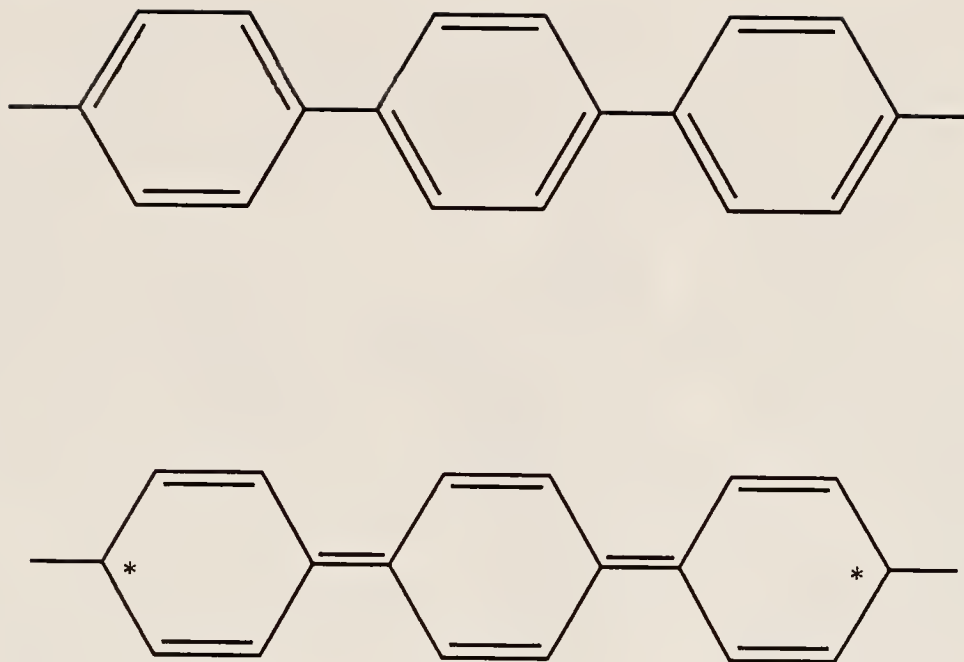
Fig. 10. Neutral bipolaron exciton in poly-p-phenylene polymer. Note that the charge defect can travel along the chain due to the extended nature of the conjugation in PPP.
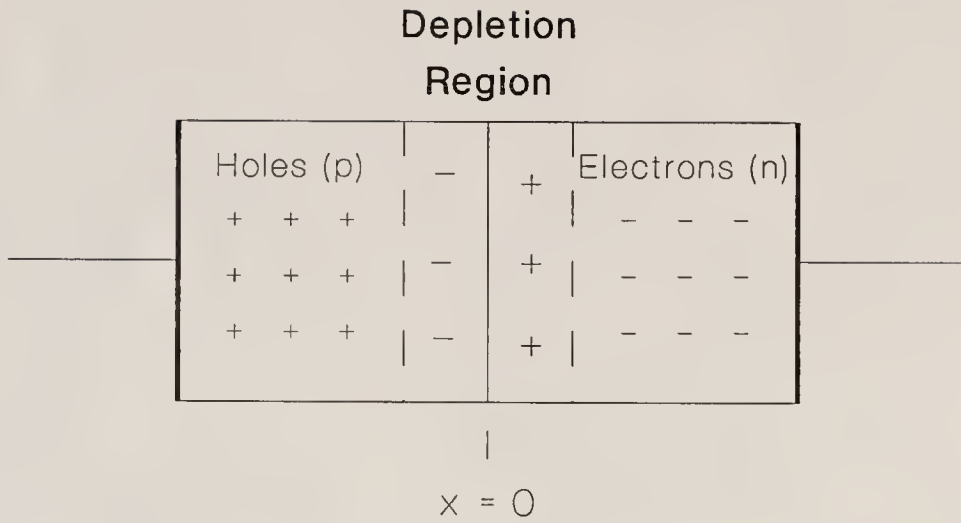
Fig. 11. Simplified diagram of a *pn* junction.

CHAPTER III
REVIEW OF PREVIOUS EXPERIMENTAL WORK

Quasi-One-Dimensional Organic Charge Transfer Salts

General

TCNQ charge transfer salts are the prototypical example of intrinsically conducting, quasi-one-dimensional organic solids. In addition to the electrical conductivity, these materials have a wide range of other interesting physical properties. These include: an unusual "stacked" crystal structure, which results in the highly anisotropic dc conductivity, magnetic and spectral properties, as well as electron-phonon coupling effects, large electron-electron correlations, and numerous structural phase transitions. Fundamental ideas from the field of one-dimensional physics (such as the Hubbard model, Peierls distortion, charge and spin density waves) have been applied to these materials with good success.

The dc conductivity of various TCNQ based charge transfer salts has been reported to span more than eight orders of magnitude. For example, metallic conductivities of up to 1000 ohm^{-1} cm^{-1} have been reported in the chain direction for samples of TTF-TCNQ at 300 K,[66] while semiconducting charge transfer salts have conductivities less than 10^{-5} ohm^{-1} cm^{-1}. The anisotropy in the dc conductivity of single crystal samples has been reported to be as high as 1000:1 for TTF-TCNQ,[66] and is commonly on the order of 200:1.

Resistivity measurements as a function of temperature show that in most of these materials, the dc conductivity increases as temperature decreases. Compounds with

metallic behavior at low temperature (such as TTF-TCNQ) have historically commanded special interest.[66] Unfortunately, most conducting TCNQ salts undergo a metal-insulator transition at low-temperature,[35] inhibiting the formation of the low temperature metallic or superconducting state. Various magnetic phenomena also compete with a low-temperature superconducting state in one dimension.[67]

For these reasons, scientists were motivated to search for other materials with either a lower Peierls transition temperature or no structural distortion at all. Increased dimensionality played an important role in reducing T_c.[68] These efforts led to the discovery of the BEDT-TTF (ET) based charge transfer materials, as well as the family of Bechgaard salts, based upon TMTSF.[30-70] The first ambient pressure organic superconductor was discovered in the family of Bechgaard salts. Superconducting phases of the ET salts have also been reported.

As synthetic metal materials have been the subject of intense study during the past three decades, the number and diversity of experimental investigations to date in this diverse field is extremely large. Therefore, I will attempt to present and summarize only the major findings, concentrating on the TCNQ based compounds, particularly those of interest in this work.

Structural Considerations

The strong anisotropy in these materials, from which the interesting physical properties derive, is known to result directly from the distinctive quasi-one-dimensional structural architecture. In these crystals, the TCNQ molecule acts as a monomer repeat unit, stacking regularly in quasi-one-dimensional columns or chains. The columns are commonly segregated on the basis of donor or acceptor species. The high electron affinity of the TCNQ molecule makes the formation of charge transfer salts energetically favorable. The degree of static charge transfer is dependent both upon the nature of the cation and the ratio of the counterion to the number

of TCNQ molecules in the crystal. For example, in the 1:1 K-TCNQ salt, there is virtually complete static charge transfer, resulting in one electron on every TCNQ site, and a half-filled band. Incomplete static charge transfer is observed in the case of TTF-TCNQ. The degree of static charge transfer is commonly accessed by structural analysis or vibrational analysis.[71,72]

Within the stacks of TCNQ molecules, the distribution of molecules can be uniform or arranged in clustered units of "n-mers."[3] The nature of this stacking arrangement has a large influence on the transport properties. For example, a uniform distribution of TCNQ molecules usually results in metallic properties. while a material with a distorted stack has semiconducting properties, due to the opening of the Peierls gap, 2Δ at the Fermi level (Fig. 6).[36] A dimeric distortion is the most common; K-TCNQ, $MEM(TCNQ)_2$ are well-known members of this class. Within the dimeric unit, the overlap geometry is commonly a ring-bond or slightly shifted ring-ring type overlap, while the external overlap is usually a strongly shifted ring-ring overlap.

For distorted systems, the electron configuration within the n-mer plays an important role in the ease of electrical transport. Compared to 1:1 salts with a half-filled band, salts with a fractional band filling have greatly facilitated transport. This is because electrons are less likely to hop to doubly occupied sites in these systems. resulting in reduced Coulomb interactions. In addition, as lattice distortions change the TCNQ stacking arrangement from one spacing to another, the electron configuration determines whether the charge density wave will be commensurate or incommensurate with the underlying lattice.

The distance between the TCNQ molecules in the stack and the mode of overlap between the TCNQ molecules in the stack determines the overlap of the electronic wavefunction, and thus, the transfer integral, t. The transfer integral is commonly

on the order of 0.1–0.3 eV for TCNQ based materials.[4,35] Ultimately, it is the value of $4t$ (the bandwidth) relative to U (the on-site Coulomb repulsion) which is the important quantity in these salts, as the ratio plays an important role in determining the periodicity of the Fermi wavevector. The electronic interactions perpendicular to the stacking direction are less favorable than along the chain direction.

A phase transition is almost always accompanied by a change in the lattice periodicity, and the nature of these structural changes can be ascertained by X-ray and neutron scattering measurements. As such changes alter the size of the Brillouin zone, they strongly affect the distribution of charge density in the material. Hence, the nature of a structural distortion is also reflected in physical methods which probe quantities related to the electronic structure, such as transport, magnetic and spectroscopic properties.

Transport Properties

Structural phase transitions almost always result in a change in the dc conductivity as a function of temperature. In fact, it is usually through such transport measurements that a phase transition is identified. For example, one interesting phenomena that is easily observed in the dc conductivity is the "metal-insulator" transition. As the name implies, the dc conductivity drops significantly due to opening of an energy gap at the Fermi surface. The size of the gap is commonly temperature dependent. Thus, the low temperature metallic state remains unrealized for most compounds. The Peierls transition is a type of metal-insulator transition. A spin density wave transition can also affect the transport properties, opening a gap at the Fermi level. Here, the energy gap represents the difference between the single and triplet spin states. A third, and less well-studied, type of structural phase transition is one driven by order-disorder considerations; it also results in a small dc conductivity.

The onset of a structural phase transition is often evident in the magnetic properties of these quasi-one-dimensional materials, and information regarding the nature and driving forces of the structural distortion can be gleaned from these measurements as well.[73,74] For example, in 1:2 compounds with large U, the magnetic susceptibility is unaffected at a $4k_F$ distortion, whereas a $2k_F$ system is characterized by a sudden drop in χ_m at T_c.[20] Thus, magnetic susceptibility measurements can distinguish between a magnetically driven structural phase transition, such as a spin Peierls distortion, and a phase transition which is dominated by other considerations.

Spectroscopic Studies

The unique structural architecture and various charge distributions of the various TCNQ charge transfer salts are strongly manifested in the spectroscopic properties. As the major thrust of this dissertation, this subject will command special attention in this review.

The polarized infrared and optical properties of numerous TCNQ charge transfer salts have been reported at room temperature. In the many good review articles in print,[4,18,20,19,30] the authors note the extreme anisotropy between various crystal directions and clearly demonstrate the spectroscopic uniqueness of the TCNQ stacking direction. The measurements by Brau et al. on single crystal samples of $TEA(TCNQ)_2$ make this point particularly well.[75] $(NMe_3H)(I)(TCNQ)$ is another good example, as the authors are able to obtain data in three orthogonal polarizations. In the chain direction, the spectrum displays metallic characteristics, while in the other two polarizations, the spectra are characteristic of a semiconductor with a few obvious non-A_g vibrational features on a relatively flat background.[76] Identification of the electronic charge transfer features and their corresponding polarizations underscored the importance of localized effects and lead to a basic understanding of how charge is transported in these materials.[77,78,75,79] Intra-molecular excitations

(and the polarization dependence of such features in the solid state) were also identified.

In the semiconducting materials, ten vibrational features were observed to dominate the infrared spectrum.[75,45,78,77,80] (In metallic compounds, these features are screened.) Observation of unusually strong A_g vibrational modes polarized in the chain direction was the impetus for the development of various models of electron-phonon coupling.[24,81,22,23] Three of these models were detailed in the previous Chapter. These models, based upon the interaction between the A_g molecular vibrations and either a charge transfer excitation or an oscillating charge density wave were successful in explaining the basic physics of these coupling processes in many materials. Electron-molecular-vibrational coupling constants were determined for a wide variety of materials, and it was concluded that the degree of coupling was similar in many different TCNQ salts. To this end, Painelli et al.[82] developed a set of "universal coupling constants" for a wide variety of materials, with small differences based only upon the degree of static charge transfer to the TCNQ from the counterion. Lipari et al.[83] calculated the unperturbed phonon frequencies for the $TCNQ^-$ anion. These were a useful comparison for the frequencies obtained in the aforementioned experiments. Finally, Lipari et al. also presented a modified valence force field model calculation of the vibrational normal modes of A_g symmetry.

Later studies characterize the individual nature of the various phases in these materials, which are separated by phase transition of various kinds. Changes in the electron-phonon coupling between the high and low temperature phases of these salts commanded special attention, as this interaction is fundamentally related to changes in the lattice distortion and electronic configuration.[22,27,84] For example, in the well-studied $MEM(TCNQ)_2$ system,[22,27] the authors show that the electron-phonon coupling constants are fundamental material properties, and not a function of

temperature. However, Graja et al. arrive at a different conclusion, and they report strongly temperature dependent coupling constants for TMB-TCNQ.[85] The authors also suggest that the intensity of the A_g phonon modes should be related to a product of three functions, which describe changes in the electronic interaction, ground state occupation, and geometry with temperature, respectively.[85] Hence, the temperature dependence of the coupling constants is still a matter of investigation. These studies demonstrated the particular utility of infrared techniques, and provided the basis for the more recent spectroscopic work as a mechanistic probe to follow structural phase transitions.

Many of the most interesting spectroscopic studies of quasi-one dimensional organic materials have concentrated upon structural phase transitions and the associated metal to insulator transitions.[5-12] Detailed examination of the systematic spectral changes in the neighborhood of T_c has proved to be a useful tool in understanding changes in electron-phonon coupling through the phase transition and the changes in the gap below T_c. Swietlik and Graja[84] report the temperature dependence of the infrared spectra for the MTPP(TCNQ)$_2$ semiconducting charge transfer salt. Below T_c, the spectra display doublets of A_g origin and a strong charge transfer excitation centered at $\approx$ 2750 cm^{-1}. The reflectance changes discontinuously at T_c. Because of the first order nature of the phase transition, the temperature dependence of the reflectance displays a hysterisis. Above T_c, the vibrational features are significantly broadened and reduced in intensity; the doublet character is still present, but greatly reduced. The charge transfer excitation is also significantly weaker. Tanner et al.[5] presented a particularly interesting study on TTF-TCNQ in which they measured the far infrared spectra above and below the Peierls transition temperature. Above T_c, the spectra display metallic behavior, with the ac conductivity extrapolating to a

finite value of the dc conductivity. Below T_c, a semiconducting gap develops and the spectra displays a sharp pinning mode of the charge density wave at low energy.

Our Materials

NPrQn(TCNQ)$_2$ and DMTM(TCNQ)$_2$ are two "quarter-filled" materials which have particularly interesting structural phase transitions. The NPrQn salt undergoes a second-order metal-insulator transition at T_c,[13,14] while the dc conductivity of DMTM salt actually increases sharply below T_c.[15,16] In NPrQn(TCNQ)$_2$, the high-temperature phase is weakly metallic, which is unusual for a 1:2 quarter-filled salt; the dc conductivity drops sharply at T_c. For DMTM(TCNQ)$_2$, it is thought that the unusual transport properties below T_c are due to a crystal field distortion, which results in the narrowing of the semiconducting band gap.[86] The role of disorder is certainly important in both of these materials, although it is not well understood. Finally, K- and Rb-TCNQ are two half-filled charge transfer salts in which the TCNQ stacks go from a uniform to a dimerized molecular spacing at T_c. These sharply first order structural phase transitions have been characterized as "spin Peierls" in nature. This study will highlight the important role of the cation on the nature of the phase transition.

The following three sub-sections present a brief background specific to each of the aforementioned materials. These transport, magnetic and structural studies were the basis and impetus for our work.

NPrQn(TCNQ)$_2$

N-propylquinolinium bis-7,7',8,8' ditetracyanoquinodimethane, NPrQn(TCNQ)$_2$, is a 1:2 organic charge transfer salt containing segregated chains of TCNQ tetramers and NPrQn counterions. The stoichiometric ratio of the donor to acceptor entities is such that NPrQn(TCNQ)$_2$ is referred to as a "quarter-filled" charge transfer salt.

It undergoes a second-order structural metal-semiconductor transition at a critical temperature (T_c) of 220 K.[13,14]

NPrQn(TCNQ)$_2$ is different from most other quarter-filled 1:2 charge transfer salts, which are generally semiconductors as a result of a structural distortion that distorts the uniform intermolecular spacing and introduces gaps in the metallic band structure.[19−18] The temperature dependence of the dc conductivity is shown in Fig. 12.[13] The transport properties of NPrQn(TCNQ)$_2$ in the high-temperature phase have been described as weakly metallic, with a value[13] for the dc conductivity of approximately 1 ohm^{-1}cm^{-1}. Below T_c, the dc conductivity drops sharply by about four orders of magnitude.[13] In the low-temperature phase, conduction in NPrQn(TCNQ)$_2$ has been shown to proceed by excitation over a temperature dependent gap,[14] as in an ordinary semiconductor. An explanation for this unusual metallic conductivity above T_c was proposed by Jánossy et al.,[14] who suggested that the Coulomb interaction of the donor cations with the TCNQ chains could perturb the band structure in the TCNQ stack, resulting in a closed gap and enhanced conductivity.

Structural studies[87,88] of this material reveal that the intra-tetramer distances change significantly between the high temperature and low-temperature phases. At 300 K, intra-tetramer distances of 3.24 Å and 3.28 Å are reported, while at 100 K, these distances decrease to a uniform 3.15 Å. Thus, at low temperature, the TCNQ chains become more uniformly tetramerized. In contrast, the inter-tetramer distances are temperature independent, remaining constant at 3.43 Å, resulting in relatively well isolated tetramers within the TCNQ stack. The P$\bar{1}$ space group, the mode of overlap within the tetramer, and the intramolecular bond lengths and angles remain unaffected by the phase transition. Based upon the structural data, it has been concluded that the crystal structure becomes more uniform at low-temperature.[88] How-

ever, this conclusion is in direct contradiction with low-temperature measurements of other physical properties,[13,14] which indicate a *less* uniform charge distribution within the tetramer below T_c.

The phase transition causes important changes in the magnetic state of N-PrQn(TCNQ)$_2$.[13,14] Paramagnetic susceptibility (χ) measurements show that χ is large and constant in the high-temperature phase, corresponding to 0.8% free spins per formula unit. Between 200 and 80 K, there is a strong decrease in the susceptibility, which is characteristic of a singlet ground state with a low lying triplet spin excitation. EPR measurements also confirm the formation of triplet states below 100 K. The energy gap between the singlet and triplet states increases with decreasing temperature. At low-temperature, χ is small; below 80 K a Curie tail appears. On the basis of these observations, it has been suggested that magnetic interactions may be the driving force for the structural phase transition.[13,14,73,74]

The dielectric constant, measured at 9.1 GHz, is constant at approximately 6 in the high-temperature phase. Between 240 K and 180 K, it gradually decreases to a final value of 2 in the low-temperature phase.[13]

DMTM(TCNQ)$_2$

N-N'-dimethyl-thiomorpholinium bis-7,7',8,8'-tetracyanoquinodimethane, DMTM(TCNQ)$_2$, is also a "quarter-filled" semiconducting organic charge transfer salt containing segregated chains of TCNQ dimers and DMTM counterions. This material undergoes a first order structural phase transition at a critical temperature (T_c) of 272 K, with the unusual feature that the dc conductivity is three orders of magnitude *higher* below the transition temperature.[15] More specifically, $\sigma_{dc} = 10^{-2}$ $\Omega^{-1}cm^{-1}$ and $E_A=0.26$ eV just above the phase transition; $\sigma_{dc} = 3$ $\Omega^{-1}cm^{-1}$ and $E_A = 0.03$ eV just below it.[15,16] This unusual behavior (shown in Fig. 13) has been

described as an "inverted Peierls transition," and has tentatively been explained in terms of a crystal field distortion.[86]

Structural studies[86,89,90] reveal that the high-temperature phase is monoclinic, with the TCNQ molecules stacked in a dimerized fashion along the c direction. The intra- and inter-dimer distances are 3.25 Å and 3.29 Å, respectively. The DMTM cations, which are located on mirror planes, are disordered. The mirror planes result in the crystallographic equivalence of the two TCNQ sheets (as defined by the a/c plane) within the unit cell.

In the low-temperature phase, the crystal symmetry is reduced to a triclinic space group. At T_c, the b axis rotates slightly (about 10° away from the normal) into the a/c plane. It is likely that ordering of the DMTM counterions results in the loss of the mirror plane symmetry. The reduced crystal symmetry results in the crystallographic inequivalence of the two TCNQ sheets within the unit cell. The structure of the two TCNQ sheets in the unit cell (defined by the a/c plane) is unaffected by the phase transition.

The unusual transport properties of $DMTM(TCNQ)_2$ have tentatively been explained in terms of a crystal field distortion.[86] The band structure which is thought to result from this distortion is diagrammed in Fig. 14. The proposed band structure of quarter-filled $DMTM(TCNQ)_2$ in the high-temperature phase (monoclinic) is shown on the left. A crystal field distortion along the b axis at the phase transition temperature reduces the crystal symmetry (to triclinic), causing a splitting of the bands, as shown on the right. Four other bands occupy a similar configuration at higher energy, separated from those shown in Fig. 14 by the Hubbard gap.

In terms of transport, the net effect of the distortion is to reduce the energy gap between the valence and conduction bands. Based upon this argument, one would predict a large decrease in the activation energy for transport in the low-temperature

phase, thus facilitating thermal excitation of the carriers. Indeed, the activation energy for conduction (E_A) has been measured to be 0.26 eV and 0.03 eV in the high and low-temperature phases, respectively.[15,16] In the high-temperature phase, the small value of the dc conductivity and the large value of the activation energy suggests that the dc conductivity is due to hopping.[48,49] Despite the "inverted Peierls" nature of the low-temperature phase, the dc conductivity is relatively low, suggesting both a modest number of carriers and a limited mobility.

Thermopower measurements[16] on DMTM(TCNQ)$_2$ also show clear evidence of a first order structural phase transition, in agreement with previous results. In the low-temperature phase, these data are consistent with that expected for a transition to a small band gap semiconductor with a gap of 0.06 eV. Thus, thermopower provides further evidence for a reduction of the band gap at T_c, in support of the crystal field distortion theory by Visser et al.[86]

Magnetic susceptibility (χ) measurements[15] display the "inverted Peierls" behavior as well. In the high temperature phase, χ rises slightly from its room temperature value of $\approx 1.0 \times 10^{-3}$ emu/mol as temperature is lowered from 300 K. At T_c, χ drops sharply from a value of $\approx 1.2 \times 10^{-3}$ to $\approx 1.0 \times 10^{-3}$ emu/mol and then rises with a further decrease in temperature to a value of 2.2×10^{-3} emu/mol; below 50 K, χ drops sharply, reminiscent of a spin-Peierls transition. From an extrapolation of these results to zero temperature, it has been suggested that the value of χ may be consistent with two different TCNQ chains in the low-temperature phase, possibly one with and one without a $2k_F$ distortion.

High-resolution ^{13}C NMR studies[91,92] on DMTM(TCNQ)$_2$ show unusually large chemical shifts of lines assigned to CN groups. Below T_c, these lines split due to the inequivalence of the two TCNQ molecules in the unit cell. Because of the unusually large chemical shift of these lines, it is suggested that they are Knight shifts, and thus,

related to the unpaired electron density on the dimer. The Knight shift increases with decreasing temperature, in accord with the magnetic susceptibility measurements.

EPR studies on single crystal samples[93] also confirm the inequivalence of the TCNQ chains below the phase transition temperature as proposed by the crystal field distortion model.

K- and Rb-TCNQ

Potassium and rubidium bis-7,7',8,8'-tetracyanoquinodimethane, K-TCNQ and Rb-TCNQ, are "half-filled" organic charge transfer salts containing segregated chains of TCNQ dimers and alkali metal counterions. Both compounds undergo first-order structural phase transitions at a critical temperature (T_c) of 395 and 381 K, respectively. Due to the large on-site Coulomb repulsion (U), these 1:1 materials are commonly referred to as Mott insulators.[94,41]

In the low-temperature phase (25 °C), K-TCNQ has monoclinic symmetry, with a space group of $P2_1/n$ and eight TCNQ molecules per unit cell.[95] The TCNQ molecules are stacked in a dimerized fashion in two mutually orthogonal, inequivalent columns along the a direction. Average intra- and inter-dimer distances are 3.237 Å and 3.567 Å, respectively. Above T_c (140 °C), K-TCNQ is also monoclinic, but with a space group of $P2_1/c$ and only two TCNQ molecules per unit cell.[95] The TCNQ molecules are stacked along the a axis with a uniform interplanar spacing of 3.479 Å. The two stacks per unit cell remain mutually orthogonal, as before, but are now equivalent.

In the low-temperature phase (-160 °C), Rb-TCNQ (I) has monoclinic symmetry, and a space group of $P2_1/c$.[96] There are four molecules per unit cell. The TCNQ molecules are also stacked in a dimerized fashion along the a direction. Intra- and inter-dimer distances are 3.159 Å and 3.484 Å, respectively. The dimeric units in the Rb- compound are more isolated than those in the K- material because of the

unusually short intra-dimer distance as well as the greatly reduced inter-dimer overlap along a. In addition, the TCNQ molecule itself is not planar, but "boat-shaped." The crystal structure of Rb-TCNQ has not been reported in the high temperature phase. Given the similarity of the rubidium system in the low-temperature phase to other that of alkali-metal TCNQ salts, it is not an unreasonable expectation that the lattice dimerization may also be either sharply reduced or absent entirely above T_c.[95-98]

Despite the similar nature of the crystal structure in these two materials in the low- (and perhaps, the high-) temperature phases, the structural changes near to T_c differ substantially. Figure 15 illustrates the temperature dependence of the superlattice x-ray reflection intensity, as reported by Terauchi.[17] The superlattice reflection intensity is directly related to the square of the lattice dimerization.[17] For K-TCNQ, the data show a gradual decrease in the lattice dimerization upon approach to T_c, a discontinuity and weak decrease at T_c, and evidence of a slight residual lattice dimerization in the high-temperature phase. The behavior of the rubidium system presents a strong contrast. In Rb-TCNQ, the data display little temperature dependence in the low-temperature phase, a sharp discontinuity and very abrupt decrease at T_c, and no evidence of residual lattice dimerization above T_c. These data offer a striking illustration of the changes wrought by cation substitution on the solid state geometry, principally the difference in ionic radius, and the resulting behavior of the lattice at the structural phase transition temperature.

The transport properties of half-filled 1:1 quasi-one-dimensional materials have been well studied.[99,100] K-TCNQ and Rb-TCNQ are both semiconductors above and below T_c, with conductivities on the order of 10^{-4}–10^{-5} in the stacking direction. At T_c, the dc conductivity increases in a discontinuous manner to ≈ 1.4 times its value in the low-temperature phase. A pressure induced phase transition has been reported in a variety of alkali-metal-TCNQ salts as well.[100]

Magnetic susceptibility (χ) measurements on both K- and Rb-TCNQ display similar behavior.[99,101] The high-temperature phase is paramagnetic, with χ having values $\approx 0.77 \times 10^{-4}$ emu and 1.82×10^{-4} emu, for the K- and Rb- compounds, respectively. At T_c, χ exhibits a discontinuity, indicative of a first order phase transition. Below T_c, χ drops sharply (by two orders of magnitude), reminiscent of a spin Peierls transition. The low-temperature phase is diamagnetic in both materials. Residual free spins have been attributed to the existence of spin-solitons.[102]

Vetger et al.[99] also report the heat of transition, as measured by DSC, for several alkali-metal TCNQ salts. They find $\Delta H = 60$ cal/mol for the potassium compound, and $\Delta H = 1010$ cal/mol for the rubidium material. The violent nature of the phase transition in the Rb- compound has been reported by numerous researchers, and is well understood to reduce the accuracy and reproducibility of measurements above T_c, leading, in many cases, to the destruction of the crystal.

The microwave dielectric constant of K-TCNQ is temperature independent below T_c, having a value of $\epsilon_1 \approx 6 \pm 1$.[94] We are unaware of any such data for the rubidium compound.

K-TCNQ has been the subject of numerous spectral investigations, while the Rb-salt has been much less well-studied. Electronic spectroscopies on the potassium salt have concentrated on the two oscillator nature of the charge transfer band in the chain direction, the localized excitation of (π,π^*) origin, centered at 17000 cm^{-1}, and the importance of Coulomb interactions.[78,103,104,105,106,94,6] Low-temperature measurements clearly resolve the doublet nature of the charge transfer band[105,6] splitting it into a sharp lower-energy excitation at 7500 cm^{-1} and a weak, broader excitation near 11000 cm^{-1}. These two absorptions are commonly attributed to intra-dimer and inter-dimer charge transfer excitations along the chain, respectively,[105] although various other interpretations have been suggested. It is still a matter of investigation

as to the exact nature of the 10000 cm^{-1} absorption.[6,106,78] The single particle gap, 2Δ, has been estimated to be 0.7 eV.[94] Several groups have also estimated the on-site Coulomb interaction, U, for the potassium salt as $\approx$1 eV, indicating the importance of electron correlations in these materials.[94] An estimate of t and U for the Rb-salt obtains similar values as the K- compound.[106] Recently, Okamoto et al.[6] have completed a detailed investigation of the temperature dependence of the U bands through the phase transition. They observe a systematic red-shifting and merging of the two charge transfer excitations with increasing temperature. This is in good agreement with the earlier but less detailed studies by Yakushi et al.[105] The authors[6] report that the optical spectra of the Rb- salt is analogous to that of the K- salt in the low-temperature phase. However, above T_c, the results are quite different; in the Rb- compound, the inter-dimer charge transfer excitation is completely disappeared.[6]

The vibrational spectra of K-TCNQ has also been extensively investigated.[107−78] In these studies, the authors note the unusually strong intensity and polarization dependence of the A_g vibrational modes. Various models of the interaction between the A_g vibrational modes and the charge transfer of charge density wave have been used to understand the electron-phonon coupling in the potassium salt. These range from the application of the relatively simple isolated dimer model[78] to complex charge density wave formalisms to explain this coupling.[20] Due to its relative simplicity, the 300 K spectrum of K-TCNQ has been used extensively as a model compound to test these the applicability of many methods. We are presently unaware of any temperature dependent infrared spectra on single crystal samples. In addition, no far infrared data is available for the K- compound. A room temperature middle infrared measurement of the Rb-TCNQ salt in mull form has been reported in transmission at 300 K.[111] However, we are also unaware of any complete infrared measurements on Rb-TCNQ single crystal samples.

A few studies have compared the behavior of the electron-phonon coupling induced modes in these two salts. Bozio and Pecile[110] show that, for powder samples of a variety of 1:1 charge transfer salts (including both K- and Rb-TCNQ) the intensity of the A_g modes decreases with increasing temperature in the low-temperature phase. More recently, Okamoto et al.[6] have reported the temperature and polarization dependence of the CN stretching mode on single crystals of both materials.

Raman spectroscopy has been used extensively to study the neutral TCNQ molecular crystal as well as the K- and Rb-TCNQ charge transfer salts. Because of the different selection rule, it has been used to identify the unperturbed frequencies of the A_g vibrational modes in both the K- and Rb- compounds.[112-114] The A_g phonon modes in the potassium salt have been reported to change substantially through the phase transition, increasing in intensity upon approach to T_c and reducing again above it.[114] Raman data for Rb-TCNQ is only available only for pressed salt-KBr pellets and for single crystal samples above 350 cm^{-1}in the low-temperature phase.[112,111] However, it is reasonable to expect that the symmetry assignments of the various low energy modes in Rb-TCNQ may be similar to other 1:1 alkali TCNQ salts.

Various lattice and libron modes have been identified in the low frequency Raman studies as well.[21,113,114] For the TCNQ molecular crystal, Girlando et al.[21] report lattice modes at 41, 76, 97, 105, 133, and 144 cm^{-1}. The lattice mode frequencies in the dueterated crystal are almost identical. For the K- salt, Truong et al[113] report lattice mode frequencies of 70, 81, 110, 170, 229, and 295 cm^{-1}, with the lowest three assigned as librations. The scattering intensity of several of the lattice modes in the K- salt has been shown to decrease with increasing temperature and broaden significantly above T_c.[113,114] The frequencies and symmetry designations of these modes will be discussed in detail in Chapter 6.

Work has also focussed upon the nature of the various structural phase transitions in Mott insulators. The alkali-metal TCNQ charge transfer salts are generally considered to be spin Peierls systems,[115,116,117] with a $2k_F$ structural distortion at T_c. Experimental evidence for this conclusion derives primarily from the temperature dependence of the magnetic susceptibility, where the sharp decrease of χ at T_c is evidence for the opening of a spin-wave gap.[99,101] The diamagnetic phase is accompanied by the formation of spin-soliton defects.[102]

Luminescent Materials

Heterogeneous (III-V and II-VI) inorganic semiconductors have historically received the majority of attention in the field of luminescent materials technology. Some of the materials currently under intense study for possible use in opto-electronic applications include GaAs, ZnS, and ZnSe.[118-124] However, the widespread use of these materials has been hampered by fabrication problems and low EL efficiency. Researchers have implanted dopants in these semiconductors in an effort to circumvent these shortcomings.[121-120] Porous silicon is another inorganic material which has also generated a great deal of excitement recently. It exhibits visible red-orange photoluminescence, and research is currently in progress to demonstrate reliable electroluminescence and develop high efficiency devices from this technology.[125]

Organic materials have also been successfully fabricated into light emitting diodes. For example, anthracene molecule is a blue emitter, although the efficiency is not very high.[126] Additionally, devices fabricated from low molecular weight organic materials have had stability problems.[127] A more promising organic material for use in opto-electronic applications is buckmisterfullerine (C_{60}). Recently, a broad near-infrared and visible EL peak was reported in an undoped C_{60} diode device.[128] Copper phthalocyanine based diode devices are also under study.[129]

Photo-luminescence of conjugated polymeric materials has been a well known phenomena for several years. There are numerous studies in the literature evaluating the optical absorption and steady state photo-emission properties, the Stokes shift, the photoinduced absorption effect, as well as time resolved measurements.[60,130,62,131,132,133] The studies on poly-phenylenevinylene (PPV) and related materials by the Cambridge group have been the most extensive.[60,134,135] The nature of the various excitons and the mechanism of radiative decay (as well as the nature of the competing non-radiative processes) dominate much of their work. Their analysis of the photo-excitation and recombination process is as follows. After photo-generation of polaron lattice defects, the quasi-one-dimensional nature of the lattice acts to local the charges in polaron-exciton or (neutral bipolaron exciton) defects. Photo-induced absorption experiments have provided the most important substantiating evidence for this proposal.[60,134,131,136] Further evidence for the formation of such defects also comes from the absence of ESR and photoinduced ESR signal, as these singlet excitons have no net charge.[60,130] Subsequent recombination of the po-laron exciton leads to light emission. Evidence for the neutral bipolaron exciton has been observed in other materials as well.[130,137,138]

The use of conjugated polymers as a diode material is a relatively recent development. In fact, the first reports of electro-luminescence in polymers appeared in late 1990! Undoped polymers are ideal materials for diode applications because of the large, tunable (π,π^*) band gap[139,140,141] and the quasi-one-dimensionality of the chain. Polymeric materials offer significant advantages over the aforementioned conventional semiconductors, the most important being the ease of processability. This is partially due to the fact that good luminescence properties can be obtained from oligomeric chains.

In the next section, I will present a review of the field of electro-luminescent polymers. In the following section, I will briefly discuss experimental results which are directly relevant to the materials used in this study.

The Field of Electro-luminescent Polymers

Burroughes et al.[31] were the first to demonstrate yellowish light emission (at 600 nm) from poly(p-phenylene vinylene) (PPV) diodes in late 1990. The authors reported the current-voltage characteristics, and showed that there is a 14 V threshold for substantial charge injection in this material. They also demonstrated that the integrated EL intensity was approximately linear with current. Device efficiencies on the order of 0.05% were reported.

The results of Burroughes et al. were confirmed by Braun and Heeger[32] for both PPV and a chemically modified PPV system. Here, the authors suggest a plausible mechanism for light emission in these materials, in which the electrons tunnel from the rectifying metal contact into the upper polaron state in the gap. Structural relaxation to the excited state of the polaron exciton (neutral bipolaron exciton) proceeds by a non-radiative process, after which, radiative decay occurs in the characteristic manner described previously by the Cambridge group.[60] It is not known if the tunneling mechanism is a general phenomena.

Ohmori et al.[34] have studied the effects of the length of an alkyl side chain on the electro-luminescence of poly(3-alkylthiophene) diodes. They report red-orange emission at room temperature, and increased emission intensity from the diodes with the longer alkyl side chains.

Recently, Grem et al.[33] have reported the photo- and electro-luminescence of poly-(para-phenylene) (PPP) made by a precursor method. PPP is a wide band gap semiconductor, and due to the non-degenerate of the ground state, supports the formation of polaron charge carriers.[137,138] Grem et al. report a Stokes shift of

about 1.1 eV between the absorption maximum and the photo-emission maximum in PPP. They also observe greenish-blue emission properties from the diode devices: efficiencies between 0.01 and 0.05 % are reported.

Finally, copolymers have also been successfully incorporated into diode devices.[141] This process can potentially allow device patterning, and hence, frequency tuning of the emitted light at various points on the diode. These devices display improved emission efficiencies, as well.

On the more practical side, there have been several reports on the importance of hole and electron transport layers in fabricating devices with improved EL performance.[142,143,144,34,145] The transport layers are thought to facilitate control of the recombination process, resulting in increased EL efficiencies.[142,143] In recent experiments, the chemical identity of the metal contact has been shown to significantly influence the intensity of diode light emission.[32] This is most likely due to the combination of work function and Fermi level matching considerations which act to reduce the width of the Schottky barrier.[32] For example, it is thought that the calcium electrode facilitates charge injection and reduces heating near the anode. Indeed, Braun and Heeger[32] report improved light emission properties for a calcium anodic contact rather than an indium one. In addition, researchers have recently reported the fabrication of an "all-polymer" light emitting diode.[146] Such a flexible, large area diode is expected to find many uses in the electronics industry. Finally, polymers with very high luminescent efficiencies are also finding applications as laser dye materials.[147]

Our Materials—Previous Work

The chemical structure of the polymers used in this study are diagramed in Fig. 2, Fig. 3 and Fig. 4. The structures displayed in Fig. 2 are based upon *meta*-linked phenylene, the structure in Fig. 3 is poly(2,1':4',1":4",1"'-quarterphenylene-

1,4) (PQP), while the structures shown in Fig. 4 are based upon 1,4-bis(2-thienyl)phenylene (PBTP) with symmetric side groups.

Phenylene and thiophene groups (as well as unsaturated double bonds) are well known components of other electro-luminescent polymers, such as PPV, PPP and P3AT. This is because the conjugated character of the ring can stabilize excess photo- or chemically induced charge by forming a quinoid based resonance structure.[64] Depending on the spin and charge, these defects can be polaronic or bipolaronic in nature.[64] Due to their non-degenerate ground state, the phenylene and PBTP based materials are expected to form polarons upon photo-injection. Due to the quasi-one-dimensionality of the chain and strong electron-phonon coupling effects, these polarons are thought to combine to form the polaron exciton (or neutral bipolaron). The effect of this neutral charge defect on the chemical structures of PMP and PQP is shown in Fig. 16.

It is anticipated that the phenylene components of the materials shown in Fig. 2 and Fig. 3 will function as active emitter centers. By linking the various emitter groups in a *meta* fashion (Fig. 2), each group is electronically isolated from one another, but can individually support a charge defect of the type discussed above. In the case of the the quarterphenylene (PQP) polymer (lower structure of Fig. 16), steric hindrances act to twist the main-chain out of its planar configuration. This destroys the long range conjugation which is inherent in the unsubstituted PPP system, thus isolating the charge defects on the pendant side chains. Although these materials can support the formation of a neutral bipolaron exciton, it can not travel along the chain due to the aforementioned broken conjugation.

This idea of a discrete EL emitter center is the most important fundamental idea that we investigate in this work. In a discrete emitter unit, the charge defect as well as the lattice distortion are localized on one portion of the chain. All of the phenylene

based polymers in Fig. 2 and Fig. 3 may be thought of as containing a series of discrete emitting units, without any long-range conjugation. This set of materials allows us to study the influence of emitter unit structure on the electronic properties.

Solution phase absorption and photo-luminescence data of the phenylene based materials (shown in Fig. 2) has been reported by Ruiz and Reynolds.[148] For poly-m-phenylene, they find the absorbance maximum and the semiconducting energy gap to be 260 and 350 nm, respectively. These absorbance features are a relatively weak function of the emitter unit conjugation length of the material. For example, upon increasing the number of conjugated units from two to five, a 20 nm red shift of the absorbance maxima was observed. The photo-emission data display a strong, narrow emission spectra in the blue frequency regime. With increasing conjugation length of the discrete emitter center, the photo-luminescence maximum is red-shifted by approximately 40 nm. For the PQP, the optical absorption maximum is observed at 300 nm, while the photo-luminescence maximum is found at 401 nm.[149]

Our measurements on the PMP and PQP materials can be also be compared with similar measurements by Grem et al.[33] and others[137,138] on PPP. A detailed discussion of this data will be presented in Chapter 7. At least one result may be anticipated in advance. It is well known that upon reduction of the conjugation and bond length alternation, the gap, 2Δ, decreases. Thus, it is expected that the semiconducting gap of PMP will be larger than that of PPP. Solution measurements of these quantities in PMP bear out this supposition.[148]

Promising results have already been obtained on the poly-3-alkylthiophene system, and thus, this material has enjoyed significant attention recently. The optical absorption has been well-studied,[150] and the poly-thiophene and alkyl-substituted poly-thiophenes have been shown to support polaronic structure.[151,136,131] The thermochromic properties of this material have also engendered special interest.[150] In ad-

dition, visible light emission has recently been observed from thiophene based diode devices.[34] It is a natural extension of this work to combine the thiophene emitter unit with a phenylene emitter unit, as we have begun to do here.

The (2-thienyl)phenylene (PBTP) materials are another class of potential light emitting polymers. The side chains (shown in Fig. 4) have been carefully selected to alter the band gap of the main-chain polymer, due to their electron-withdrawing or electron-donating behavior. The long side chains are also expected to result in steric hindrances, which may twist the main-chain backbone from a more planar configuration, thus isolating the potential emitter units. As in the phenylene based polymers, these materials are expected to support a bipolaron defect, but their mobility may be limited due to out of plane twisting. Hence, the PBTP system is another material in which we believe that the polaron exciton will be localized in a discrete unit.

Recently, the PBTP system (substituted with a wide variety of electron-donating and withdrawing substituents) has been the subject of an extensive investigation.[152] Absorption spectra identified these materials as wide band gap semiconductors. Upon oxidative doping, the spectra of the PBTP compound with dodecyloxy substituents display the characteristic inter-gap features indicative of polaron, and finally bipolaron, formation. With the hexyl side group, the PBTP materials do not dope. This is because local steric considerations hinder the formation of a planar main-chain geometry, which is necessary for charge defect stabilization. In addition, symmetrically substituted PBTP materials, such as those in Fig. 4 were observed to exhibit significant long range ordering, as evidenced by X-ray and DSC.

Together, the various polymers allow us the opportunity to systematically assess the idea of a discrete emitter center, as well as to ascertain the effect of variations in the chemical structure upon the light emitting properties of two potentially interesting families of materials.
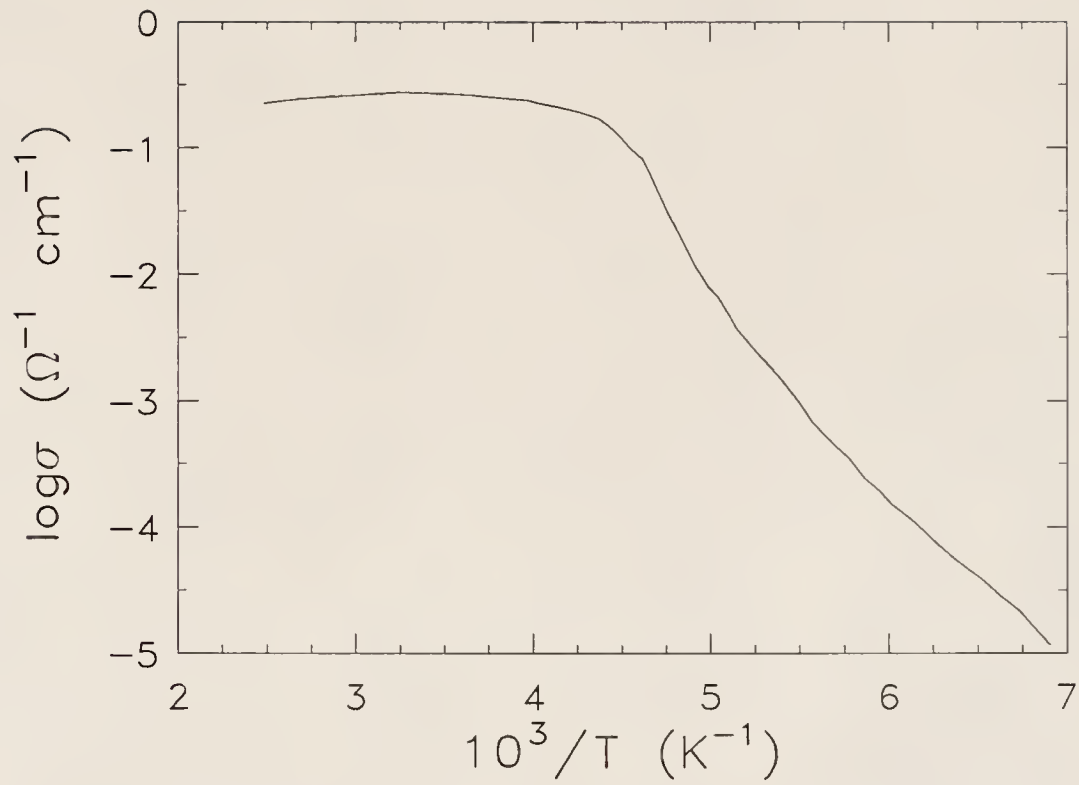
Fig. 12. Log of dc conductivity *vs* inverse temperature along the TCNQ chain direction for NPrQn(TCNQ)$_2$.
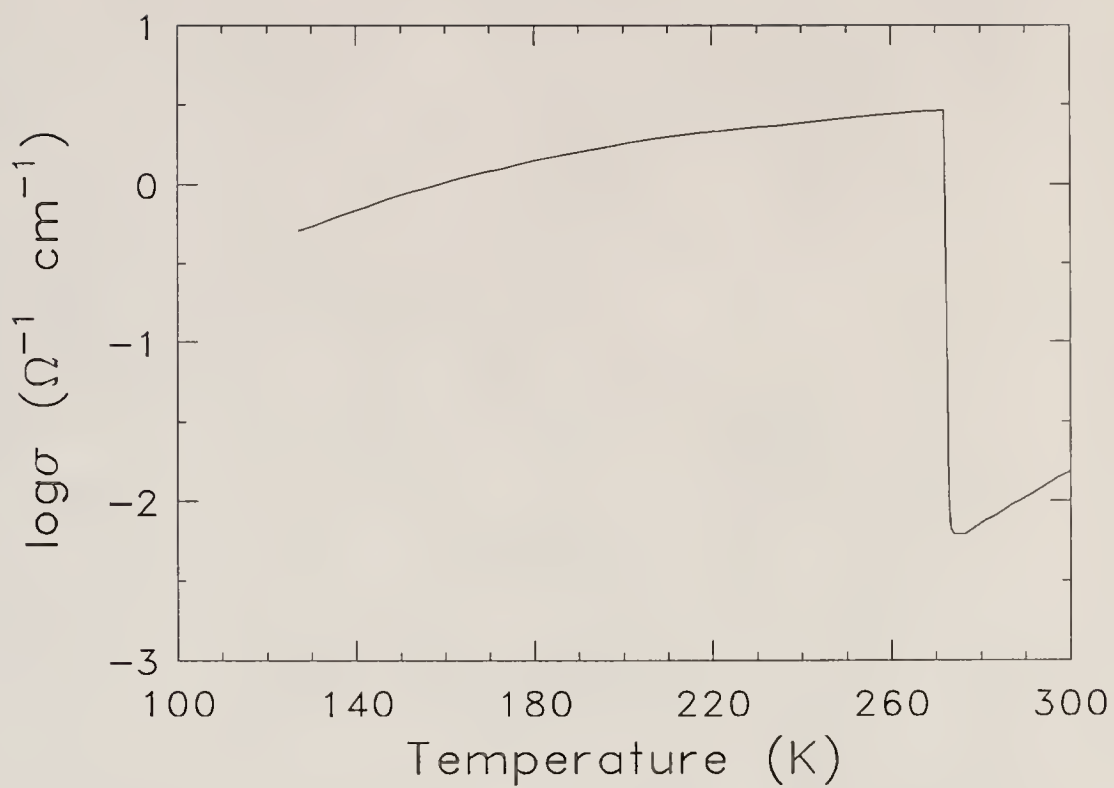
Fig. 13. Log of DC conductivity *vs* temperature along the c* direction for DMTM(TCNQ)$_2$.

Fig. 14. Band structure modifications of the proposed crystal field distortion, which is thought to occur in the b crystallographic direction.
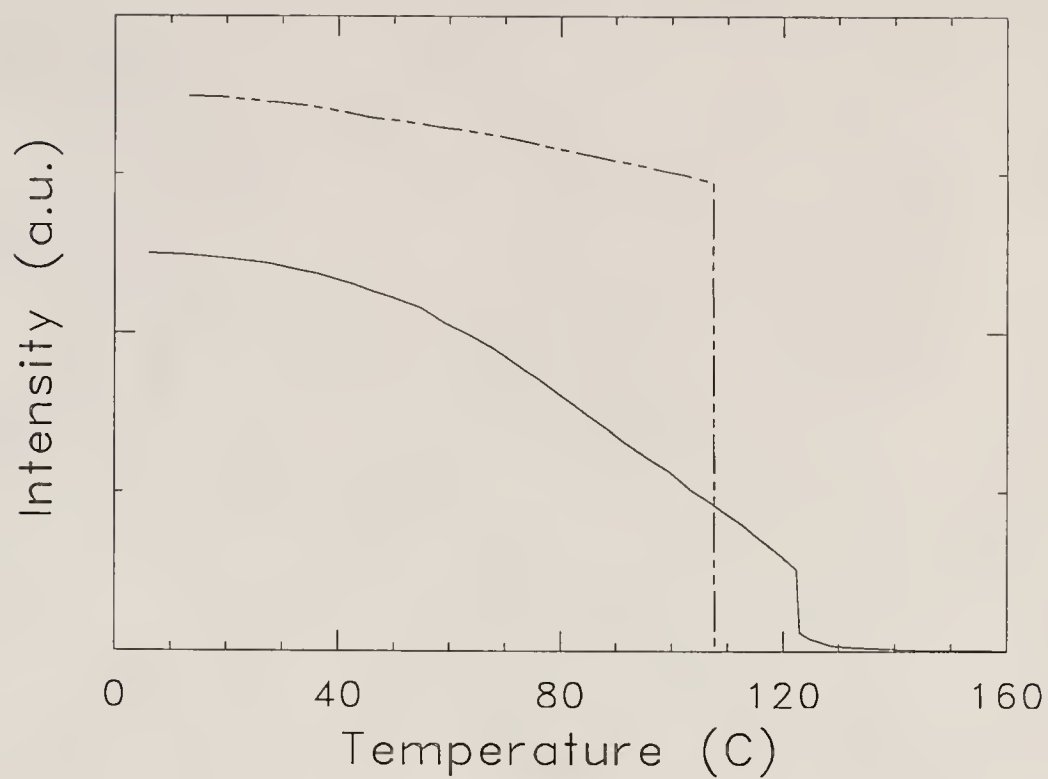
Fig. 15. Temperature dependence of the superlattice X-ray intensity.[17] Solid line: K-TCNQ; Dashed line: Rb-TCNQ.
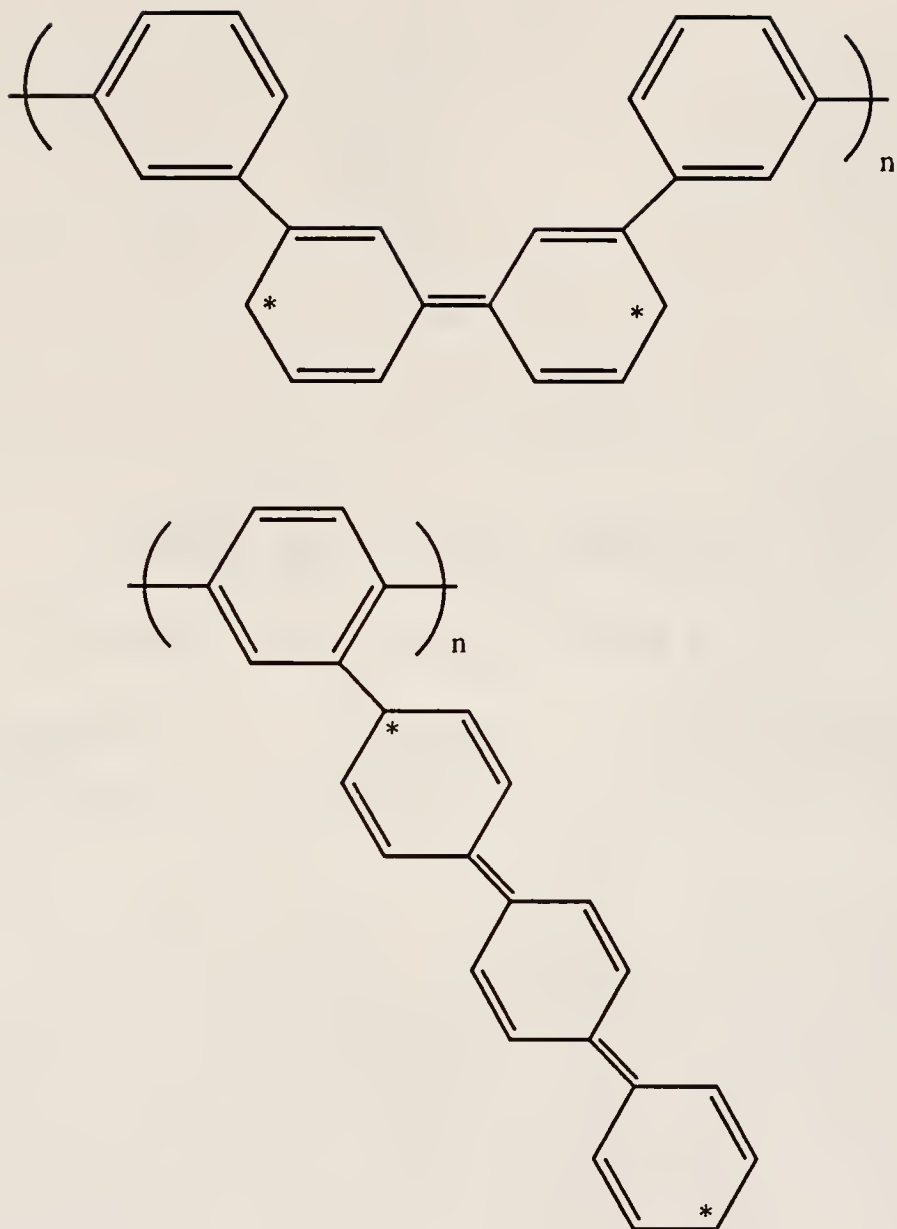
Fig. 16. Neutral bipolaron charge defects. Upper panel: PMP, lower panel: PQP.

CHAPTER IV
EXPERIMENTAL TECHNIQUES

This chapter will detail the experimental methods and apparati used in this work. It is divided into two sections. The first section presents a general discussion of the spectrometers, the temperature and polarization control, the sample mounting procedures and the data analysis techniques used in the investigations of the organic charge transfer salts. The second section describes, more briefly, the spectrometers, the electro-luminescence circuit and apparatus, and the device preparation techniques used in the investigations of the luminescent polymers.

Fourier Transform Infrared Spectroscopy

General

Fourier transform spectroscopy has several advantages over conventional grating-based spectroscopy.[153] These include: the multiplex advantage, the stability, the ability to easily average multiple scans, as well as the increased speed at which data can be obtained. These advantages result in an increased signal to noise ratio as compared to a conventional grating machine.

A simple, two-armed interferometer (Fig. 17) will be used to discuss the general principles of interferometry. In this diagram, the wave traveling from the light source, is split into two components at the central beamsplitter. When the reflected beams are recombined, they have a phase difference, $\phi = 2\pi\omega x$, due to the path difference of the moving mirror. Thus, the signal (or *interferogram*) is eventually detected as a

function of this optical path difference. The interferogram is written as

$$I(x) = \int_{-\infty}^{+\infty} S(\omega) \exp^{-i2\pi\omega x} d\omega + I_\infty, \qquad (43)$$

where x is the path difference, $S(\omega)$ is the spectral distribution function, and I_∞ is the intensity at infinite path difference (the average value of the interferogram). In the ideal case, $I(x)$ is symmetric about $x = 0$, x runs from $-\infty$ – $+\infty$. and the sampling is carried out continuously as a function of path difference. Thus, the spectrum may be obtained directly by an inverse Fourier transform of the collected interferogram:

$$S(\omega) = \int_{-\infty}^{+\infty} I(x) \exp^{i2\pi\omega x} dx. \qquad (44)$$

The advent of fast computers and the development of the fast Fourier transform algorithm has made such a computation routine.

In practice, several approximations and assumptions are essential to the act of measuring the interferogram as well as to the computation of $S(\omega)$ using Eqn. (44). The most common limitations to be addressed in measuring the interferogram include:

1. the finite path of the movable mirror.

2. accurate determination of the zero path difference position of the movable mirror.

3. the discrete nature of $I(x)$ due to non-continuous sampling.

These limitations cause various aberations in $I(x)$, which result in a distortion of the true spectrum. The nature of these non-idealities are well documented.[153-156] Each of these limitations and their common corrections will be discussed briefly below.

The finite path difference, Δ, of the movable mirror is probably the single most important limitation in Fourier transform spectroscopy, as it results in a truncation of the complete interferogram at $x = \pm\Delta$, rather than $x = \pm\infty$. This truncation

introduces large side lobes (or "feet") into $S(\omega)$. Apodization of the interferogram removes these lobes.[153] At the same time, convoluting an apodization function with the interferogram reduces the spectral resolution. A wide variety of apodization functions are commonly used.[153] The choice of apodization function is critical— not only for the removal of the lobes but for the degree of broadening and spectral distortion which is incurred in the procedure. Thus, we see that the resolution of a Fourier transform spectrometer is limited in part by the maximum path difference.

The accurate determination of the zero path difference position of the movable mirror is critical to the collection of the interferogram, $I(x)$. An accurate determination of the $x = 0$ position is essential to properly locate $I(x)$ on the x axis, thus preserving the symmetry of the interferogram. The location of the zero path difference of the movable mirror is also used for other purposes. For example, the $x = 0$ position is needed to center the truncation and apodization functions. Improper positioning of these functions with respect to the $x = 0$ position will result in asymmetry of the interferogram.

Phase errors result from the asymmetry of the interferogram, when $I(x) \neq I(-x)$. In terms of the spectral distribution function, this translates into $S(\omega)$ having an imaginary part, which is physically unreasonable. Commonly, phase error is the result of an inaccurate determination of the zero path difference of the movable mirror, but it can also result from misalignment of the spectrometer. A method for the correction of phase errors has been discussed in detail elsewhere.[24]

Eqn. (44) also assumes that the user has collected an interferogram which is a continuous function of path difference, x. In practice, the interferogram is sampled at small intervals along the positive path difference $x = k\delta$, where k either zero or an integer. The Nyquist sampling theorem puts an upper limit on the frequency spectrum as $\omega_{max} = \frac{1}{2\delta}$. This limit defines the largest sampling interval, δ, that can be used to

prevent aliasing in the frequency spectrum. The finite sampling consideration also introduces a high frequency limit to the spectrum. Electronic filtering of the signal removes frequencies which are higher than the maximum cut-off frequency.

Bruker 113V

A Bruker 113V Fourier transform infrared spectrometer (FTIR) was used to measure the polarized reflectance of the various samples in the 30–4000 cm^{-1} frequency regime. Figure 18 displays a ray and block diagram of this instrument. For discussion purposes, we will divide the spectrometer into four chambers: the source housing, the optical bench, the sample area and, finally, the detection area.

Our FTIR is equipped with two sources: a mercury arc lamp and a globar, for use in the far and mid-infrared, respectively. An adjustable aperture allows the light into the optical bench.

The main components of the interferometer are a two-sided, moveable mirror, the various beam splitters, and two independent interferometers. The beam splitters are mounted on a rotating wheel, allowing beam splitter changes without a break in the vacuum. The various beam splitter materials, thicknesses, and efficiencies for each spectral region, as well as other operating parameters, are shown in Table 1. As in Fig. 17, the divided beam returns to the beam splitter with a known path difference caused by the moving mirror. Two smaller interferometers occupy less visible positions on the optical bench. A HeNe laser reference interferometer monitors the path difference of the movable mirror. A white light source is used to determine the zero path difference position of the moveable mirror. Optical filters can also be rotated into the beam path, depending on the frequency region. For example, a black polyethylene filter is used to block the near-infrared and ultra-violet radiation from the mercury arc source, whereas a wire "mesh" can be used to partially block the

beam, thereby reducing its intensity. Concave spherical mirrors focus light onto the beamsplitter and onto the adjustable exit aperture.

There are two sample chambers in our FTIR. For transmission measurements, the reference and sample are placed directly at the focal point. For reflectance measurements, we use the reflectance stage, diagramed in Fig. 19. Alignment of the stage makes reflectance measurements more difficult. A series of concave and flat mirrors direct the light through the polarizer and into the detection chamber.

In the far infrared, a liquid helium cooled Si bolometer (Infrared Laboratories) was used as the detector. In the mid-infrared, a room temperature pyroelectric deuterated triglycine sulfate (DTGS) detector or helium cooled (4.2 K) Si:B photocell, also from Infrared Laboratories, was used to collect the signal. The helium cooled detectors were used for most work due to their high sensitivity. A diagram of the helium cooled detector is shown in Fig. 20.

Because the two-sided mirror moves at a constant velocity, v, the optical path difference may be re-written as $x = 4vt$, where t is the time that the mirror has traveled from the zero path difference position. In this way, the infrared frequency radiation is converted to a radio frequency signal. The aforementioned detectors actually produce an audio (rather than infrared) frequency signal.

After amplification, electronic filtering and digitization, the signal is sent to an Aspect computer. Here various apodization and phase corrections are applied, and the interferogram is Fourier transformed into the single beam spectrum.

The spectra are taken under vacuum. Sufficient time is allowed for thermal equilibrium of the detector, beamsplitters and other optical bench components before commencing measurements.

Optical Measurements: the Perkin-Elmer Grating Spectrometer

A modified Perkin-Elmer 16U grating spectrometer was used to obtain spectra from the mid-infrared through the ultra-violet (800–30000 cm^{-1}). Unlike FTIR, each frequency is sampled sequentially; signal averaging is done by taking multiple readings at each frequency.

Figure 21 displays a ray and block diagram of the instrument. The operation and calibration of this instrument has been described in detail elsewhere.[157] so here. I will only briefly outline the main components and operating principles for this spectrometer.

Three different light sources are positioned in a water cooled housing. These are the globar, quartz tungsten, and dueterium arc lamp, respectively. Upon leaving the source housing, the beam passes through a chopper and a series of filters. The chopper creates a square wave signal, which is easily amplified by a lock-in amplifier. The long-pass and band pass filter eliminate higher (unwanted) orders of diffraction. Next, the beam is directed through the monochromator entrance slit towards the grating. Diffraction of the light at the grating is the most critical element of this process, as the grating angle and grating constant uniquely determine the frequency of light which is allowed to pass out of the exit slit and into the rest of the spectrometer.

The relationship between grating angle and the frequency of diffracted light can be derived as follows.[158] The general equation relating the angle of incidence and diffraction to the wavelength of diffracted light is

$$m\lambda = d(\sin i + \sin D),\tag{45}$$

where m is the spectral order, λ is the wavelength, d is the spacing between grating lines, and i and D are the angles of incident and diffracted light, respectively. As

shown in Fig. 22, both angles, i and D, are measured with respect to grating surface normal; the grating angle, ϕ, is measured from the zero position. Writing i and D in terms of ϕ, we obtain

$$m\lambda = d(\sin(\phi + \frac{\delta}{2}) + \sin(\phi - \frac{\delta}{2})) = 2d\sin\phi\cos\frac{\delta}{2}, \qquad (46)$$

where δ is the angular separation of the entrance and exit slits. Rearranging, setting $m = 1$ and substituting for wavenumbers in terms of frequency, we obtain

$$2\omega d\cos\frac{\delta}{2} = \csc\phi. \qquad (46)$$

For our monochromator, $\delta = 4°$, so $\cos\frac{\delta}{2} \approx 1$. Thus, the angle of the grating is then related to the energy of the diffracted light (in wavenumbers) as

$$2\omega d = \csc\phi. \qquad (47)$$

The quantity

$$\frac{1}{2d\cos\frac{\delta}{2}} \qquad (48)$$

is usually defined as the grating constant.

During normal operation, a stepping motor moves the grating (at predetermined intervals consistent with the necessary spectral resolution) from one position to the next. The angle of rotation together with the exit slit-width determine the resolution of the monochromator.[158] For our machine, $\frac{\Delta\omega}{\omega} \approx 0.1\%$.[157]

After exiting the monochromator, the beam is focussed onto position $\mathcal{R}$, using a large spherical mirror. A second large spherical mirror focuses the light onto the detector. Three detectors were used in these measurements: a thermocouple with

a KBr window, a room temperature lead sulfide detector, and a Si photocell. The chopped signal is amplified by an Ithaco Model 393 lock-in amplifier, and then sent to a Fluke Model 8520A digital voltmeter. The signal average processes occur at the Fluke. The various operating parameters of the Perkin-Elmer are summarized in Table 2.

Note that the Perkin-Elmer spectrometer can be used in reflection or transmission mode. In reflection mode, the reference mirror and sample are both positioned at position $\mathscr{R}$. A single beam spectra is obtained for the aluminum reference mirror; then the sample is rotated into position, and the single beam spectra of the sample is recorded. The ratio of these two single beam spectra define the sample reflectance. It is common practice to correct for sample roughness and the reflectivity of the Al reference mirror by coating the sample with 2000 Å of Al, remeasuring the single beam spectra, and computing the following ratio:

$$R(\omega) = \left(\frac{\frac{S_{samp}}{S_{mirror}}}{\frac{S_{coatsamp}}{S_{mirror}}} \right) R_{Al},$$

(49)

where S_{mirror} and S_{samp} are the single beam spectra of the mirror and sample, respectively, and R_{Al} is the absolute reflectance of aluminum. In transmission mode, an aluminum reference mirror is placed at position $\mathscr{R}$, and the reference and sample are placed at the focal point in position $\mathscr{T}$.

The entire spectrometer can be evacuated to pressures below 150 millitorr. This is especially important in the mid- and near-infrared frequency regime, where absorption of water or CO_2 is readily evident in the spectra.

Temperature and Polarization Control

General

The copper sample holders, upon which the crystals are mounted, consist of a small hole surrounded by a conical face; these sample holders were mounted on an adjustable copper frame. The frame was attached to the cryostat tip.

A Hansen and Associates High-Tran cryostat, transfer line and Model 8000 temperature controller were used for the non-ambient temperature experiments. The temperature sensor itself is a calibrated Si diode, which is embedded in the cryostat tip. The cryostat also contains a heating element. The cryostat tip is surrounded by a vacuum shroud, which is evacuated with a diffusion pump to prevent ice from forming on the sample. The shroud has either a polyethylene or KCl window to transmit far or mid-infrared light, respectively. A transfer line is used to move the liquid helium from the storage dewar through the cryostat. The helium gas is recovered for re-use. Flow meters control the flow of helium through the system.

To correct for the effect of the shroud window and any slight alignment differences caused by insertion of the transfer line, we normalize our temperature dependent spectra with respect to the room temperature spectrum taken without a window and corrected for the finite reflectance of the aluminum reference mirror, as previously discussed. This renormalization is given as:

$$R(\omega, T) = \frac{R(\omega, T, win)}{R(\omega, 300, win)} R(\omega, 300). \qquad (50)$$

The polarizers used in the Bruker FTIR are wire grid polarizers, mounted in oriented polyethylene and AgBr for the far and mid-infrared, respectively. Polarizers rotate in or out of the beam path, and the orientation is easily changed using a gear mechanism.

The polarizers used in the Perkin-Elmer spectrometer are wire grid, dichroic, and plastic polarizers, for the infrared, near infrared and visible frequency regions, respectively. These polarizers may be moved in and out of the beam path using external (to the vacuum tank) spring-loaded cables. The position of the polarizer monitored using a potentiometer readout. The orientation of the polarizer is determined from a calibration of the potentiometer with respect to a polarizer of known orientation.

Measurements on the Charge Transfer Salts

Near normal polarized reflectance measurements were made on the large face of single crystal samples of NPrQn(TCNQ)$_2$, K- and Rb-TCNQ. Experiments were performed in two polarizations on the large crystal faces: with light polarized parallel and perpendicular to the TCNQ chain axis.

DMTM(TCNQ)$_2$ represents a special case, as several of the crystal facets were large enough to permit investigation. Figure 23 depicts the typical crystal shape and labels the crystallographic faces of DMTM(TCNQ)$_2$. Note that the a/c plane defines the (010) face of the sample. Here, we report our measurements on the (010) and (110) faces. Experiments were performed with light polarized parallel and perpendicular to the maximum reflectance on each unique crystal face. Symmetry requires that two of the principal axes of the high temperature phase lie on the (010) crystal face. Once the optic axes were found at 300 K, the polarizer position remained unchanged for all temperatures studied.

For each polarization, infrared measurements (30-4000 cm^{-1}) were made at several temperatures ranging from 10 K to 420 K, concentrated around T_c. For the quarter-filled salts, data in the near-infrared region (4000–15000 cm^{-1}), were collected at $\approx$ 100 K and 300 K. Reflectance measurements for the visible frequency region (15000–30000 cm^{-1}) were obtained at room temperature. Thus, the total frequency range of data collection ran from 40 to 30000 cm^{-1}. For the K- and

Rb-TCNQ samples, complementary data for the near-infrared and visible frequency region (3000–20000 cm^{-1}), were obtained from various literature sources, and used as a high frequency extrapolation in this study. Thus, the total frequency range of reflectance data available ran from 30 to 20000 cm^{-1} for the half-filled charge transfer salts.

Sample Preparation and Mounting—Organic Charge Transfer Salts

The NPrQn(TCNQ)$_2$ single crystal samples were prepared by the method of Melby et al.[2] by Dr. Katalin Kamarás at the Central Institute for Research in Budapest, Hungary. These crystals were precipitated from an acetonitrile solution by slow cooling. Typical sample dimensions were $\approx 4 \times .5 \times .5$ mm^3.

The DMTM(TCNQ)$_2$ single crystals were prepared by Dr. Manuel Almeida at the National Laboratory of Engineering and Industrial Technology, Portugal. In this reaction, TCNQ was reacted with the cation iodide in boiling acetonitrile under a nitrogen atmosphere.[2] Large single crystals, up to $\approx 5 \times 5 \times 1.5$ mm^3 were grown by slow cooling of deaerated saturated and seeded solutions under dry nitrogen, using a technique similar to that previously described for other complex TCNQ salts.[159,160]

Under a microscope, both the NPrQn(TCNQ)$_2$ and DMTM(TCNQ)$_2$ samples were smooth, so no attempt was made to coat the surface with aluminum to correct for scattering loss. Such losses are expected to be more important at high energy.

Needlelike single crystals of K-TCNQ and Rb-TCNQ(I) were prepared by the reaction of TCNQ with the cation iodide in acetonitrile by Dr. Yoshihiro Iwasa at the University of Tokyo, Japan.[2] Typical sample dimensions were $\approx 8 \times .4 \times .4$ mm for the potassium salt, and $\approx 7 \times 1 \times 1$ mm for the rubidium salt.

Because of the small sample size, two K-TCNQ crystals were mounted adjacently on the sample holder to form a mosaic, thus increasing the effective sample size. The

absolute level of the reflectance was obtained by coating the surface of the crystals with aluminum to correct for scattering loss and the area between crystals of the mosaic.

Due to the violent first-order nature of the structural phase transition, a different approach was taken with the Rb- compound. In this case, a single Rb-TCNQ crystal was mounted on two thin copper wires, which were secured to the copper sample holder. The flexibility of the copper wires allowed for the thermal expansion of the crystal, thus preventing *complete* breakage at T_c. It is important to note that the sample *did* break and fissure at T_c due to internal (and external) stresses. The absolute level of the reflectance for these spectra was determined as follows. First, the absolute level of the reflectance was determined at room temperature with the sample the same size as the reference mirror. Here, the Rb-TCNQ sample was smooth, so no aluminum correction was used. In the low temperature phase, spectra were ratioed to the 300 K spectrum in the customary manner. Due to the surface cracking and sample breakage, we do not know the true absolute level of reflectance in the high temperature phase. It would have been highly desirable to coat the crystal with Al, and thus, renormalize for these effects. Unfortunately, due to the delicacy of the crystal, this was impossible. Making an educated guess, we renormalized these spectra above T_c to be consistent with the level and trend below T_c.

Analysis of Reflectance Spectra

The Kramers-Kronig Transform

Optical constants presented in this dissertation were obtained by Kramers-Kronig analysis of the power reflectance spectrum.[161,162] This analysis gives the complex dielectric function

$$\epsilon(\omega) = \epsilon_1(\omega) + i\epsilon_2(\omega) = \epsilon_1(\omega) + \frac{4\pi i}{\omega}\sigma_1(\omega), \tag{51}$$

where ϵ_1 is the real part of the dielectric function and σ_1 is the frequency dependent conductivity. These properties are fundamental material characteristics, as they effectively define its optical response to light.

The Kramers-Kronig relations are based upon the requirement of causality and the fact that the real and imaginary parts of a response function are always related through a dispersion relation.[161,162] For reflectance measurements, the response function is

$$r(\omega) = \frac{E_{refl}}{E_{incid}} = \rho(\omega) \exp i\Theta(\omega). \tag{52}$$

The measured reflectance is

$$R(\omega) = \left| \frac{E_{refl}}{E_{incid}} \right|^2 = \rho^2(\omega), \tag{53}$$

and the phase shift upon reflection is calculated from

$$\Theta(\omega) = \frac{\omega}{\pi} \int_0^\infty \frac{\ln R(\omega') - \ln R(\omega)}{\omega^2 - \omega'^2} d\omega'. \tag{54}$$

Although our data was collected over a wide frequency range, extrapolation beyond the frequency interval of interest is necessary, as the integral in Eqn. (54) extends from zero to infinity. The details of these extrapolations and the effect upon the resulting optical constants are the subject of the next brief sections.

Using

$$r(\omega) = \frac{(n-1) + i\kappa}{(n+1) + i\kappa}, \tag{55}$$

one can obtain the real and imaginary parts of the complex refractive index. The refractive index, n, is given as

$$n(\omega) = \frac{1 - R(\omega)}{1 + R(\omega) - 2\sqrt{R(\omega)} \cos \Theta(\omega)}, \tag{56}$$

and the extinction coefficient, κ, is given as

$$\kappa(\omega) = \frac{2\sqrt{R(\omega)}\sin\Theta(\omega)}{1 + R(\omega) - 2\sqrt{R(\omega)}\cos\Theta(\omega)}. \tag{57}$$

These relationships can be re-cast in terms of the dielectric function, $\epsilon(\omega)$. Since $N = \sqrt{\epsilon}$ for a non-magnetic material,

$$\epsilon = N^2 = (n + i\kappa)^2. \tag{58}$$

The real part and imaginary parts of $\epsilon(\omega)$ are

$$\epsilon_1(\omega) = n^2 - \kappa^2 \tag{59}$$

and

$$\epsilon_2(\omega) = 2n\kappa. \tag{60}$$

The real part of the dielectric function describes the dispersion of the carriers, while the imaginary part of $\epsilon(\omega)$ describes the attenuation of the carriers.

The absorption coefficient, α, can be obtained as

$$\alpha(\omega) = \frac{2\omega\kappa}{c} = 4\pi\kappa\omega. \tag{61}$$

Thus, by Kramers-Kronig analysis of reflectance data, we can obtain the optical constants of a material, which effectively characterize its response to light.

Method of Extrapolation

The high frequency extrapolation is actually comprised of two distinctly different regimes: the interband region, where there is some (unknown) contribution to the overall oscillator strength from interband transitions, and the higher energy free electron region. In the interband region, from 30000–1.0×10^6 cm^{-1}, the reflectance is modeled as

$$R(\omega) = R_f\left(\frac{\omega_f}{\omega}\right)^s, \tag{62}$$

where R_f and ω_f are the reflectance and frequency of the last measured data point, and s is an adjustable parameter typically taking on a value between zero and four. Above 1.0×10^6 cm^{-1}, free electron behavior, given by

$$R(\omega) = R_{f'}\left(\frac{\omega_{f'}}{\omega}\right)^4, \tag{63}$$

is assumed.[161,162] Hence, the high frequency extrapolation of the Kramers Kronig analysis has two adjustable parameters: s, the interband exponent, and $\omega_{f'}$, the free electron frequency. A reasonable choice of these two parameters is critical to the success of this method. The high frequency extrapolation naturally affects the optical constants in the visible and near-ultra violet the most.

The method of extrapolation at low energy in Eqn. (54) must also be addressed. For semiconducting materials, it is common to approximate $R(\omega)$ as a constant to zero frequency,[161,162] as in such samples, there are no low lying excitations with large oscillator strength.

Luminescence Measurements

Sample and Device Preparation

The molecular structure of the polymers used in this study are displayed in Fig. 2 and Fig. 4. The synthesis of these materials was done by Dr. Jose Ruiz and J. Wang, under the direction of Profs. J. Reynolds and M. Pomeranz, at the University of Arlington, TX. The *meta*-linked phenylene based oligomers had molecular weights of ≈600-2000 g/mole were obtained, with polydispersity ratios on the order of 1.2-1.7.[148] In addition, they are stable in air, and remain so at elevated temperatures.[148] PBTP based samples were synthesized via oxidative polymerization, and yielded oligomers with an average degree of polymerization of about six repeat units. The polydispersity ratios were 1.69 and 2.46 for the symetrically substituted dodecyloxy- and hexyl- PBTP samples, respectively. These materials were also stable at elevated temperatures.[152] Finally, the PQP sample was obtained as an oligomeric material, and treated to remove the Cl end-groups. The details of the various synthetic methods are reported elsewhere.[148,152,149] These materials have an advantage over other previously reported potential EL polymers in that they are directly soluble in common organic solvents and thus, do not need to be converted from a precursor stage, as do PPV and some forms of PPP.[31,33]

The diode fabrication process proceeded as follows. Films were solution cast or spin coated onto indium/tin oxide (ITO) covered glass substrates. We estimate the film thicknesses to be less than 1 μm. Good quality thin films were obtained in this manner. Next, 2000 Å of aluminum was evaporated on top of the polymer film using a micro-etch. The aluminum served as a counter electrode contact. Silver paste was used to attach thin wire leads to both the ITO and Al contacts.

Photo-luminescent Measurements

The steady state photo-luminescence measurements were carried out on a modified SPEX Model 1681 fluorimeter in the laboratory of Dr. K. Schanze at the University of Florida. The spectrometer had a Xenon lamp source, two monochromators and a photomultiplier detector. Experiments were run in emission mode, using λ_{excit}=330 nm for the phenylene based polymers, and 330 and 500 nm for the thiophene-phenylene-thiophene based materials with hexane and dodecyloxy side groups, respectively.

Time resolveed PL measurements were used to determine exciton lifetimes. These measurements were done using a Photochemical Research Associates instrument (Model 1551) and a photomultiplier detector. Excitation energies were identical to those used for the steady state emission measurements. Decay profiles were measured at the emission maximum, or as close to the maximum as possible, given the availability of filters.

Electro-luminescence Measurements

The overall design showing the various components of the electroluminescence experiment in the light tight box is diagramed in Fig. 24. Measurements were run in a light-tight box that was purged with nitrogen to prevent oxidation or degradation of the polymer films under high voltage. The sample holder is mounted on an $x/y/z$ stage inside the light tight box. A computer was interfaced to automatically step the power supply and simultaneously record the resultant current-voltage characteristics and photomultiplier light intensity (as measured by Keithley digital multimeters) in a data file.

The circuit diagram for the electroluminescence experiment is shown in Fig. 25. The indium-tin-oxide (ITO) electrode was run at positive bias with respect to the Al electrode. Thus, holes were injected at the ITO electrode and electrons were injected

at the Al counter electrode, presumably combining in the film with the emission of light. Active areas were on the order of 0.4 cm^2.

Table 1. Bruker FTIR Operating Parameters

Range cm^{-1}	Beam Split. Material	Opt. Filt. Material	Source	Pol. Material	Detect.
35 - 90	Mylar	Black PE	Hg arc	1	bolometer
80 - 400	Mylar	Black PE	Hg arc	1	bolometer
100 - 600	Mylar	Black PE	Hg arc	1	bolometer
450 - 4000	Germanium on KBr	none	Globar	2	DTGS, photocell

PE = polyethylene. Polarizer 1 = wire grid on oriented polyethylene; polarizer 2 = wire grid on AgBr.

Table 2. Perkin-Elmer Operating Considerations

Range cm^{-1}	d^{-1} mm^{-1}	Lamp	Detect.	Pol.	Slit μ
801 - 965	101	Globar	TC	1,0	2000
905 - 1458	101	Globar	TC	1,1	1200
1403 - 1752	101	Globar	TC	1,1	1200
1644 - 2612	240	Globar	TC	1,1	1200
2467 - 4191	240	Globar	TC	1,1	1200
3829 - 5105	590	W	PbS or TC	1,2	225
4793 - 7822	590	W	PbS or TC	2,2	75
7511 - 10234	590	W	PbS or TC	2,2	75
9191 - 13545	1200	W	PbS or TC	2,2	225
12904 - 20144	1200	W	PbS or TC	2,2	225
17033 - 24924	2400	W	Si Photocell	2,3	225
22066 - 28059	2400	D_2	Si Photocell	3,3	700
25706 - 37964	2400	D_2	Si Photocell	3,3	700
36368 - 45333	2400	D_2	Si Photocell		700

W = tungsten halogen lamp; D_2 = dueterium lamp. Polarizer 1 = wire grid; polarizer 2 = dichroic; polarizer 3 = plastic.

M

Movable Mirror

Source

B

M

S

Beam
Splitter

D
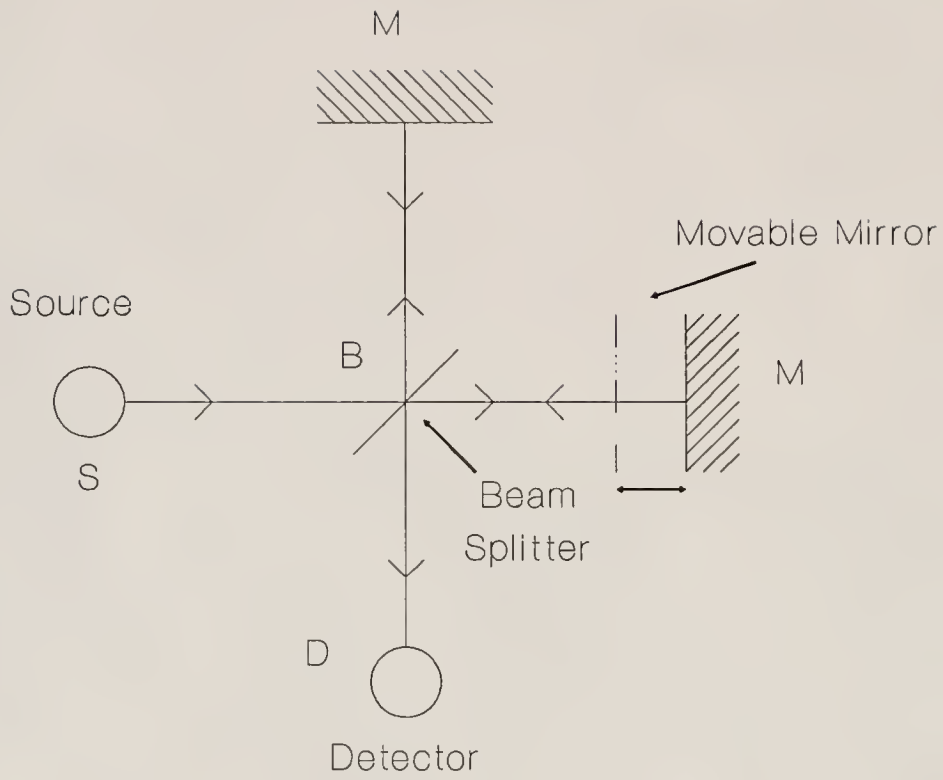
Detector

Fig. 17. Diagram of a simple two-armed interferometer.

I **Source Chamber**
a Near-, mid-, or far-IR sources
b Automated Aperture

II **Interferometer Chamber**
c Optical filter
d Automatic beamsplitter changer
e Two-sided movable mirror
f Control interferometer
g Reference laser
h Remote control alignment mirror

III **Sample Chamber**
i Sample focus
j Reference focus

IV **Detector Chamber**
k Near-, mid-, or far-IR
   detectors
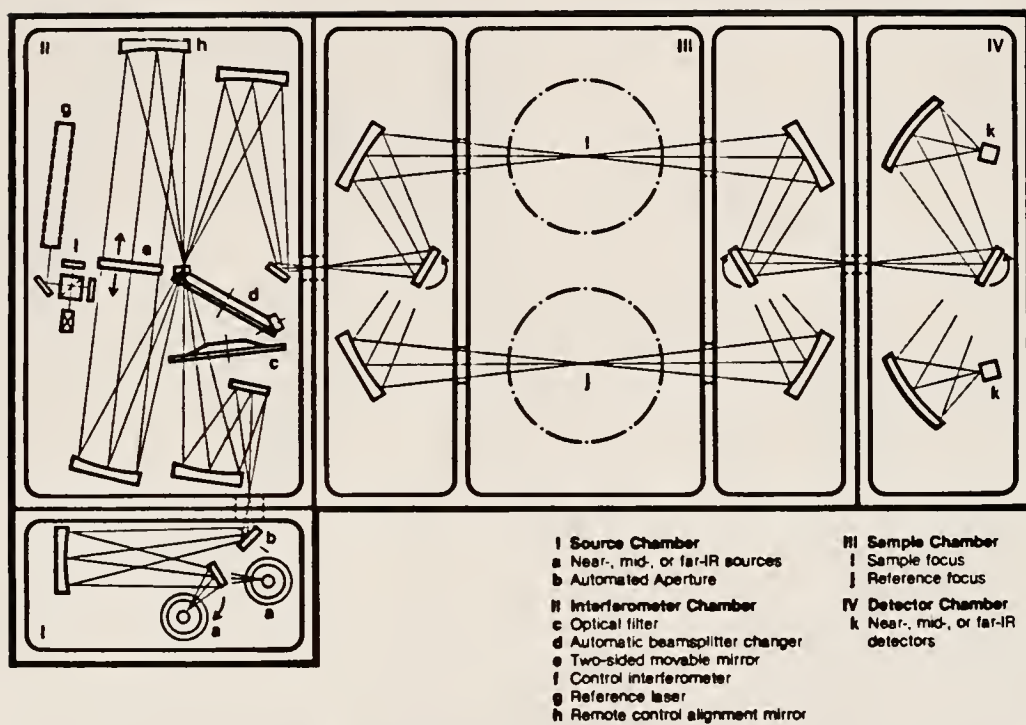
Fig. 18. Diagram of the Bruker FTIR.
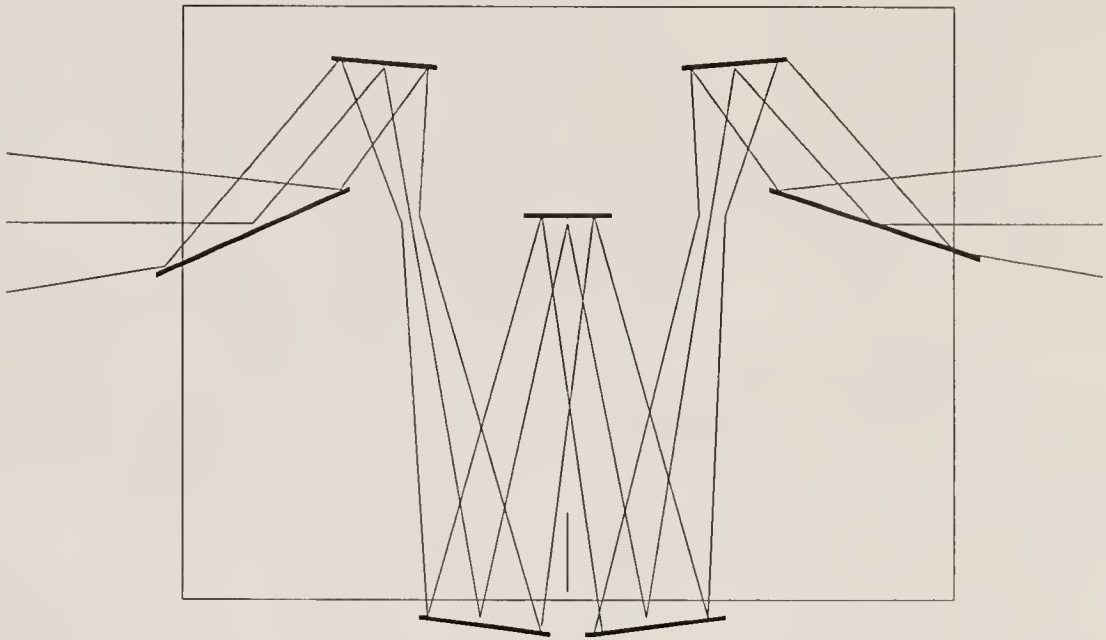
Fig. 19. Diagram of the reflectance stage used in the Bruker FTIR.
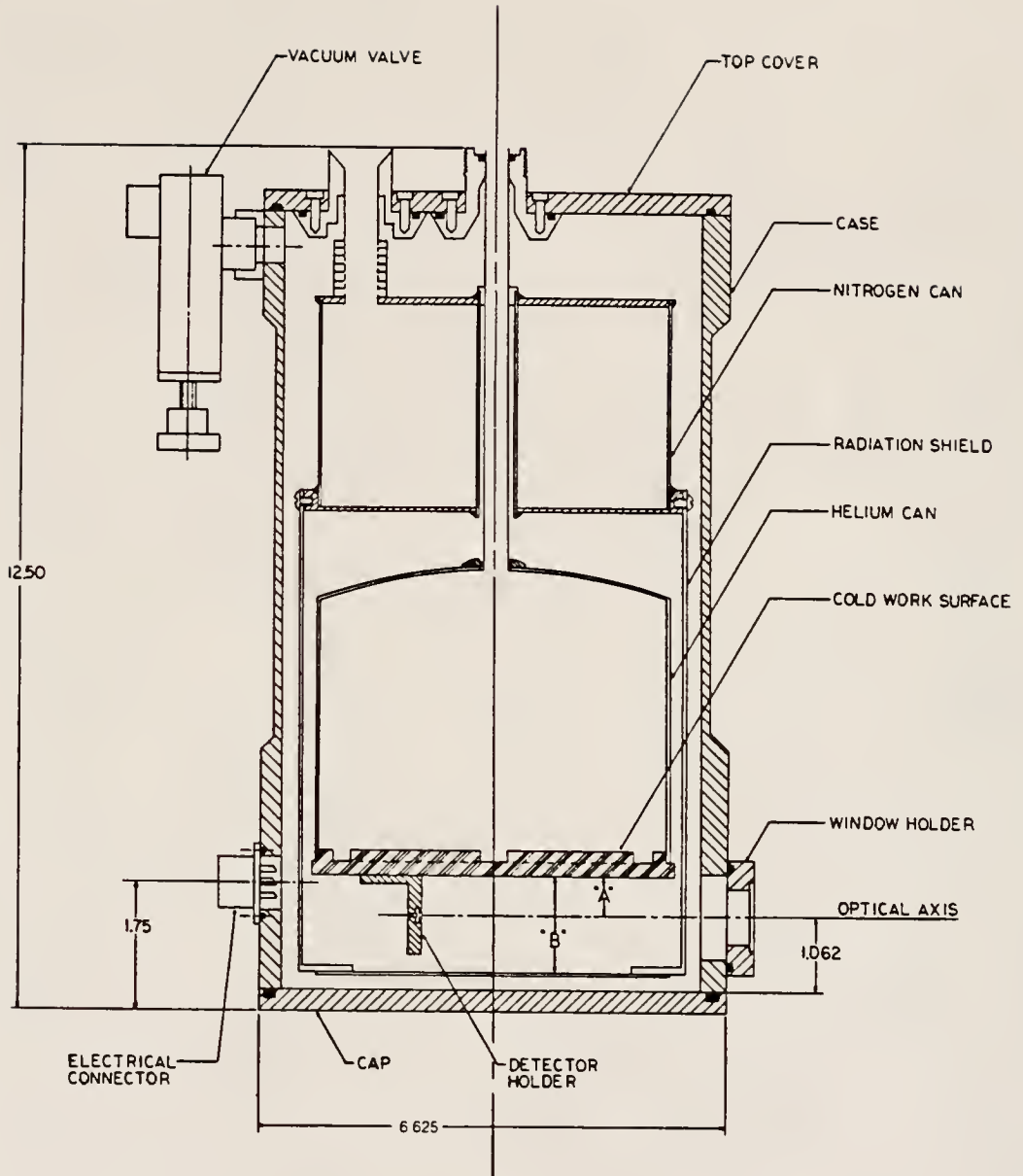
Fig. 20. Diagram of the liquid helium cooled detector used in the middle and far infrared frequency regime.
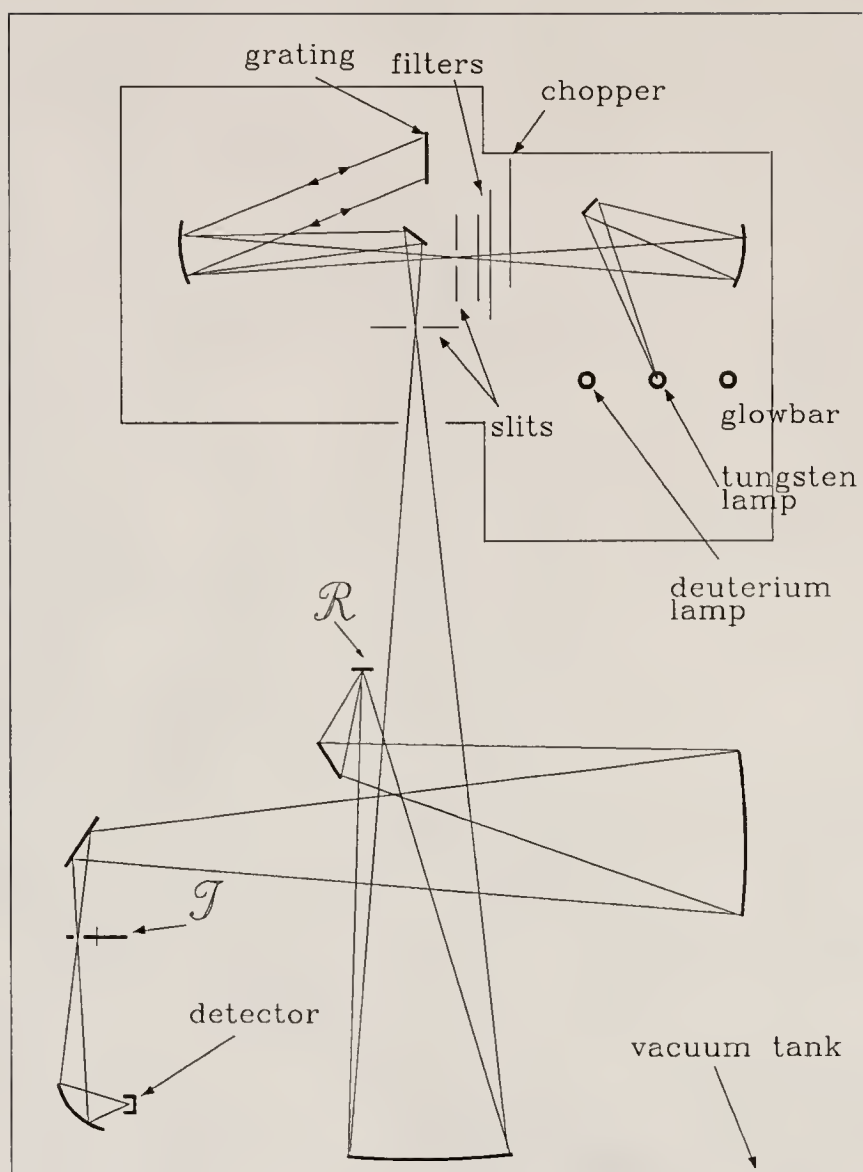
Fig. 21. Diagram of the Perkin-Elmer grating monochromater.
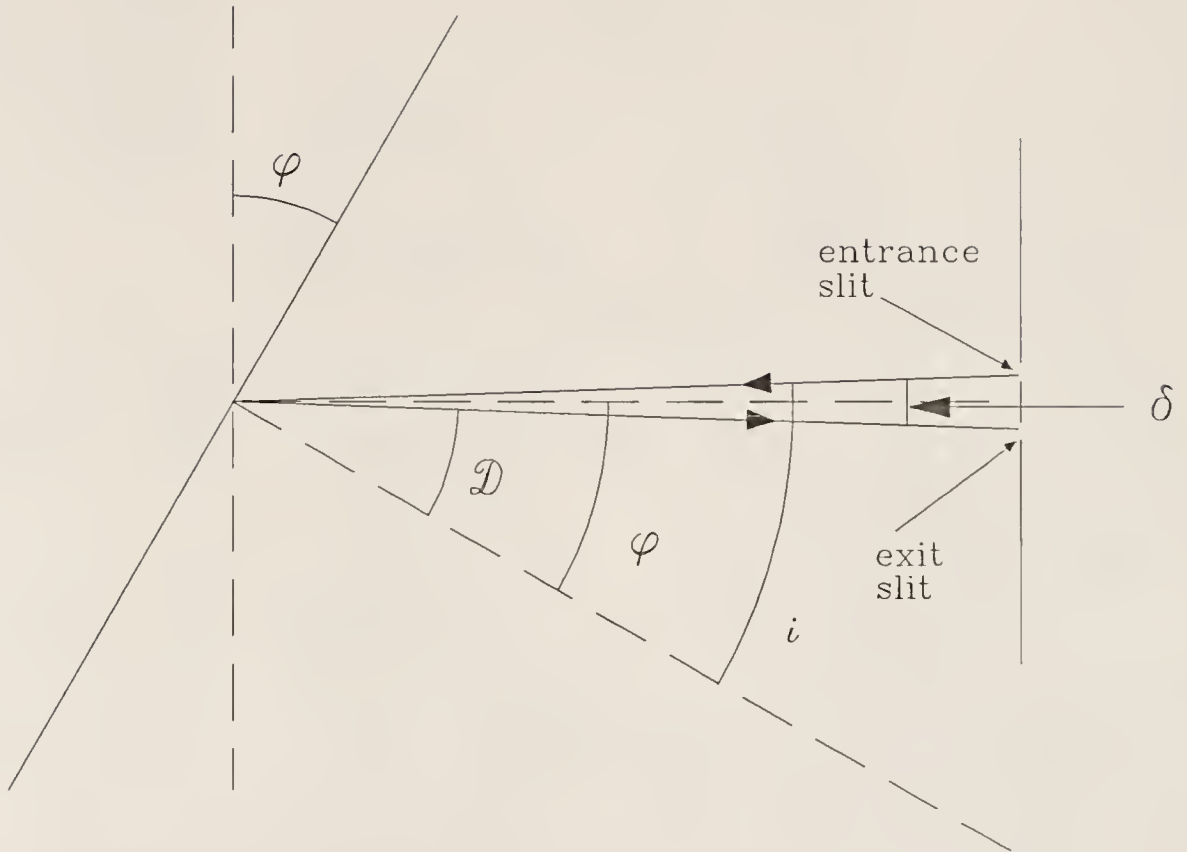
Fig. 22. Diagram of a diffraction grating, used in the Perkin-Elmer monochromater.
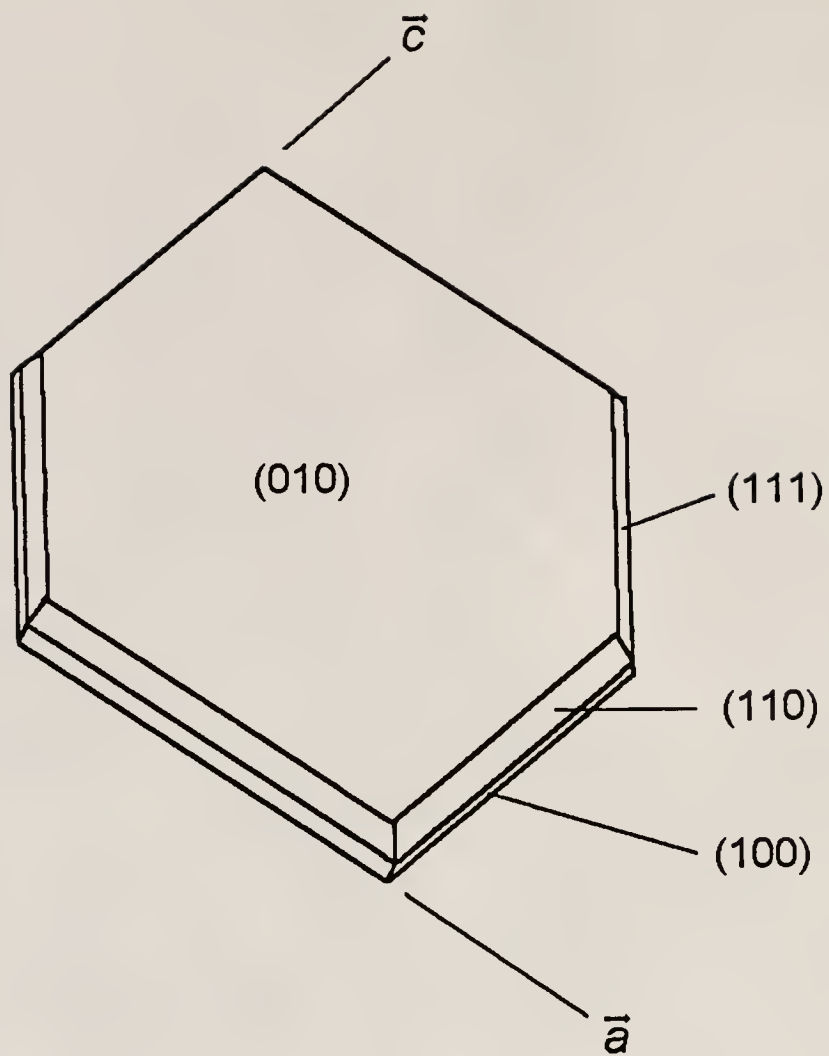
Fig. 23. Diagram of DMTM(TCNQ)$_2$ single crystal facets.
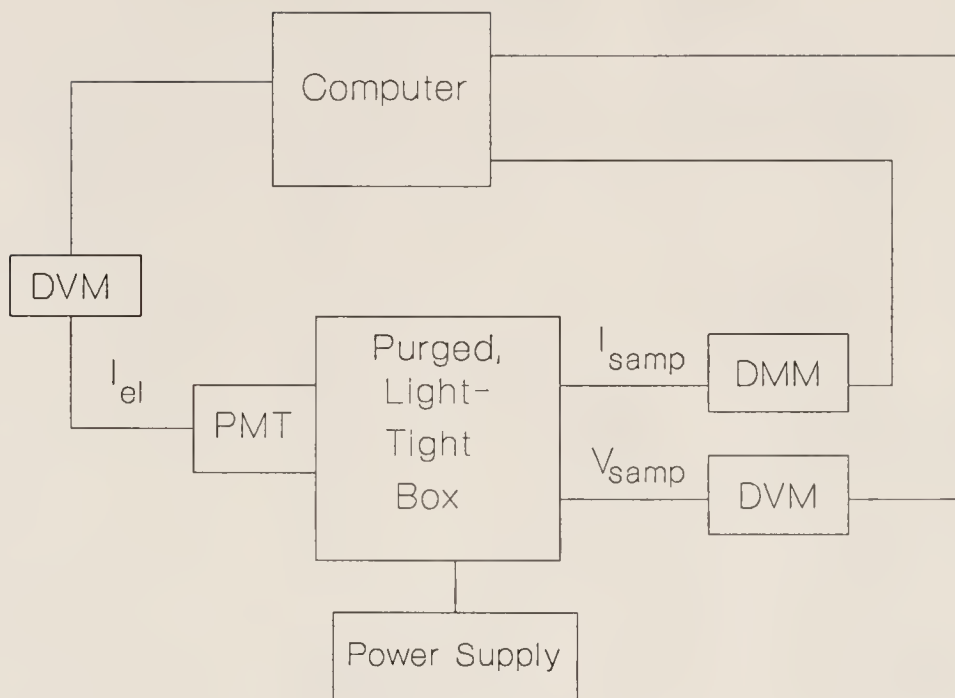
Fig. 24. Block diagram of the equipment used in the electro-luminescence experiment.
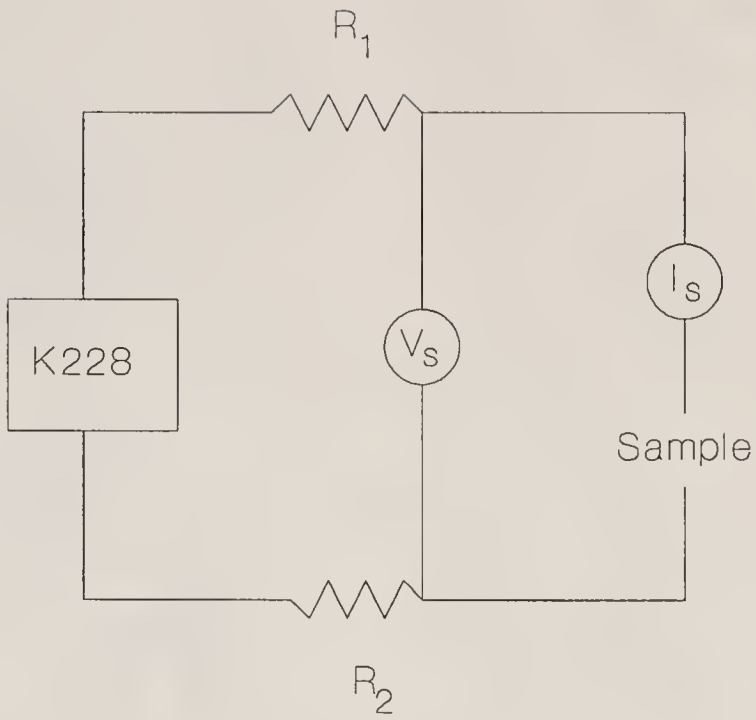
Fig. 25. Circuit diagram for the electroluminescence experiment.

CHAPTER V
RESULTS AND DISCUSSION—QUARTER-FILLED
ORGANIC CHARGE TRANSFER SALTS

Results: NPrQn(TCNQ)$_2$

Room Temperature Spectra

Figure 26 displays the room temperature reflectance of NPrQn(TCNQ)$_2$ over the entire spectral range for polarizations parallel and perpendicular to the stacking axis. For the electric field vector polarized along the TCNQ chain direction, the spectra display two electronic excitations (at $\approx 3000 \text{cm}^{-1}$ and $\approx 10000 \text{ cm}^{-1}$). The low energy band is very broad and contains a majority of the oscillator strength. These electronic features have been attributed to the transfer of charge within TCNQ tetramers in the stack.[163,79] At low frequency, the spectra display many sharp vibrational features. Ten of these modes are A_g vibrations of the TCNQ molecule, activated by coupling to the low energy charge transfer band.[164–166] Additional vibrational structure is much weaker and due to TCNQ modes of other symmetry[19] as well as those of the N-propylquinolinium donor cation.

In this polarization above T_c, the spectra of weakly metallic NPrQn(TCNQ)$_2$ show qualitative agreement with other quarter-filled, 1:2 semiconducting materials such as Qn(TCNQ)$_2$,[26] MEM(TCNQ)$_2$,[166,167] TeEA(TCNQ)$_2$,[168] TEA(TCNQ)$_2$,[75,169] and MTPP(TCNQ)$_2$[170] in terms of the position and intensity of the electronic and vibrational features. Although transport measurements show that NPrQn(TCNQ)$_2$ is weakly metallic in the high-temperature phase, the spectra are qualitatively different

from typical spectra for very highly conducting TCNQ salts. For example, low frequency features commonly associated with highly conducting salts[19,4] include high reflectivity with a weakly superimposed vibrational structure (due to the screening of conduction electrons) and a Drude relaxation. Our spectra are not well described in these terms, evidence that the pronounced tetrameric clustering in $NPrQn(TCNQ)_2$ precludes a metallic band structure and introduces a semiconducting transport gap, 2Δ. The spectra displayed in Fig. 26 are consistent with a material of low conductivity.

Perpendicular to the TCNQ stacking direction, the reflectivity is low ($\approx$10 %), flat, and almost featureless. The extreme anisotropy observed in $NPrQn(TCNQ)_2$ is observed for other TCNQ charge transfer salts as well.[18]

Temperature Dependence

The reflectance spectra exhibit gradual changes around T_c (220 K) as a function of temperature. In general, the spectral features become sharper and shift to higher frequency at lower temperature. The oscillator strength of the low energy charge transfer band increases systematically with decreasing temperature, especially in the low-temperature phase. The position of the deep minimum in the reflectivity (at $\approx$5500 cm^{-1}) is unaffected by temperature. Although the vibrational splitting appears only below T_c, it too becomes gradually more pronounced at lower temperature. No spectral hysteresis is observed upon temperature cycling.

To compare the spectral differences between the high- and low-temperature phases in the TCNQ stacking direction, the reflectivity and the frequency dependent conductivity are shown in Fig. 27 for two temperatures, 300 K and 100 K. The following discussion refers primarily to the frequency dependent conductivity.

The character of the mid-infrared charge transfer excitation is a strong function of temperature, indicating that important changes occur in the electronic state as

a result of the phase transition. This is shown in Fig. 28. In the high-temperature phase, the low energy charge transfer band is very broad (due to the possible overlap of several excitations) and centered at ≈ 2200 cm^{-1}. At 100 K, the resonance sharpens and the center frequency shifts to a higher energy, the band center moving from 2200 cm^{-1} at 300 K to 2500 cm^{-1} at 100 K. Additionally, in the low-temperature phase, this electronic band can be resolved into two components centered at 1000 and 2500 cm^{-1}, separated by a minimum at 1500 cm^{-1}. Similar behavior is observed in both the high- and low-temperature phases of MTPP(TCNQ)$_2$.[170] At the same time, the integrated oscillator strength is significantly larger at 100 K than at 300 K.

A second charge transfer band occurs at ≈ 9700 cm^{-1} for both 300 and 100 K. In both phases, it appears as a weak doublet, the doublet structure being slightly more pronounced in the low-temperature phase. However, the general shape and oscillator strength of this band are not strongly affected by temperature. Consequently, it was omitted from the narrower spectral range, displayed in Fig. 27.

The most obvious difference between the high- and low-temperature phases is the fundamental change in the infrared vibrational structure. Below T_c, each A_g phonon mode splits into a doublet, whereas no phonon splitting is observed in the high- temperature phase. Details of the typical doublet phonon structure in the low-temperature phase are presented in Fig. 29. At the lowest temperature, a well developed sideband appears above each of the principal A_g peaks in $\sigma_1(\omega)$. For ex- ample, the main peak at approximately 1280 cm^{-1} is accompanied by a sideband at approximately 1400 cm^{-1}. With increasing temperature, both sidebands and main peaks lose oscillator strength. Above T_c, the sidebands are absent. This fine structure becomes gradually more pronounced at lower temperature. Table 3 displays the un- perturbed phonon frequencies and the amount of splitting of the sideband for several

A_g phonon modes at 100 K. The unperturbed phonon frequencies were obtained from a plot of $Re\left(\frac{1}{\sigma(\omega)}\right)$, as discussed in Chapter 2.[28]

Discussion: NPrQn(TCNQ)$_2$

Electronic Features

In typical large U semiconducting materials of this class, the high energy spectral features in the TCNQ stacking direction consist of two strong, broad absorptions which correspond to electronic charge transfer between TCNQ moieties within the chain.[19,163,79] The electronic absorption band centered at 2200 cm^{-1} corresponds to the charge transfer: $TCNQ^0 + TCNQ^- \rightarrow TCNQ^- + TCNQ^0$. The breadth of this band in NPrQn(TCNQ)$_2$ may result from the overlap of two intra-tetramer charge transfer excitations (at $\approx$1000 and 2200 cm^{-1}), as well as a low energy inter-tetramer charge transfer excitation (also at $\approx$2200 cm^{-1}). As discussed in Chapter 2, the low energy charge transfer excitation at 2200 cm^{-1} is of proper energy and significant intensity to couple with the TCNQ phonon modes.[166]

The temperature dependence of the charge transfer bands indicates important changes in the electronic structure of the salt as a result of the phase transition. Below T_c, the low energy charge transfer band can be resolved into two main bands, centered at 1000 and 2500 cm^{-1}, respectively. They are separated by a minimum in the frequency dependent conductivity at 1500 cm^{-1}. Šwietlik and Graja have observed a similar two banded structure in both phases of tetrameric MTPP(TCNQ)$_2$.[170]

As in the high- temperature phase, we expect two intra-tetramer and one inter-tetramer charge transfer bands. Although the intra-tetramer distances are identical at 100 K, the mode of overlap is different.[88] Consequently, two distinct intra-tetramer charge transfer excitations are still expected. We have assigned the band at $\approx$1000

cm^{-1} to intra-tetramer charge transfer; the band at 2500 is probably composed of overlapping intra- and inter- tetramer excitations.

Below T_c, the increased oscillator strength of these bands is indicative of a larger intra-tetramer transfer integral, consistent with structural studies in the low-temperature phase[7] which conclude that intra-tetramer distances decrease as the chains become more uniformly tetramerized. From the systematic increase in the oscillator strength of the low energy charge transfer band below T_c, we can infer a gradual change in the transfer integral, and thus, a change in the intra-tetramer distances. The band sharpening below T_c is a characteristic commonly associated with charge localization.

The band at ≈ 10000 cm^{-1}, often seen as a weak doublet, is attributed[19,163,79] to the charge transfer process: $TCNQ^- + TCNQ^- \rightarrow TCNQ^0 + TCNQ^{2-}$. The oscillator strength of this band is probably small because an electron has to hop two sites in order to occupy the same site with another electron in this material. Because two electrons reside on the same site in the final state, the energy of this transition is proportional to $(U - V)$, the Hubbard parameters for on-site and nearest neighbor Coulomb repulsion, respectively.[38] Assuming V is small, we can estimate the on-site Coulomb repulsion from the center position of this band. We find $U = 9700$ cm^{-1} (or 1.2 eV) for both phases of NPrQn(TCNQ)$_2$, which is comparable to the on-site Coulomb repulsion energy in other TCNQ charge transfer salts.[18,4] The higher energy charge transfer excitation is not strongly temperature dependent.

Electron-Phonon Coupling

Upon comparison of the infrared electron-molecular vibration coupling induced modes with other semiconducting quarter filled 1:2 salts. it becomes clear that the intra-tetramer charge transfer bands strongly interact with the A_g molecular vibrations of the TCNQ molecule.[166-3] All ten A_g modes are observed in NPrQn(TCNQ)$_2$.

most with relatively strong intensity. The intensities and frequencies of the excitations are in relatively close agreement to the previously studied 1:2 semiconducting compounds listed above,[166-169] implying that the electron-phonon coupling constants are of similar size in these different salts.[82]

The infrared spectra of semiconducting TCNQ salts are dominated by electron localization effects,[19-18] suggesting that the TCNQ stack can be modeled as linear clusters of dimers or tetramers. The solution of the electron-phonon interaction for an isolated TCNQ dimer with one electron per two TCNQ molecules has been presented by Rice et al,[166] the final result of which is an expression for the frequency dependent conductivity. Successful application of the Rice dimer model to the experimental frequency dependent conductivity in the chain axis direction indicates that dimerized quarter filled salts may be understood as one electron on an isolated dimer.

However, application of the isolated dimer model to our frequency dependent conductivity data for $NPrQn(TCNQ)_2$ is unsatisfactory, with especially poor agreement below 1000 cm^{-1}. The best fit is shown in the lower panel of Fig. 30. The model parameters for are as follows.[7,171] Electronic parameters are $t = 1500$ cm^{-1}, $\omega_{CT} = 2050$, and $\gamma = 2000$ cm^{-1}. Unperturbed phonon frequencies were obtained from a plot of $\mathrm{Re}\left(\frac{1}{\sigma(\omega)}\right)$, while the coupling constants were obtained from Painelli et al.[82] Structural data was obtained from Ref. 87. The poor quality of the fit in the upper panel of Fig. 30 suggests that $NPrQn(TCNQ)_2$ should not be considered as an isolated dimer in a $4k_f$ configuration with one electron on two sites, and that the inter-dimer interactions are too strong to neglect. This result was not unexpected; although $NPrQn(TCNQ)_2$ has a quarter filled band, the TCNQ chain is composed of relatively isolated *tetramers*.

These concepts on electron-molecular vibrational coupling have been extended by Yartsev[23,3] to describe isolated tetramers. The result of such a calculation, obtained

using this model, is shown in the lower panel of Fig. 30. The extended Hubbard parameters are as follows: $t = 1000$ cm^{-1}, $t' = 0.8t$, $U = 6t$, $V = 0.4U$, and $\Delta = 0.25t$.[7,171] Electronic parameters are $t = 1000$ cm^{-1}, $\gamma = 1800$ cm^{-1}, and charge transfer excitations centered at 2200, 9000, 13000, and 19000 cm^{-1}, respectively. Unperturbed frequencies and coupling constants were obtained as described above. The intra-tetramer distances and unit cell volume were obtained from structural studies at room temperature.[87] The good agreement with our experimental spectrum suggests that NPrQn(TCNQ)$_2$ is a system of relatively isolated TCNQ tetramers, occupied by two electrons, and that intra-tetramer interactions dominate the optical properties of the salt.

The A_g vibrational lines split into doublets below T_c. As seen in Fig. 29, the oscillator strength is unevenly divided between the two peaks of the doublet; in every case, the lower energy resonance is much more intense. Within the doublet, the higher energy sideband monotonically grows in intensity as temperature decreases, but its resonance frequency remains constant. The resonance frequency of the more intense main mode gradually increases as temperature decreases; thus, the energy difference between the main peak and the sideband decreases with decreasing temperature below T_c. This splitting behavior is qualitatively seen in all of the doublet modes.

Such phonon splitting behavior has been previously observed in the low-temperature phases of other organic charge transfer salts, and is generally attributed to an unevenly localized charge distribution within the tetramer repeat unit.[23,170,169,3,47] The unperturbed A_g phonon frequencies and splitting energies, shown in Table 3, support this claim. Comparison of these values with the frequency difference expected from isolated TCNQ^0 and TCNQ$^-$ molecules[164,165] shows that the doublet frequency separation is of reasonable size. Consequently, the fine struc-

ture in NPrQn(TCNQ)$_2$ presents evidence for two distinct molecular environments of different charge within the tetramer.

The possibility that the splitting of the vibrational lines is a consequence of the coupling of the A_g vibrational modes with *two* low energy charge transfer excitations should not be ignored. Examination of Fig. 27 will show that although there is a weak band centered at 1000 cm^{-1} in the low-temperature phase, it is well separated in frequency from the main charge transfer band at 2500 cm^{-1}, and thus, is unlikely to couple to the phonon motion. If it were involved in the coupling, we would expect to see A_g multiplets, not doublets. Alternately, the A_g phonon splitting may be due to steric interactions of the donor cations with the TCNQ stack. However, this is also unlikely, as structural studies[87,88] reported no significant changes in the behavior of the NPrQn cation as a function of temperature.

Thus, we believe that the doublet splitting pattern below T_c is directly related to the modification of the original charge distribution by localization within the tetramer, probably on every other site. (The absence of A_g mode splitting in the infrared spectra of the high-temperature phase could also be taken as evidence for site indistinguishability.)

Implications for Charge Transport

The spectra of NPrQn(TCNQ)$_2$ are clearly characteristic of a semiconductor in the high-temperature phase, but it is not a straightforward matter to assign an optical gap, as it appears to be broadened and obscured. We believe that the broadening is the result of the overlap of three distinct charge transfer bands, representing the two different intra-tetramer and one inter-tetramer charge transfer excitation, respectively.

Because conduction is limited by inter-tetramer hopping, an optical estimate for the semiconducting energy gap can be obtained by linear extrapolation from the

shoulder of the band associated with inter-tetramer transport in Fig. 27. It can also be obtained from the sum rule.[7] Using this method, we obtained $2\Delta \approx 800 \pm 200$ cm^{-1} at 300 K. Alternately, the gap position can be estimated from the changes in the phonon line shape: below the gap, phonons have a typical Lorentzian shape; above the gap, overlap with the electronic feature perturbs the excitation, resulting in a Fano[46] line shape. Using this method, we obtain a comparable estimate of the semiconducting gap.

In the low-temperature phase, we can distinguish the various band shapes more clearly. Extrapolation of the leading edge of the charge transfer band associated with inter-tetramer hopping provides us with an estimate of the semiconducting energy gap at 100 K; we find $2\Delta \approx 1800$ cm^{-1} at 100 K, consistent with transport measurements at that temperature.[13,14]

Recent calculations by Homes et al.[52] predict a larger gap in both the high- and low-temperature phases. The authors also find that above T_c, the gap is 58% Peierls and 42% external cation potential, whereas below T_c, it is almost wholly due to the Peierls (intrinsic chain) distortion. It is suggested that a gradually increasing Peierls contribution combined with a decreasing external cation potential may explain the sharp drop of the dc conductivity. These calculations bolster a suggestion made several years ago by Janossy et al.[14] as to the origin of the weakly metallic properties in the high-temperature phase. They proposed that a large cation potential in the high-temperature phase may cause the reversal of the valence and conduction band energy levels, thus leading to a finite density of states at the Fermi level.

Comparison with Previous Results

In this section, we discuss our spectral studies of NPrQn(TCNQ)$_2$ with respect to the previous results on the closely related quarter-filled compounds Qn(TCNQ)$_2$ and (NMP)$_x$(Phen)$_{1-x}$(TCNQ).[26,172-176] Although the previous measurements by

McCall et al. were performed on KCl pellets due to small crystal size, many useful comparisons can be made.

Despite the chemical modifications of the donor cation and the significantly different dc conductivities, the 300 K spectra of $NPrQn(TCNQ)_2$, $Qn(TCNQ)_2$ and $(NMP)_x(Phen)_{1-x}(TCNQ)$ are similar in character and typical of semiconducting charge transfer salts. In the infrared, all three of the aforementioned materials have infrared active A_g vibrational features, although they are less pronounced in $Qn(TCNQ)_2$ and $(NMP)_x(Phen)_{1-x}(TCNQ)$ due to screening by conduction electrons. Excitations at higher energy can be assigned to charge transfer in the TCNQ chain in these large U materials. McCall et al.[26] estimate $2\Delta \approx 700\text{-}950$ cm^{-1} for $Qn(TCNQ)_2$, in excellent agreement with our estimate for the NPrQn salt at 300 K. The authors attribute the gap in both $Qn(TCNQ)_2$ and $(NMP)_x(Phen)_{1-x}(TCNQ)$ to a combination of a Peierls distortion and the external cation potential. It is expected that the semiconducting gap in $NPrQn(TCNQ)_2$ is of similar origin.

There are many similarities in the low-temperature spectra of these materials as well. As in $NPrQn(TCNQ)_2$, the A_g vibrational features of $Qn(TCNQ)_2$ and $(NMP)_x(Phen)_{1-x}(TCNQ)$ become more pronounced at lower temperature. From plots of the normalized A_g model oscillator strength vs. temperature, the authors conclude that the strength of the Peierls interaction, and thus the size of the transport gap, increases with decreasing temperature. Qualitatively similar behavior is found in $NPrQn(TCNQ)_2$ as well. For $Qn(TCNQ)_2$ and $(NMP)_x(Phen)_{1-x}(TCNQ)$, the gradual decay of the gap with temperature has been ascribed to the presence of thermal and chemical solitons.[174,175] The role of soliton defect states in $NPrQn(TCNQ)_2$ is still under investigation.

Although the chemical structure of these materials are very closely related, the temperature dependence of the electron-phonon coupling is strikingly different in-

dicating important changes in the fundamental interactions in these materials. As previously mentioned, the vibrational features in these salts become more intense with decreasing temperature. However, NPrQn(TCNQ)$_2$ has less (rather than more) residual conductivity below the gap than the other two quinoid based charge transfer salts at lower temperature. This is probably related to the lower DC conductivity. The A_g vibrational modes in NPrQn(TCNQ)$_2$ also provide evidence for a structural phase transition. At T_c (220 K), the A_g phonon modes of NPrQn(TCNQ)$_2$ split into doublets, evidence for a change in the charge distribution within the tetramer. No such dramatic changes are observed in the electron-phonon coupling in Qn(TCNQ)$_2$ or (NMP)$_x$(Phen)$_{1-x}$(TCNQ) as a function of temperature.

The very low frequency absorption of Qn(TCNQ)$_2$ and (NMP)$_x$(Phen)$_{1-x}$-(TCNQ) is small, and based upon this observation, the authors conclude that a gap exists in the density of states at the Fermi level. This is contrasted by an unusual increase in the low energy frequency dependent conductivity in NPrQn(TCNQ)$_2$, which may indicate the importance of disorder near the Fermi surface.[177] Such disorder would strongly affect the infrared and physical properties of this material.

The temperature dependent DC conductivity of Qn(TCNQ)$_2$ and (NMP)$_x$-(Phen)$_{1-x}$(TCNQ) has been fit to a two-component model by Epstein and Conwell in which σ_T is a product of a strongly temperature dependent mobility and an activated carrier concentration.[178,179] The expression is given as:

$$\sigma_T = ne\mu = \sigma_0 T^{-\alpha} \exp\left(\frac{-\Delta}{T}\right). \tag{64}$$

Although such a model for the temperature dependence of the DC conductivity would seem to provide a plausible framework for the observed metal-like transport properties and semiconductor-like spectra which characterized NPrQn(TCNQ)$_2$, a fit of this model to the experimental data[13] is, overall, unsatisfactory. In the high-temperature

phase, we obtain a relatively good quality fit, with parameters $\Delta \approx 1190$ K and $\alpha = 4.0$. However, near and below T_c, the model conductivity does not fall fast enough to give a reasonable fit to the data. Perhaps a better fit to the $NPrQn(TCNQ)_2$ data would be obtained using a temperature dependent activation energy, Δ. Homes et al. have suggested that this sharp falloff may be due to the opening of a transport gap combined with the simultaneous increase of the Peierls contribution to the gap.[52]

The Phase Transition

The behavior of the A_g phonon modes is a strong function of temperature in $NPrQn(TCNQ)_2$. Experimentally, the doublet structure of the A_g phonon modes appears in the spectra only below 220 K and is clearly a characteristic feature of the electronic structure below T_c.

Changes in these A_g modes are directly related to fundamental characteristics of the phase transition. In similar studies of TCNQ salts, Bozio and Pecile have shown that the intensity of the satellite band is proportional to the square of the order parameter.[180,181] In our case, it seems reasonable to define the charge difference between the two inequivalently charged TCNQ ions in the tetramer as the order parameter of the structural phase transition. This is analogous to defining the order parameter as the change in the static charge density wave amplitude, observed in charge density wave materials such as TTF-TCNQ.[24]

A more detailed examination of the typical phonon doublet structure of $NPrQn(TCNQ)_2$ below T_c is given in this section. As shown in Fig. 29, each A_g peak splits into a main phonon mode and a less intense, higher energy satellite mode in the low-temperature phase. The integrated spectral intensity of the satellite mode grows systematically with decreasing temperature below T_c. The oscillator strengths of four modes vs. temperature are shown in Fig. 31. In this plot, the oscillator strengths have been normalized with respect to the limiting low-temperature value of

the intensity of each mode. The error in the oscillator strength at each temperature is estimated to be ±4%.

We can conclude from the gradual variation of the integrated spectral intensity of the satellite mode with temperature that the order parameter of the phase transition also changes gradually with temperature. Thus, the structural phase transition is of second order, in agreement with previous work.[13,14] Additional evidence for this conclusion is found in the very systematic change of the entire infrared reflectance spectrum through the phase transition, with no hysteresis observed on temperature cycling.

Results: DMTM(TCNQ)$_2$

(010) Crystal Face: Room Temperature Spectra

Figure 32 displays the room temperature reflectance on the (010) face over the entire spectral range for polarizations parallel and perpendicular to the direction of maximum reflectance (R_{max}). Assuming that two principal axes are located in this plane, the R_{max} (and thus, the perpendicular to R_{max}) direction must be those principal axes of the crystal. No clear evidence of a change in the R_{max} direction with wavelength was found (except for the trivial exchange by 90° between 6000 and 18000 cm^{-1}), although the crystal symmetry allows for such dispersion.

For the electric field vector polarized along R_{max}, the frequency dependent conductivity spectrum displays two electronic excitations (centered at $\approx$ 3200 cm^{-1} and $\approx$ 10500 cm^{-1}); the mid-infrared band contains a majority of the oscillator strength. In other strongly dimerized TCNQ salts these absorptions have been attributed to the transfer of charge between TCNQ molecules in the stack.[22,163,79] At low frequency, the spectra display many sharp vibrational features. Ten of these modes are A_g vibrations of the TCNQ molecule, activated by coupling to the charge transfer

excitations.[22,24] The presence of these well known features[164,165] in this polarization indicates that R_{max} is in the direction of maximum charge transfer, and thus, closely aligned with the c crystallographic axis. Additional vibrational structure is due to TCNQ modes of other symmetry[19] as well as those of the N-dimethyl morpholinium donor cation. In addition, a strong two-phonon absorption mode is observed at 2675 cm^{-1}.

The reflectivity perpendicular to the maximum reflectance on the (010) face is low ($\approx 10\%$), flat and almost featureless (Fig. 32). In this polarization, no temperature dependence was observed in the infrared. At higher energies, there is a small absorption at ≈ 10000 cm^{-1}, and a strong feature centered at ≈ 18000 cm^{-1}. The absorption at ≈ 18000 cm^{-1} is probably attributable to a localized excitation of the TCNQ molecule.[18,79]

Although the direction perpendicular to R_{max} on the (010) face is most likely a principal axis of the crystal, this particular polarization is relatively uninteresting. It lacks temperature dependence and electron-phonon coupling in the infrared and provides no information on the structural phase transition. Consequently, for the majority of this section, we will confine our discussions to the data in the R_{max} direction on the (010) crystal face.

The extreme anisotropy observed between the two polarizations in DMTM(TCNQ)$_2$ on this face of the crystal has been observed for many other TCNQ charge-transfer salts as well,[4,18,19,20] once again clearly emphasizing the spectroscopic uniqueness of the TCNQ stacking direction. Additionally, absence of charge transfer and electron-phonon coupling features in the perpendicular polarization provides proof that the polarizers were correctly positioned.[4,18]

(010) Face: Temperature Dependence

To compare the spectral differences between the high- and low-temperature phases in the R_{max} direction on the (010) crystal face, the reflectivity and the frequency dependent conductivity are shown in Fig. 33 for two temperatures, 300 K and 150 K. The detailed temperature dependence of the mid-infrared charge transfer band is displayed in Fig. 34.

Important changes in the electronic state occur as a result of the phase transition in the R_{max} direction. Figure 34 illustrates the strong temperature dependence of the mid-infrared excitation centered at 3200 cm^{-1}. The oscillator strength of this band increases systematically with decreasing temperature within each phase—a trend which is especially pronounced in the low-temperature phase. As shown in Fig. 33, the position of the sharp plasma edge and deep minimum in the reflectivity is red shifted in the low-temperature phase.

A second charge transfer band occurs at ≈ 10500 cm^{-1} for both 300 and 150 K. (Fig. 33) The general shape and oscillator strength of this band is strongly affected by the structural phase transition. In the high-temperature phase, the oscillator strength of this absorption is relatively small, but below T_c, this high energy excitation appears as a strong doublet. The difference between the two phases is striking, and is an effect not seen in other quarter-filled TCNQ salts.

The infrared reflectance spectra exhibit few changes around T_c (272 K) as a function of temperature. The overall character of the electron-phonon coupling is relatively unaffected by the phase transition. In the low-temperature phase, the A_g phonon modes do not show the pronounced fine structure that was observed in NPrQn(TCNQ)$_2$ and others, which would be indicative of a separation of charge.[8,84] However, careful examination of the A_g phonon modes in the low-temperature phase reveals very slight multiplet splitting at the crest of some of these modes. Such

splitting is probably a result of the reduced molecular site symmetry below the phase-transition temperature.

Extrapolating the frequency dependent conductivity to zero frequency, we obtain an estimate of the DC conductivity of $\approx 1\ \Omega^{-1}\ cm^{-1}$ at 300 K. This value is in reasonable agreement with that obtained by four-probe measurements.[15,16]

(110) Crystal Face

On the (110) face of the single crystal samples of $DMTM(TCNQ)_2$, R_{max} is polarized purely along the c crystallographic axis. Consequently, the IR and visible spectra are very similar (in terms of the electron-phonon coupling and infrared excitations) to that in the R_{max} on the (010) crystal face. The temperature dependence is also analogous to what was observed on the (010) face. However, from examination of Fig. 35, it is evident that the phonon lines along c on the (110) face are not as intense or as well shaped as those measured along the R_{max} direction on the (010) face, suggesting that the direction of maximum charge transport is not directly along the c axis. From the ratio of phonon peak heights, we estimate that the angle between R_{max} on the (010) crystal face and R_{max} (the c crystallographic axis) on the (110) side to be ≈ 20 degrees. This is in good agreement with that expected from the crystal structure.[86,89,90] Consequently, we conclude that the TCNQ stacking direction, c, is not a principal axis of the dielectric tensor. Thus, for the remainder of the paper and especially in our discussion of the electron-phonon coupling effects, we concentrate on the spectra along R_{max} on the (010) crystal face, which we believe is a principal axis of the crystal.

Perpendicular to the R_{max} direction on the (110) face of the crystal, we measure a combination of two principal axis reflectivities, shown in Fig. 35. The major component of this polarization is b, the axis directed along the length of the TCNQ

molecule. As in the spectra taken of the (010) crystal face, there is extreme anisotropy between the two polarizations.

In the infrared, the reflectivity is low and flat, with a few weak phonons and no temperature dependence. In the low-temperature phase, we found no evidence of a low energy excitation at 430 cm^{-1}, attributable to a reduced band gap, as expected from the crystal field distortion theory of the phase transition. The frequency dependent conductivity, shown in Fig. 36, is close to zero below about 4000 cm^{-1}. $\sigma_1(\omega)$ is actually slightly negative in the far-infrared, probably due to small errors in measuring the reflectivity. We consider $\sigma(\omega)$ to be effectively zero in this regime. The frequency dependent conductivity begins to rise at $\approx$ 4000 cm^{-1} in both phases. In the near-infrared and visible frequency range, there is strong temperature dependence, especially around 10000 cm^{-1}. Among the more interesting electronic features is the strong absorption at $\approx$ 2 eV in both phases, which is often associated with intramolecular excitations within a doubly charged dimer.[182] Finally, the strong excitation centered at $\approx$ 23000 cm^{-1}, seen in the reflectance spectrum of Fig. 35 may be due to a localized excitation polarized along the long axis of the TCNQ molecule.[163,79]

Discussion: DMTM(TCNQ)$_2$, (010) Crystal Face

Electronic Features along R$_{max}$

Above T_c, the spectra of DMTM(TCNQ)$_2$ along the R$_{max}$ direction on the large (010) crystal face shows qualitative agreement with other quarter-filled, 1:2 semiconducting charge-transfer materials in terms of the position and intensity of the electronic and vibrational features.[4,18,19,20,22] The similarity between our data at 300 K and that of Rice et al.[22] for the MEM(TCNQ)$_2$ system at room temperature (the dimerized phase) is particularly striking, and will be discussed at various points in this section.

For strongly dimerized, large U materials, the high energy spectral features polarized closely along TCNQ stacking direction typically consist of the two aforementioned strong, broad absorptions which correspond to electronic charge transfer between TCNQ moieties within the chain.[163,79] Despite differences is the chemical natures of the donor cation in MEM(TCNQ)$_2$ and DMTM(TCNQ)$_2$, the low energy electronic excitations of the TCNQ chain are nearly identical, centered at $\approx$ 3200 cm^{-1}.

In DMTM(TCNQ)$_2$, the center frequency and integrated oscillator strength of the mid-infrared band is a strong function of temperature, increasing systematically with decreasing temperature within each phase. This trend is especially pronounced in the low-temperature phase, and correlates inversely with the DC conductivity. For example, at 250 K, σ_{dc} is a maximum, but the oscillator strength of the mid-infrared band is a minimum. However, we find no evidence that this "missing oscillator strength" at 250 K has shifted to lower frequency, as might be expected for increased conductivity. (See the later discussion of the sum rule.) At the present time, we have no explanation for this phenomenon.

The temperature dependence of these electronic features have important implications for charge transport in the TCNQ stacking direction. Yartsev and Graja[48,49] have proposed that electron hopping between molecular clusters may responsible for the activated nature of the DC conductivity in dimerized salts. Based upon this model and the average value of the static charge transfer,[71] we calculate E_A=0.30 eV in the high-temperature phase, in reasonable agreement with that reported from transport measurements.[15,16] Consequently, we may conclude that the mechanism of charge transport above T_c is dominated by hopping between isolated dimers. However, in the low-temperature phase, we find poor agreement between the activation energy transport as calculated by this method and the experimental value of 0.03 eV.

Thus, we must conclude that charge transport is not dominated by hopping along the TCNQ chain below T_c; it must occur by an entirely different mechanism.

As shown in Fig. 33, the position of the deep plasma minimum in the reflectivity is red shifted in the low-temperature phase. Red shifts of these features are rather unusual.[4,20] The classical screened plasma frequency is defined as

$$\tilde{\omega}_p^2 = \frac{4\pi n e^2}{\epsilon_\infty m^*};$$ (65)

thus, the observed spectral modifications may result from (1) a decrease in the band curvature (increase in m^*), (2) a reduction in the number of conduction electrons at T_c, or (3) an increase in ϵ_∞ due to the increased strength of the U band. From the partial sum rule, we estimate the effective band mass to be $m^* = 1.5 m_e$ and $m^* = 1.8 m_e$ in the high- and low-temperature phases, respectively, supporting the band curvature proposal. For additional details, refer to the later discussion of the sum rule.

A second higher energy charge transfer band is observed in our spectra at ≈ 10500 cm^{-1}. As previously discussed, from the center position of this band, we obtain an estimate for the effective on-site Hubbard parameter (U) of 10500 cm^{-1} (1.30 eV) for both phases of DMTM(TCNQ)$_2$, which is comparable to values obtained for other TCNQ charge transfer salts.[18,19] In DMTM(TCNQ)$_2$, the shape and oscillator strength of the higher energy excitation display strong temperature dependence. The excitation at 10500 cm^{-1} is weak in the high-temperature phase. However, in the low-temperature phase, this band appears as a strong doublet. The fundamental nature of such a doublet structure is not well understood.[4,18,19,20]

The weak absorption of the U band in the high-temperature phase suggests that few electrons occupy adjacent sites along the chain, possibly resulting in the low dc conductivity. In contrast, the increased oscillator strength of the U band below

T_c suggests that the charged electrons are occupying adjacent sites more frequently. That the electrons are much closer together in the low-temperature phase without a significant change in the magnitude of the on-site Coulomb repulsion suggests that the effect of the long-range Coulomb interaction may be decreased. Such a charge reorganization may be responsible for the increased conductivity.

Electron-Phonon Coupling Along R_{max}

Among the most prominent and interesting spectral features of TCNQ charge-transfer salts are the ten in-plane A_g vibrational modes of the TCNQ molecule, activated by coupling to the charge-transfer excitations.[19,20,22,25,164,165] All ten A_g modes are observed in DMTM(TCNQ)$_2$, most with relatively strong intensity. In the high-temperature phase, the vibrational structure is very similar to that in the MEM(TCNQ)$_2$ system.

The overall character of the electron-phonon coupling in DMTM(TCNQ)$_2$ is relatively unaffected by the structural phase transition at 272 K. Below T_c, the A_g phonon modes in DMTM(TCNQ)$_2$ exhibit no pronounced fine structure, as might be expected in light of the evidence of several independent investigations[15,16,93] which imply two inequivalent TCNQ chains per unit cell—one with and one without a $2k_F$ distortion. The only spectral evidence to support the hypothesis of a unit cell doubling is the very slight multiplet splitting at the crest of some of the A_g modes. This splitting is probably a result of the reduced symmetry below the phase transition temperature, and therefore related to the inequivalence of the TCNQ stacks.

The infrared spectra of typical insulating 1:2 compounds are dominated by electron localization effects[4,18,19,20], suggesting that the TCNQ stack may be well described by linear cluster models of dimers, trimers or tetramers. Based upon structural evidence[89,90] and the similarity of our spectra with that of MEM(TCNQ)$_2$,

we have analyzed our infrared results within the framework of this isolated dimer model[22].

The solution of the coupled electron-phonon problem for an isolated TCNQ dimer with one electron per two TCNQ molecules has been given by Rice et al.,[22] and is detailed in Chapter 2. This model has been fit to the experimental optical conductivity of DMTM(TCNQ)$_2$ at room temperature; the results are shown in Fig. 37. The electronic parameters are $t = 1957$ cm^{-1}, $\omega_{CT} = 3165$ cm^{-1} and $\gamma = 2203$ cm^{-1}. The structural parameters used in the calculation were obtained from the 300 K structural studies.[86] The experimental values for the unperturbed phonon frequencies and the EMV coupling constants for DMTM(TCNQ)$_2$ at room temperature are shown in Table 4, along with the calculated A_g modes of the TCNQ$^-$ molecule by Bozio et al.[183] and the values for the EMV coupling constants based on a priori calculations by Lipari et al.[83], as well as the dimer model results for MEM(TCNQ)$_2$ at 300 K by Rice et al.[22] A plot of Re$(1/\sigma_1(\omega))$ gives similar frequencies and coupling constants.[28] Neither the frequencies nor the coupling constants of DMTM(TCNQ)$_2$ were observed to be a function of temperature within experimental error. Temperature dependence of the frequencies of the EMV coupling constants is not observed in the MEM(TCNQ)$_2$ system either.[22,27]

The values of the unperturbed phonon frequencies of DMTM(TCNQ)$_2$ (Table 4) are in good agreement with those determined for MEM(TCNQ)$_2$ and also with the calculated frequencies for a TCNQ$^-$ molecule. The coincidence is slightly better for the lower energy modes, a trend which we do not understand at the present time. The EMV coupling constants agree well with tabulated values for other TCNQ salts, calculated using the dimer model.[82] However, the dimer model calculations for the EMV coupling constants are smaller than those predicted by the a priori calculations,

an effect which has also been observed in some of the TMTSF charge transfer salts[184] as well.

While the dimer model fit in Fig. 37 approximates the experimental data fairly well, it fails in a number of important aspects. One of the difficulties in fitting the dimer model to the optical conductivity stems from the fact that the phonon conductivities can never exceed that of the central charge transfer band, regardless of how large the EMV coupling constant becomes. Thus, the intensity of some of the A_g modes cannot be reproduced. Furthermore, the transfer integral and the position of the charge transfer band cannot be determined self consistently. The spectrum of excitations in a dimer requires that $\omega_{CT} \geq 2t$. However, $t = 1957$ cm^{-1}, which requires that $\omega_{CT} \geq 3900$ cm^{-1}, higher than observed. This implies that a significant portion of the conductivity may arise from interband transitions rather than from charge transfer excitations. This result is not too surprising given the the fact that this system is only weakly dimerized and not as localized (based on the larger value of the 300 K dc conductivity) as MEM(TCNQ)$_2$. The two-dimensional nature of the sulfur atom in the counter-ion may also play a role.

To obtain an improved description of the electron-phonon coupling in DMTM(TCNQ)$_2$, the experimental data was fit to a two-fold degenerate charge density wave model by Bozio et al.[25] The results of the model fit to the frequency dependent conductivity at 300 and 150 K are discussed in detail elsewhere.[8] The improved fit of Bozio's phase phonon model to the experimental data suggests that the electron-phonon coupling in DMTM(TCNQ)$_2$ is better described as an interaction between the A_g vibrational modes and a charge density wave (rather than with a localized charge transfer excitation). Thus, we conclude that DMTM(TCNQ)$_2$ is a less localized material than the well-studied MEM(TCNQ)$_2$.

Sum Rule

Information about the effective number of electrons involved in optical transitions can be obtained from the partial sum rule[161,162]

$$\left(\frac{m}{m^*}\right)N_{eff}(\omega) = \frac{m}{32\pi N_c e^2}\int_0^\omega \sigma_1(\omega')d\omega', \tag{66}$$

where m^* is the effective mass of the carriers and N_c is the number of conduction electrons per unit volume. A plot of this function is shown in Fig. 38 for the electric field vector polarized along R_{max} (close to the chain direction on the large crystal face) at 300 K and 150 K, as well as perpendicular to the R_{max} direction on the same face at 300 K.

In the direction close to the dimer axis, $(m/m^*)N_{eff}$ rises rapidly in the low frequency region, leveling off above 5000 cm^{-1}. From the plateau values of the integrated oscillator strength in the near-infrared, we estimate $m^* = 1.5m_e$ and $m^* = 1.8m_e$ in the high- and low-temperature phases, respectively, assuming $N_{eff} = 0.5$. The integrated oscillator strength of the vibrational features does not vary significantly with temperature. At higher energy, the increased oscillator strength due to the mid infrared charge transfer band is readily evident. In DMTM(TCNQ)$_2$, the integrated oscillator strength of this band is a strong function of temperature, increasing systematically with decreasing temperature within each phase. (Figure 34) However, as illustrated in Fig. 38, we find no evidence that this missing oscillator strength at 250 K has shifted to lower frequency, as might be expected for increased conductivity. In fact, it has shifted to higher energies. The enhanced contribution of the 10500 cm^{-1} charge transfer band is seen in the $T = 150$ K data. The two curves come together nicely at higher frequency, demonstrating conservation of oscillator strength above and below T_c. In the direction perpendicular to the chain axis, $(m/m^*)N_{eff}$ is small in the infrared but rises rapidly at higher frequencies.

Discussion: (110) Crystal Face

It has been postulated that the dramatic increase in the DC conductivity in DMTM(TCNQ)$_2$ is a result of a crystal-field distortion at T_c.[86] Figure 14 shows the band structure in the high- and low-temperature phases of the salt as proposed by Visser et al.[86] An identical set of bands is located higher energy, separated from those shown in Fig. 14 by the Hubbard gap. Spectral transitions occur between the various energy levels.

Based upon the band structure in Fig. 14, we expect the electronic spectrum to be quite simple in the high-temperature phase, having only one main excitation within the manifold at low energy. Because the activation energy for conduction has been measured to be 0.26 eV,[15,16] we can approximate the resultant band gap to be 0.52 eV or 4200 cm^{-1}. We would also expect to see several higher energy features, including an excitation across the Hubbard gap near ≈ 1.3 eV (or 10500 cm^{-1}) and a transition to the upper level of the manifold at ≈ 1.82 eV (or 14700 cm^{-1}), the energy difference between these two features being the 0.52 eV band gap. Transitions originating from excited states will not be observed in the spectra.

In the low-temperature phase, reduction of symmetry splits the bands, and several more transitions become possible. According to the crystal field distortion theory, four unique transitions should be observed within the manifold at ≈ 430 cm^{-1}, ≈ 3700 cm^{-1}, ≈ 4200 cm^{-1} and ≈ 7900 cm^{-1}. We are primarily interested in the lowest energy charge transfer processs, as they are expected to dominate the conduction process. At higher energy, we expect to observe excitations across the Hubbard gap to various levels in the upper manifold. The three lowest energy features would be at ≈ 10500 cm^{-1}, ≈ 14200 cm^{-1} and ≈ 14600 cm^{-1}, the energy difference between the last two being essentially the 0.06 eV low-temperature valence to conduction band gap.

Figure 36 shows the experimental frequency dependent conductivity perpendicular to R_{max} on the (110) crystal face in the high- and low-temperature phases. It remains for us to assess our spectral data in this polarization in terms of the proposed crystal field distortion along the b axis and the associated band structure modifications shown in Fig. 14.

As expected, we observe no electronic features in the 300 K spectrum at low energy. However, we also find no evidence of a low energy charge transfer band at 430 cm^{-1} in the low-temperature phase of the salt, which would have been expected from the crystal field splitting. It is anticipated that such an excitation would be strong if interchain charge transfer dominated the conduction process in the low-temperature phase.

In light of the various recent studies[15,16,93] which give great credibility to the crystal field distortion theory by Visser et al.,[86] it is not clear why we do not observe conclusive spectral evidence for the low energy charge transfer at 430 cm^{-1}. One possible explanation is that the physical separation of the TCNQ chains is large due to the DMTM cation sheets, and that the oscillator strength of this transition is small. Another possibility is that some of the lower energy electronic transitions are either symmetry forbidden or of the wrong symmetry to be observable with electric dipole allowed spectroscopy.[185,186] If the transition were symmetry forbidden, it would not contribute significantly to the conduction process. However, if an excitation does not obey the IR selection rules, it could still contribute to the conduction process. This may explain why low energy charge transfer is not evident in our spectra below T_c. Low-temperature Raman measurements on DMTM(TCNQ)$_2$ would augment this study nicely.

In both phases, there is an absorption edge at $\approx$ 4000 cm^{-1}, above which the frequency dependent conductivity begins to rise rapidly. It is this energy which we

attribute to the interchain transport gap, corresponding to an activation energy of ≈ 0.25 eV. This value is in excellent agreement with transport measurements[15,16] and the band structure predictions of Fig. 14 for the high-temperature phase. However, in the low-temperature phase, according to the band structure diagram, we should also expect to see evidence for two low energy charge transfer bands (at ≈ 430 and ≈ 3800 cm^{-1}). From examination of Fig. 36, it is clear that these are also absent.

In the near infrared and visible frequency range, there is strong temperature dependence in the spectra, especially near 10000 cm^{-1}. In the high-temperature phase, this feature is a doublet, the splitting between peak centers of the doublet being ≈ 1900 cm^{-1}. Below T_c, the spectra in this region has a triplet structure, the center absorption being most pronounced. Although the main absorption in this frequency region could result from a transition across the Hubbard gap to the lowest energy band in the second manifold. The doublet and triplet features are not accounted for within the crystal field splitting theory.

Among the most interesting of the higher energy features is the strong absorption at ≈ 2 eV. As it is not present in the other two principal axis polarizations which we have discussed, we conclude that it is polarized exclusively in the b crystallographic direction. Although such a strong feature in this frequency regime is often associated with an intramolecular excitation within a doubly charged dimer[182], we instead believe it is associated with a strongly allowed transition across the Hubbard gap to the upper level of the second manifold. Based upon the crystal field splitting theory and the associated band structure modifications (Fig. 14), such a transition is expected to appear at ≈ 1.8 eV. Below T_c, a broader band with a slight doublet character might be anticipated due to the reduced symmetry. However, no such temperature dependence is observed in Fig. 36.

Table 3. A_g phonon mode splitting at 100 K for $NPrQn(TCNQ)_2$

A_g Mode	ν_a (cm^{-1})	$\Delta\nu_{obs}$ (cm^{-1})	ν_a (TCNQ^0) (cm^{-1})	ν_a (TCNQ)$^-$ (cm^{-1})
ν_2	2188.8	18.5	2229	2206
ν_3	1570.5	26.1	1602	1615
ν_4	1349.0	63.5	1454	1391
ν_5	1164.9	21.5	1207	1196
ν_6	958.6	17.2	948	978
ν_7	700.5	36.8	711	725
ν_8	606.0	31.5	602	613
ν_9	306.8			
ν_{10}	115.7			

Theoretical frequencies were obtained from Girlando et al.[164] and Bozio et al.[25]

Table 4. *EMV* frequencies and coupling constants for DMTM(TCNQ)$_2$

A_g Mode ν_a	DMTM(TCNQ)$_2$		MEM(TCNQ)$_2$		TCNQ$^-$	
	ν_a (cm^{-1})	g_a (cm^{-1})	ν_a (cm^{-1})	g_a (cm^{-1})	ν_a (cm^{-1})	g_a (cm^{-1})
ν_1	3065	51	3075	40	3052	31
ν_2	2200	302	2210	403	2193	423
ν_3	1593	359	1630	468	1603	1057
ν_4	1406	485	1395	363	1403	392
ν_5	1186	272	1180	298	1209	229
ν_6	963	69	958	89	968	237
ν_7	716	192	718	210	731	263
ν_8	603	88	597	97	607	18
ν_9	324	210	324	172	336	194
ν_{10}	-	-	150	73	148	78

Theoretical frequencies of TCNQ$^-$ taken from Lipari et al.[83] and Bozio et al.[187]
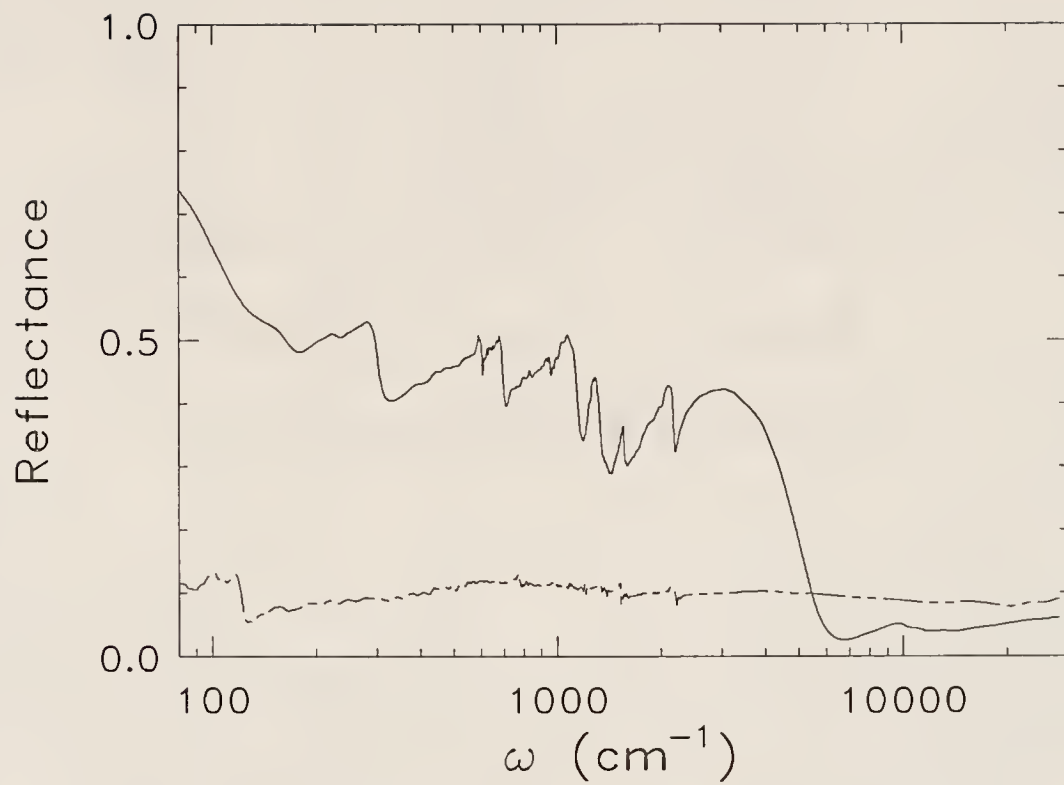
Fig. 26. Room temperature reflectance of NPrQn(TCNQ)$_2$ with light polarized parallel (solid line) and perpendicular (dashed line) to the TCNQ chain direction.

Fig. 27. Reflectance (upper panel) and frequency dependent conductivity (lower panel) of NPrQn(TCNQ)$_2$ with light polarized along the chains at 300 K (solid line) and 100 K (dashed line).
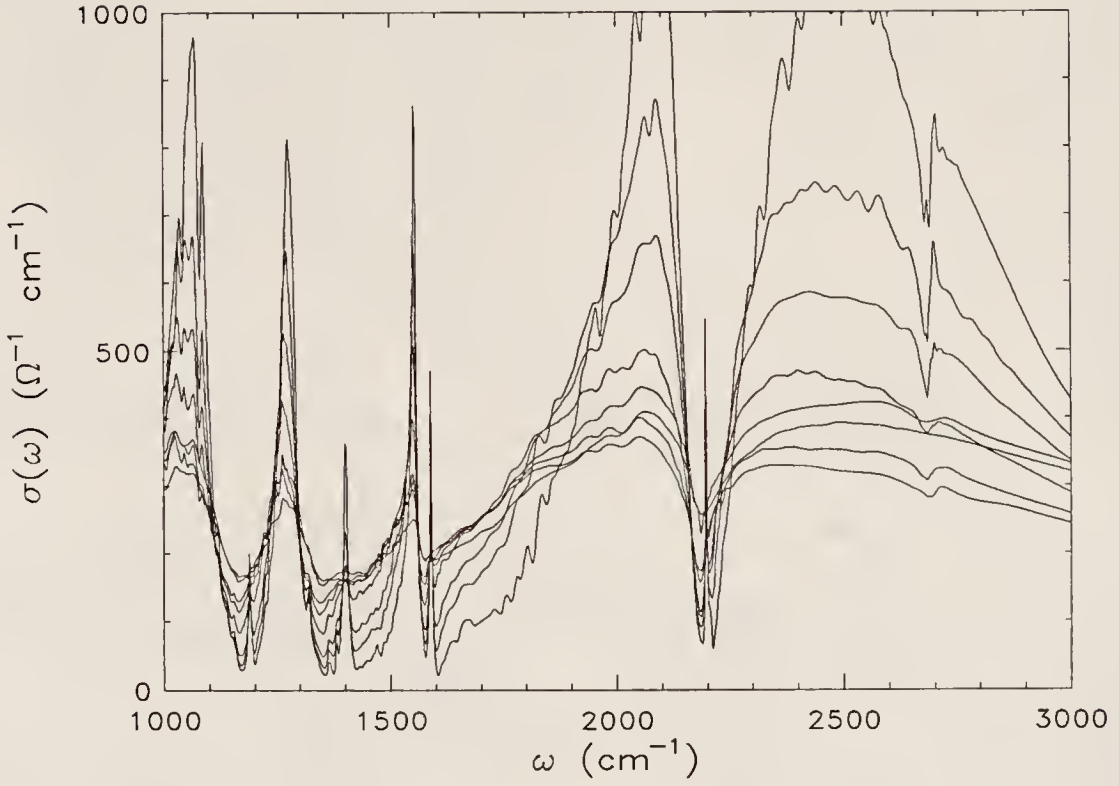
Fig. 28. Temperature dependence of the frequency dependent conductivity of the mid-infrared charge transfer band. Data shown was obtained at: 300, 250, 230, 210, 190, 170, 150, and 100 K. T_c=220 K.
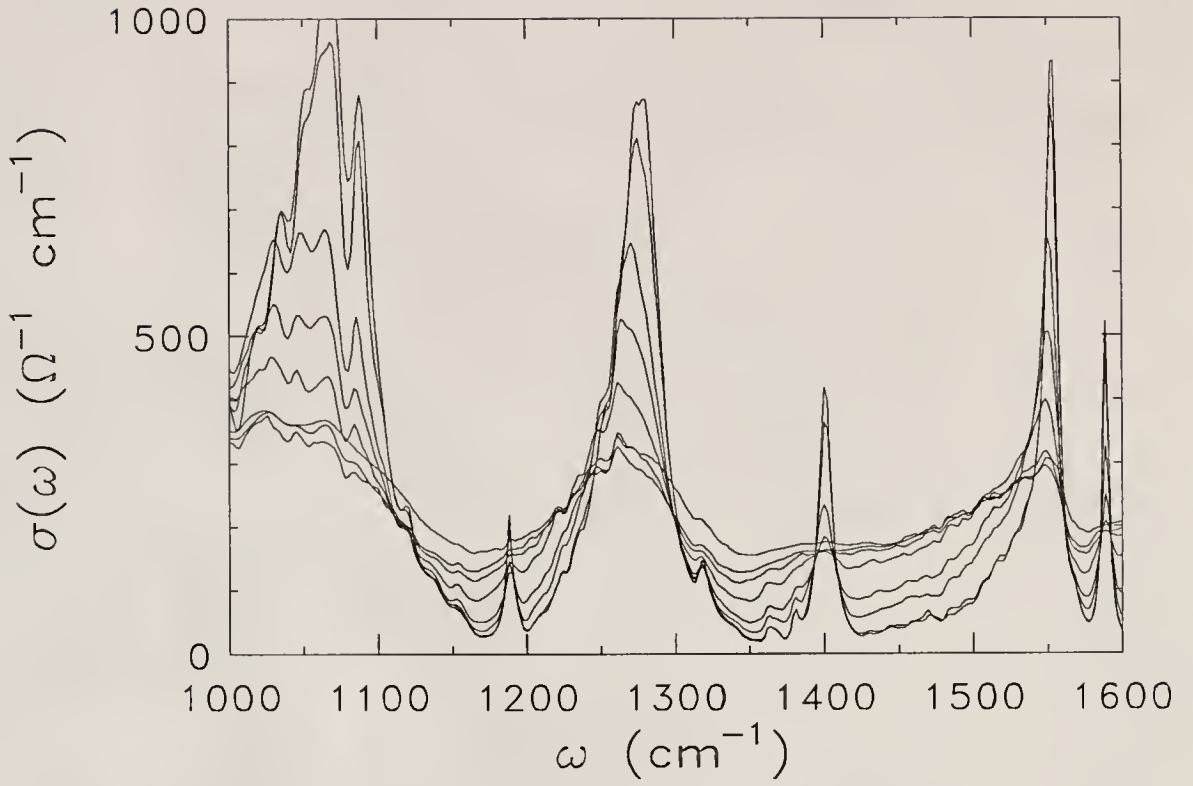
Fig. 29. Enlarged view of typical doublet structure in the frequency dependent conductivity below the phase transition temperature (220 K). Seven temperatures are shown: 210, 200, 190, 170, 150, 100 and 80 K. Intensity increases monotonically with decreasing temperature.
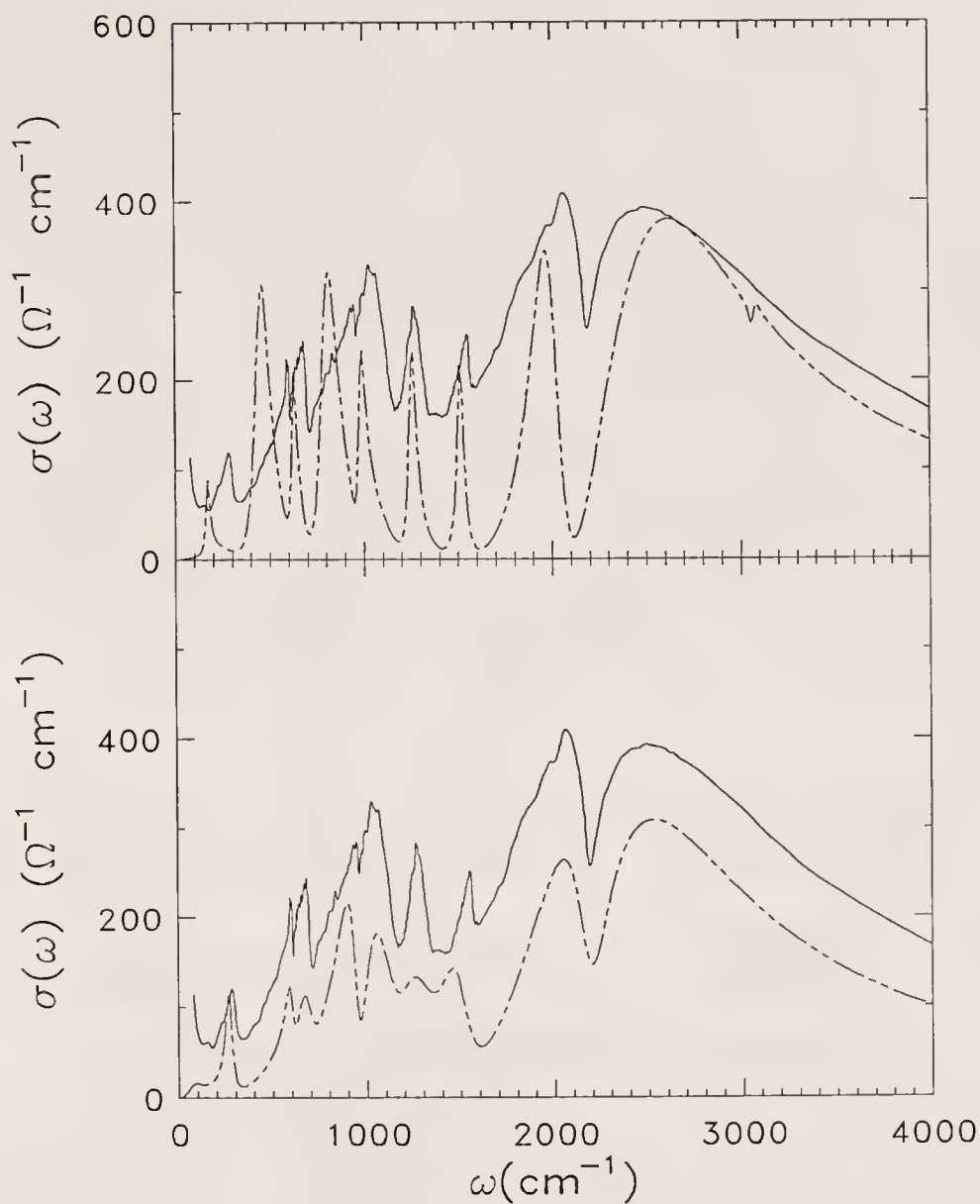
Fig. 30. Upper panel: Isolated dimer model fit to the frequency dependent conductivity at 300 K. Lower panel: Isolated tetramer model fit to the frequency dependent conductivity at 300 K.
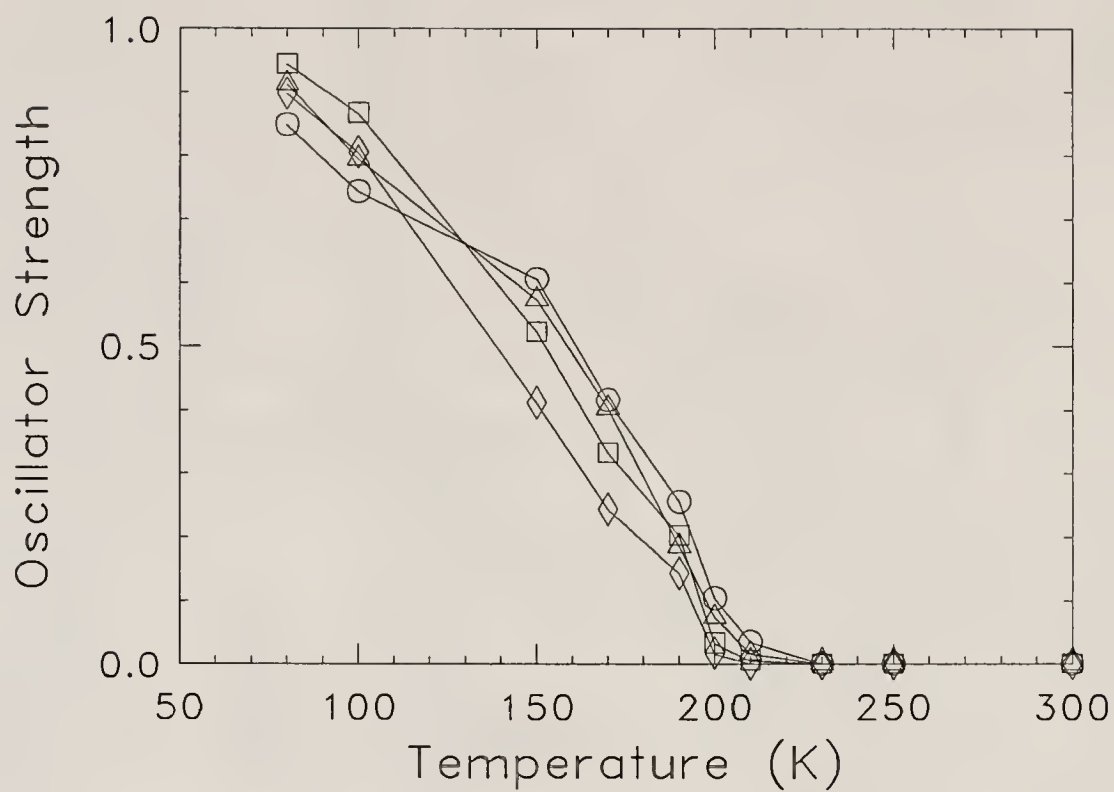
Fig. 31. Normalized intensity of sideband modes associated with four characteristic mid-infrared A_g phonon excitations versus temperature.
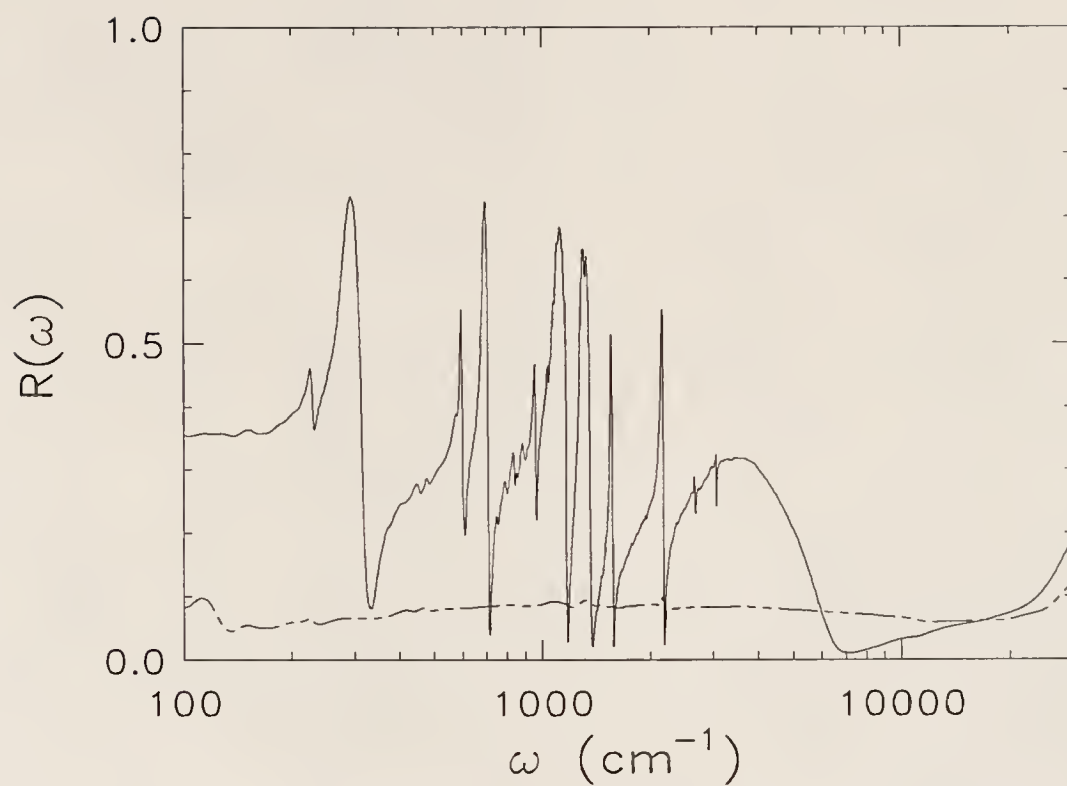
Fig. 32. Room temperature reflectance of DMTM(TCNQ)$_2$, with light polarized along the maximum reflectance direction (solid line) and perpendicular (dashed line) to it on the large (010) crystal face.
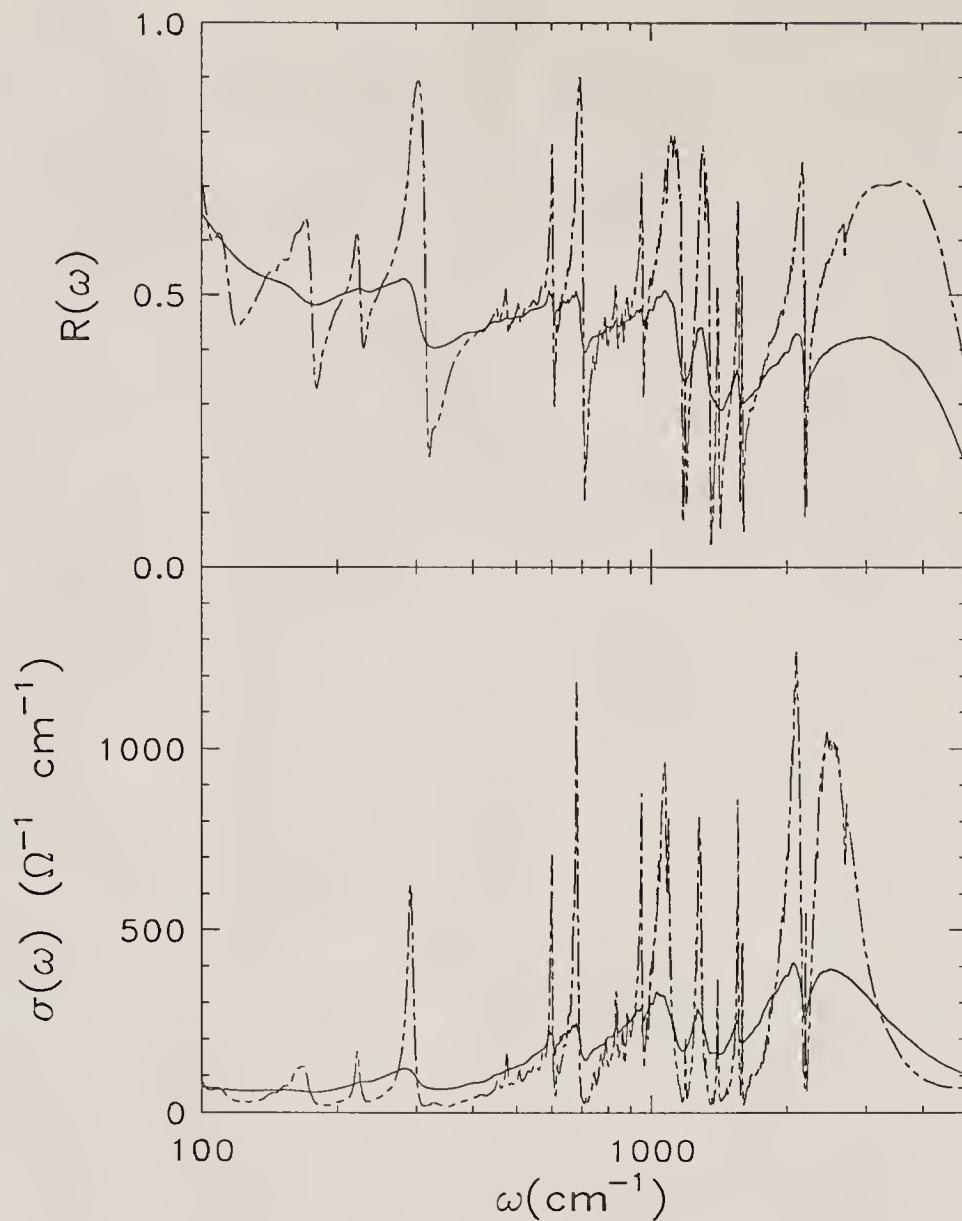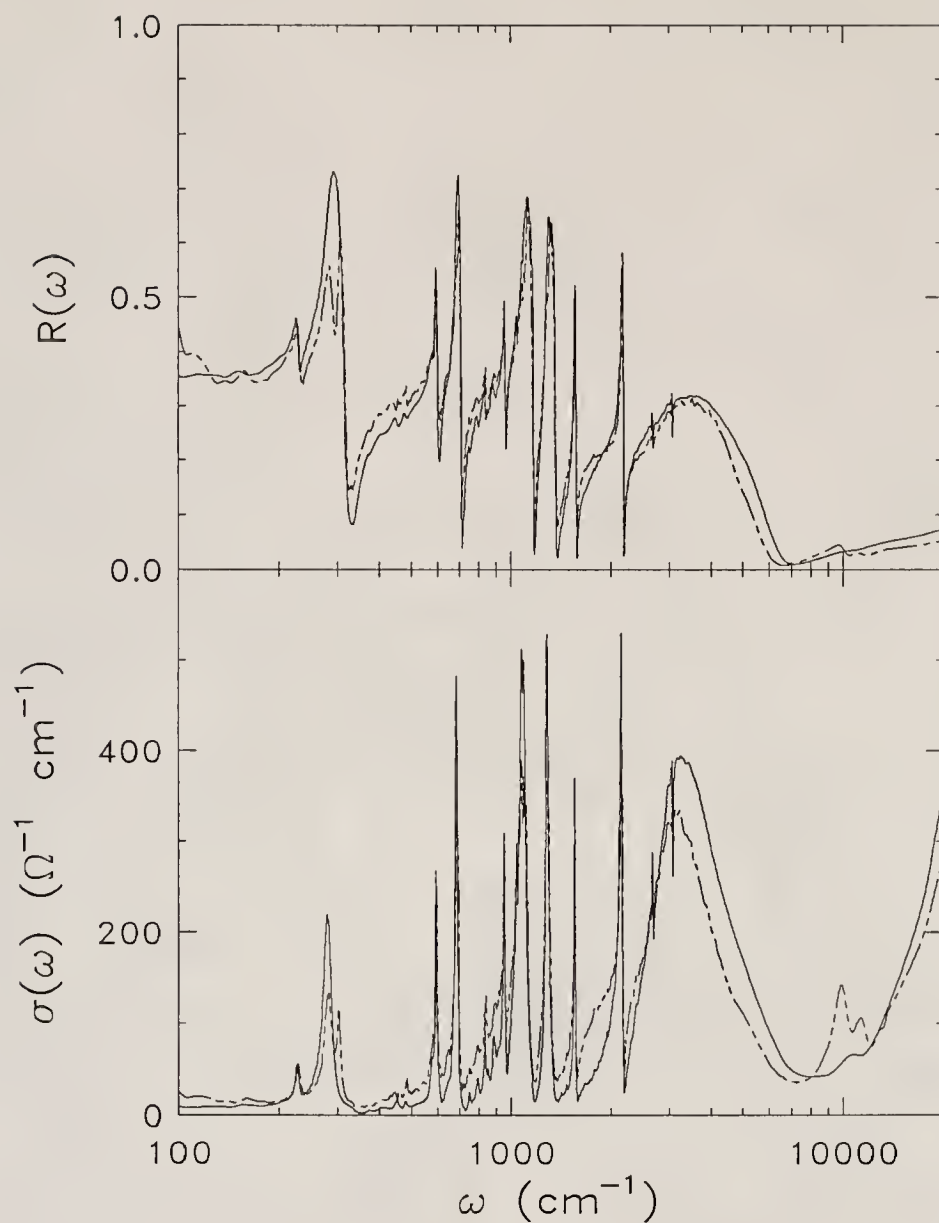
Fig. 33. Reflectance (upper panel) and frequency dependent conductivity (lower panel) of DMTM(TCNQ)$_2$, with light polarized along the maximum reflectance direction on the (010) crystal face at 300 K (solid line) and 150 K (dashed line).
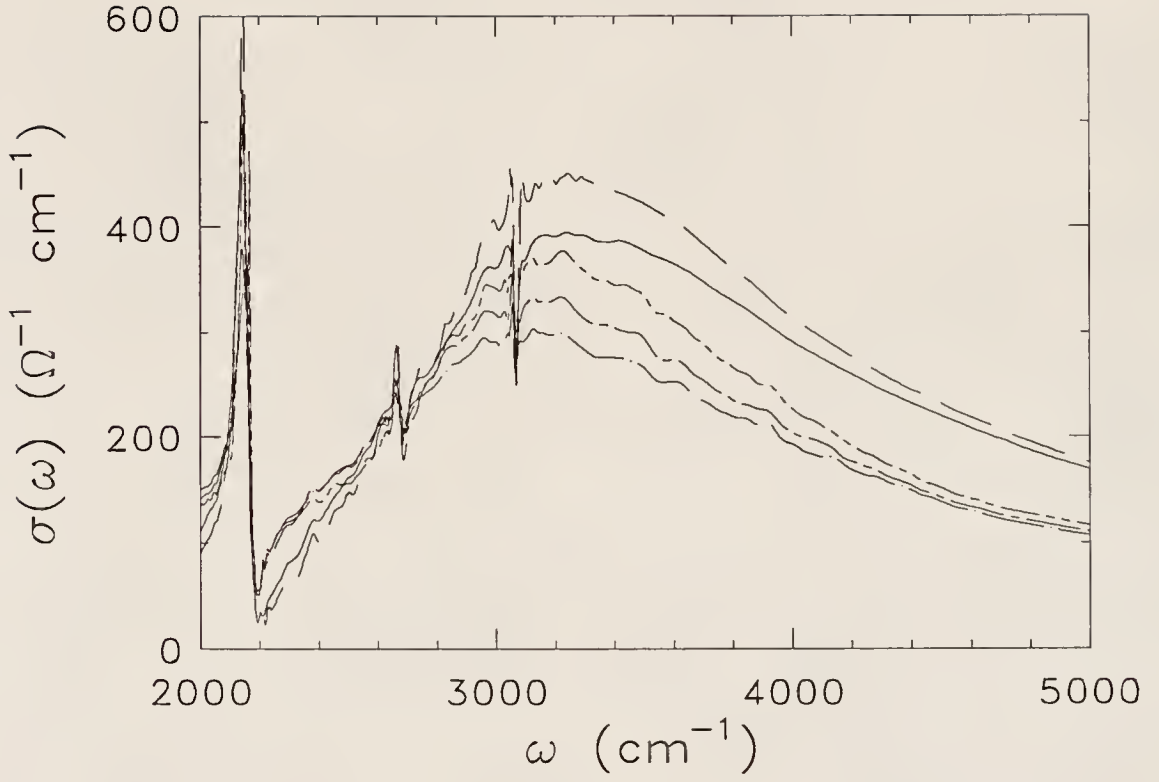
Fig. 34. Detailed temperature dependence of the mid-infrared charge transfer band in the R_{max} direction on the (010) crystal face. Solid line, 300 K; dashed line, 285 K; dashed-with-dot line, 250 K; single-dashed line, 150 K; double-dashed line, 60 K.
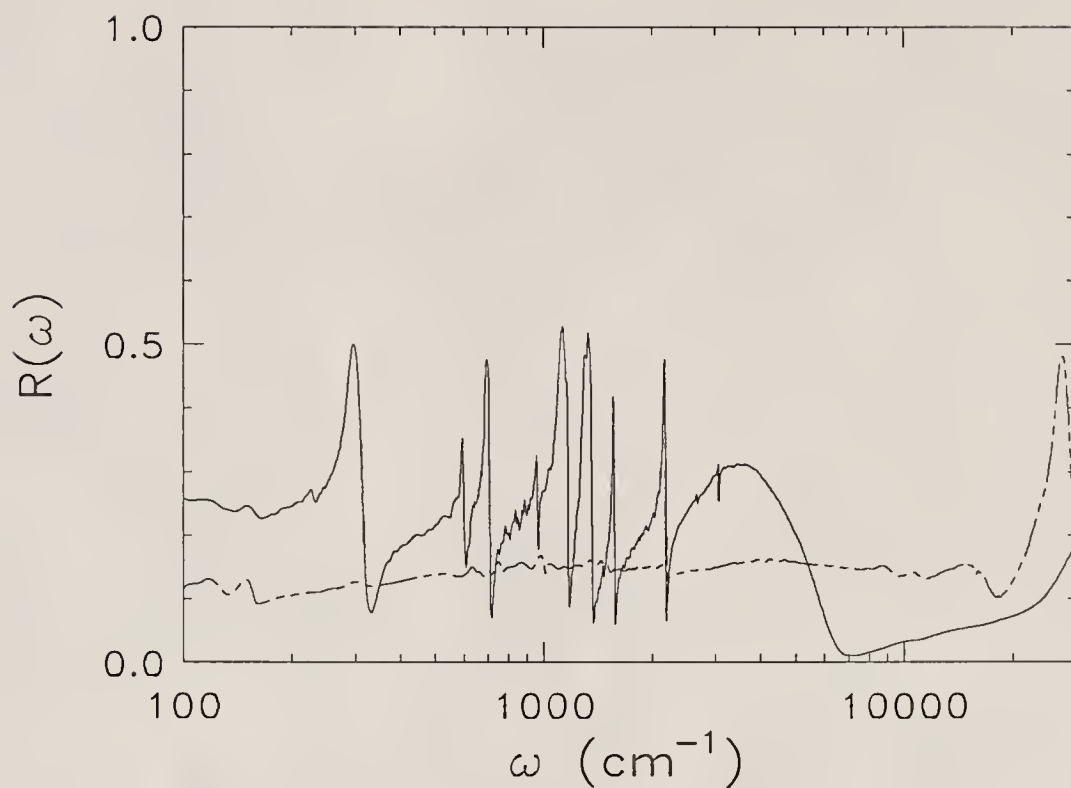
Fig. 35. Room temperature reflectance of DMTM(TCNQ)$_2$, with light polarized along the maximum reflectivity (the c crystallographic axis) (solid line) and perpendicular to the maximum (dashed line) on the (110) crystal face.
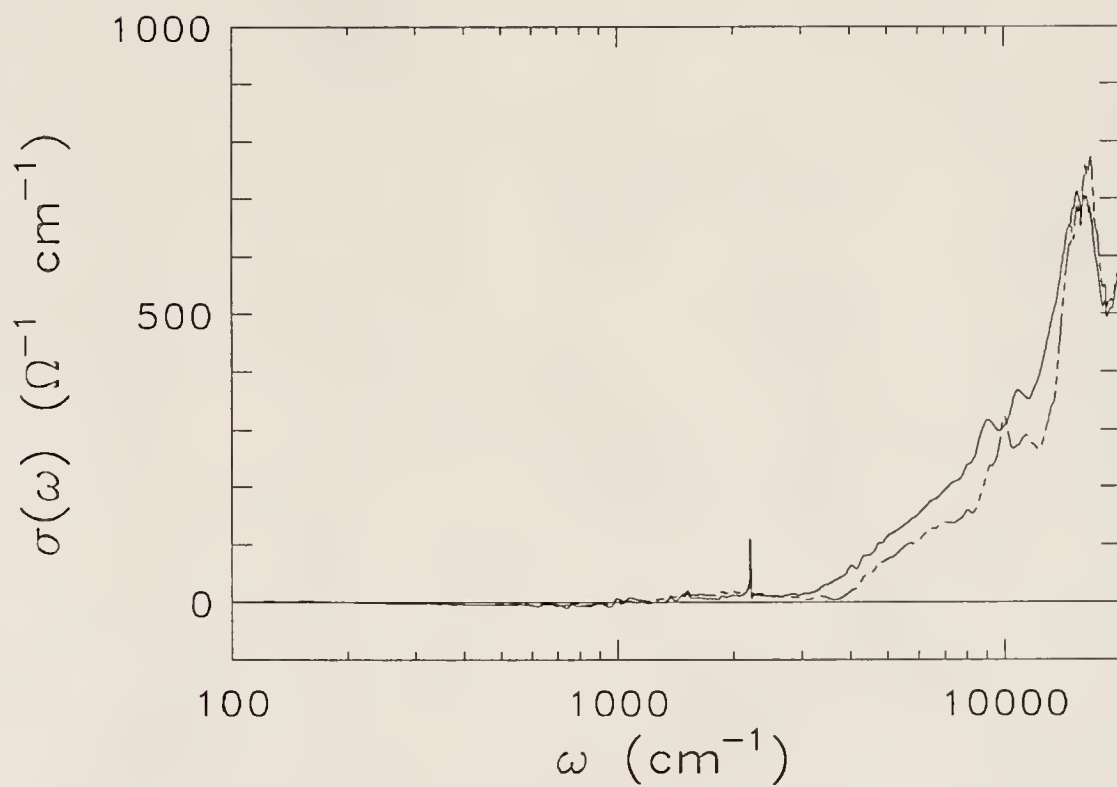
Fig. 36. Frequency dependent conductivity of DMTM(TCNQ)$_2$ with light polarized perpendicular to the c crystallographic axis on the (110) face at 300 K (solid line) and 150 K (dashed line).
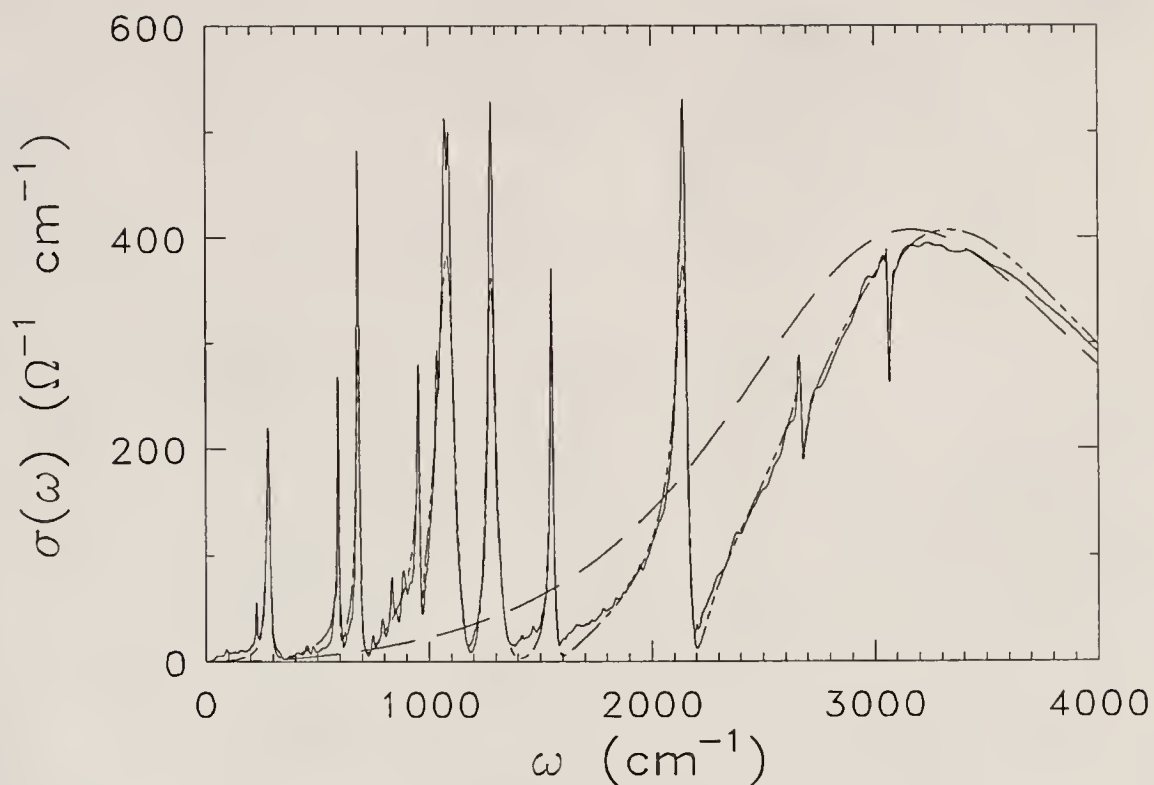
Fig. 37. The fit using the dimer model of Rice et al. to the frequency dependent conductivity of DMTM(TCNQ)$_2$ at 300 K for R$_{max}$ on the large (010) crystal face. Solid line: experimental data; double-dashed line: best fit to the data; dashed line: electronic continuum in the absence of any electron-phonon coupling.
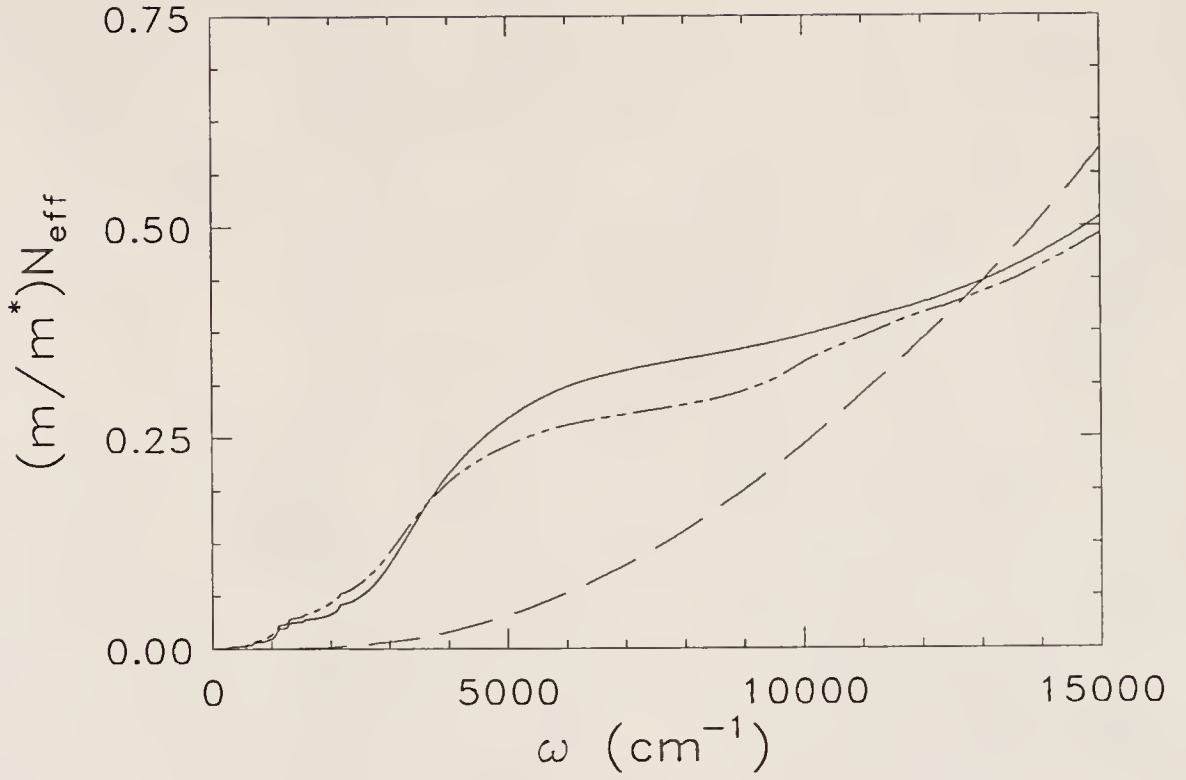
Fig. 38. Sum rule for DMTM(TCNQ)$_2$ for the R_{max} direction on the (010) crystal face at 300 K (solid line) and 150 K (double-dashed line) and the perpendicular polarization at 300 K (dashed line).

CHAPTER VI
RESULTS AND DISCUSSION—HALF-FILLED
ORGANIC CHARGE TRANSFER SALTS

Results: K-TCNQ and RB-TCNQ

Room Temperature Spectra

Figure 39 and Fig. 40 display the room temperature reflectance for polarizations parallel and perpendicular to the a crystallographic (chain) axis for K- and Rb-TCNQ, respectively. Note the logarithmic frequency scale. The infrared spectra of K-TCNQ and Rb-TCNQ are dominated by many sharp vibrational features polarized along the dimerization axis. As in the quarter-filled salts, many of these modes are the totally symmetric (A_g) vibrations of the TCNQ molecule, activated by coupling to charge transfer excitations or charge density wave oscillations.[40,24] At room temperature, nine A_g modes are observed in both K-TCNQ and Rb-TCNQ, most with relatively strong intensity. The coupling seems to be stronger in the potassium crystal, as evidence by the increased intensity of the A_g modes relative to those in the rubidium crystal. Additional vibrational structure in the far and middle infrared is due to TCNQ modes of other symmetry and lattice modes.[19,21,188]

The unperturbed frequencies of the A_g modes for both the K- and Rb- salts are displayed along with theoretical values in Table 5.[83,187] The experimental unperturbed frequencies were determined from a plot of $\mathbf{Re}(\frac{1}{\sigma(\omega)})$ for the 300 K spectra, while the maxima in $\sigma(\omega)$ are tabulated in parenthesis. For these two compounds, the unperturbed frequencies were found to be independent of temperature within experimental error.

As shown in Table 5, the unperturbed A_g frequencies of both alkali-metal salts are in excellent agreement with each other and with previous infrared measurements on the K-TCNQ salt.[107,78] With the exception of the 948 cm^{-1} mode, the data is also in good agreement with A_g phonon frequencies determined directly from Raman measurements and theoretical calculations of TCNQ$^-$.[114,113,112,83,187,188] The discussion in the next section will concentrate on the behavior of the far infrared A_g modes at ≈ 340 cm^{-1} and ≈ 720 cm^{-1} through the phase transition. The character of these modes is primarily ring deformation and C–C wing and ring stretching, respectively.[83]

The reflectivity perpendicular to the maximum reflectance on the (010) face is flat and almost featureless in the mid-infrared. The extreme anisotropy observed between the two polarizations on this crystal face has been observed for many other TCNQ charge-transfer salts as well,[4,18,19,20] once again clearly emphasizing the spectroscopic uniqueness and the quasi-one-dimensional electronic properties of the TCNQ chain direction. It is interesting to note that, perpendicular to the stacking direction, the polarization selection is less good in the Rb- sample than the K- sample; this is likely the consequence of the 23° angle the TCNQ molecule makes with respect to the stacking axis in Rb-TCNQ (*vs.* a 15.8 and 11.3° angle for the two stacks in K-TCNQ) combined with the non-planarity of the TCNQ molecule in the Rb- salt.

The vibrational modes can be divided into two classes. Those involving motion of the TCNQ$^-$ ion itself are classified as intra-molecular in nature, whereas the mode involving collective motion of the TCNQ$^-$ ions or the donor chains are inter-molecular or lattice modes. The intra-molecular modes are at higher energy, and include (in our spectra) the aforementioned totally symmetric phonon modes as well as the infrared allowed modes of B_{1u}, B_{2u} and B_{3u} symmetry. The inter-molecular modes are generally observed at less than 300 cm^{-1}. These modes can be further divided into

translational and librational motions. Both types of motion generally occur at low energy, with the acoustic modes below the frequency limit of infrared spectroscopy.

Neither the acoustic nor the librational modes are intrinsically infrared active, as they involve no changing dipole moment. Consequently, it is unlikely that they will be observed in electric dipole allowed spectroscopy unless they are made infrared active by a strong electron-lattice coupling mechanism.[189,190,191] If such a mechanism is active in these alkali-metal materials, we may observe lattice modes in the far infrared spectra.

The number of modes in each class may be determined as follows. For an isolated molecule, there are $3N$ degrees of freedom, where N is the number of atoms in the molecules. Subtracting the translational and rotational degrees of freedom, the remainder corresponds to the degrees of vibrational freedom of the molecule. In the case of the isolated TCNQ molecule, there are 20 atoms. Thus, there are 54 vibrational normal modes. A good discussion of the symmetry classification and frequency of these modes has been presented elsewhere.[21,188]

For the case of a molecular solid, we want to replace the $3N$ cartesian displacements with a new set of coordinates which separates the internal vibrations from the three external translations of the mass center and the three rotations around it. The intra-molecular modes are expected to closely resemble the 54 normal modes for the isolated TCNQ molecule, although the internal modes may broaden into branches with a weak dispersive nature.[39] The inter-molecular modes, involving cooperative motion of the lattice, depend much more on the nature of the crystal. As indicated above, there are expected to be three acoustic modes, corresponding to the translational degrees of freedom of the crystal. The remaining three degrees of freedom correspond to motions involving the rotational degrees of freedom; these modes are classified as librational. However, due to in-phase and out-of-phase coupling, six

librational modes are actually expected.[21] The librational modes have *gerade* symmetry (A_g and B_g), and therefore are Raman active.[21,113] Depending on the crystal symmetry, several of these modes may be degenerate.

Table 6 and Table 7 display the frequencies, polarization dependence, and symmetry assignments for the phonon modes in the far infrared spectra of K-TCNQ and Rb-TCNQ, respectively. Here, the intra- and inter-molecular frequencies were obtained at 300 K. The A_g frequencies, obtained from normal mode calculations, are included in this list for completeness. Symmetry designation of the non A_g intramolecular modes was accomplished with the aid of theoretical calculations and Raman measurements.[187,188,21,113,114] In general, the intra-molecular modes of non-A_g symmetry for the TCNQ molecule are in good agreement with expected resonance positions. Obviously, the donor cations in these salts do not contribute to the intra-molecular vibrational structure. The inter-molecular modes in Table 6 and Table 7 are more difficult to assign than their intra-molecular counterparts due to a variety of factors. A detailed discussion of these modes, and the rational for the assignment of many of the low energy features as collective lattice modes in the aforementioned Tables, will be presented later.

Temperature Dependence

To compare the spectral differences between the high- and low-temperature phases, the far infrared reflectance of K-TCNQ and Rb-TCNQ are shown for several temperatures and both polarizations in Fig. 41 and Fig. 42, respectively. The frequency dependent conductivity in the chain axis direction is shown in Fig. 43 and Fig. 44. (Note the linear energy scale.) Perpendicular to the chain axis direction, the spectra display little temperature dependence, except in the very far infrared.

Figure 43 and Fig. 44 illustrate the strikingly different behavior of the electron-phonon coupling through the phase transition in these two materials. In the K- com-

pound, the oscillator strength and width of the A_g modes change in a relatively gradual and continuous manner with increasing temperature through T_c. Above T_c, these peaks have not disappeared, and continue to change gradually, retaining both their Lorentzian shape and a significant amount of oscillator strength. In contrast, in the Rb- salt, the A_g modes display little temperature dependence in the low-temperature phase, and are sharply reduced at T_c, with only residual coupling remaining in the high-temperature phase. We observe no temperature dependence in the spectra above T_c.

The temperature dependence of the normalized oscillator strength and linewidth of the 340 and 720 cm^{-1} vibrational modes are displayed in the upper and lower panels of Fig. 45 for the K- and Rb- compounds, respectively. This data was normalized with respect to the limiting zero temperature value for each material. Error bars are $\pm 3\%$ in both phases of K-TCNQ as well as the low-temperature phase of Rb-TCNQ; larger error bars ($\pm 10\%$) are necessary for points in the high-temperature phase of the Rb- salt, where baseline difficulties increased the uncertainty. The linewidth of these same phonon features as a function of temperature is displayed in Fig. 46 for both materials. Here, error bars are $\pm 4\%$ for both phases of the K- salt and the low-temperature phase of the Rb- compound; above T_c, we estimate uncertainties on the order of $\pm 20\%$ for the Rb- salt.

The low energy features display strong temperature and polarization dependence as well (Fig. 41 and Fig. 42). These figures clearly indicate that while the K- and Rb-TCNQ salts may be nearly one-dimensional in terms of electronic properties, the collective lattice properties are multi-dimensional.

The inter-molecular modes (see also Table 6 and Table 7) are more difficult to assign than the intra-molecular modes because of their weak intensity, broadening at higher temperatures, and possible frequency shift due to electron-lattice coupling.

In addition, because of the reduced reliability of normal mode calculations in the far-infrared frequency regime, the lattice mode assignments in Table 6 and Table 7 rely heavily on other factors. The most important factor is the observed temperature dependence, which was used to distinguish between a very low energy intra-molecular or a lattice mode. The assignments also rely upon low energy Raman measurements of the TCNQ molecular crystal and K-TCNQ samples and the subsequent assignment of librational modes by several groups.[21,113,114,112] The polarization dependence was also a useful criterion.

It is of interest to do more than distinguish a mode as a collective oscillation of the lattice or an internal vibration as we have done in Table 6 and Table 7. However, assignment of a collective lattice motion to a purely librational or translational motion is not straightforward. As pointed out by Girlando and Pecile,[21] that this difficult task may be complicated by combination bands arising from mixing between internal and external modes, with these features contributing to the collection of low energy modes as well.

To assign the purely librational modes, we examined the detailed behavior of these low energy modes as a function of temperature. Table 8 and Table 9 show the frequencies of the low energy modes at 300 and 10 K. In both samples, many of the low energy far infrared modes red-shift and broaden with increasing temperature, indicating a softening of the lattice at higher temperature. Strong red-shifting and broadening was the main criteria taken into consideration in the decision to characterize a mode as librational.

Discussion: K-TCNQ and RB-TCNQ

Electron-Phonon Coupling

Among the most prominent and interesting spectral features of TCNQ charge-transfer salts are the ten in-plane A_g vibrational modes of the TCNQ molecule, activated by coupling to a charge-transfer excitation or a charge density wave oscillation.[19,20,22,24,25,164,165] The authors in the aforementioned citations make clear the intimate relationship between the lattice dimerization and the intensity of the A_g vibrational modes: a strong lattice distortion results in a charge density wave with a large amplitude and consequently strong coupling with the vibrational modes of proper symmetry, whereas a weak or non-existent lattice distortion results in little or no coupling. Following Okamoto et al.,[6] we define a reduced lattice dimerization as

$$\xi = \frac{(r_1 - r_2)}{(r_1 + r_2)}, \tag{67}$$

where r_1 and r_2 are the inter- and intra- dimerization separation, respectively. In this way, changes in the oscillator strength of the A_g phonon modes can be related to the changes in the reduced lattice dimerization through the phase transition.

The temperature dependence of the order parameter, Δ, rather than the effective lattice dimerization, is actually the more fundamental quantity with which to probe the nature of the phase transition. Bozio et al. have discussed the relationship between the A_g phonon mode oscillator strengths and the order parameter of the phase transition.[180,181] They find that the oscillator strength of the totally symmetric vibrational modes goes as $\approx \Delta^2$. Thus, by monitoring the integrated oscillator strength of the A_g vibrational modes as a function of temperature, we can also follow changes in the order parameter through T_c.

The data in Fig. 45 and Fig. 46 display the striking contrast between the nature of the phase transition in the K- and Rb- compounds. These curves suggest that the

effective lattice dimerization in K-TCNQ changes gradually in the low-temperature phase, through the phase transition, with a very small discontinuity taking place at T_c. The gradual change continues even in the high-temperature phase, where a non-uniform lattice spacing still present even at 420 K.

We can conclude from the gradual variation of the integrated spectral intensity of the 340 and 720 cm^{-1} A_g modes in K-TCNQ with temperature that the order parameter of the phase transition also changes gradually with temperature in this compound—except at T_c, where there is a weak discontinuity in the curve. Thus, although the structural phase transition is weakly first order, it has a very strong second order component. Consequently, the structural phase transition in the K-salt is best characterized as a second- (rather than first-) order process. Additional evidence for this conclusion has been provided by a variety of transport and magnetic measurements.[99]

In contrast to the other 1:1 salt, the integrated oscillator strength of the A_g phonon modes in the Rb-TCNQ sample display little temperature dependence in the low-temperature phase, a sharp change at T_c, and no temperature dependence above T_c. Thus, for the Rb(I)- salt, we conclude that the the change in lattice dimerization occurs suddenly at T_c as well, moving from a distorted lattice in the low-temperature phase to a uniform lattice (ξ=0) in the high-temperature phase. This result was not unexpected given the violent nature of the phase transition in the Rb(I)- salt as compared to other alkali-metal TCNQ charge transfer salts. It is also interesting to note that the behavior of the Rb(I)- crystal (presented here) is quite different from that of the other crystalline modification of the Rb(II)- salt,[109,110] which displays a more gradual change in the EMV coupling through the phase transition.

The nearly temperature independent variation of the oscillator strength of the A_g vibrational modes in the high- and low-temperature phases of the Rb- salt, combined

with the sharp discontinuity at T_c, shows that the order parameter changes abruptly at T_c and falls to nearly zero. Thus, we find that the structural phase transition in Rb-TCNQ is strongly first order. This conclusion is in good agreement with previous transport and magnetic measurements.[99]

The results in Fig. 45 and Fig. 46 are in good agreement with those of Okamoto et al[6] for the temperature dependence of the CN stretching mode near 2200 cm^{-1}. The changes in lattice dimerization suggested by these curves is also analogous to the results of superlattice reflection measurements by Terauchi, shown in Fig. 15.[17] This similarity highlights the important connection between the electron-phonon coupling and the structural distortion, which is the basis for much of the spectroscopic work presented here and elsewhere on the charge transfer salts.

Although the phase transition is largely driven by the structural distortion, the cations play a critical role in the distortion process for these 1:1 compounds, as evidenced by the results of Fig. 45. Several factors may interact to influence the nature of the TCNQ stacking; these include the intra- and inter-dimer spacing, the mode of overlap within the stack, the size of the cation and how the external cation potential interacts with the TCNQ chain. The intra-dimer as well as the inter-planar distances are significantly shorter in the Rb- compound, which is surprising, given the increased size of the Rb- cation. In both materials, the environment of the alkali-metal cation consists of a distorted cube, with the corners of the cube being defined by eight N atoms. The Rb- cation is at the center of a slightly larger cube, as indicated by M^+–N distances.[95,96] Accommodation of the cation may account for the large molecular tilt along the TCNQ stacking axis as well as the boat-shape of the TCNQ molecule in the Rb- compound. However, the most important structural distinction between the two materials is the intra- and inter-dimer overlap. In the low-temperature phase of K-TCNQ, a slightly shifted (along the TCNQ short axis)

ring-ring overlap is observed in the dimeric unit, while between dimers, there is a modified ring-ring overlap with a small diagonal shift of the molecular center. Above T_c, K-TCNQ has a modified ring-ring overlap intermediate between those observed in the low-temperature phase.[95] In the low-temperature phase of the Rb- compound, the intra-dimer overlap is very similar to that in the K- material, where the ring-ring overlap is shifted along the short axis of the molecule. However, the inter-dimer overlap is significantly different in the Rb- material with a 2.2 Å diagonal offset (primarily a long axis shift) between molecular centers. This results in six atoms lying virtually on top of each other, which is a very high energy configuration. If the structure of the high-temperature phase is to be even remotely similar to the structure of the uniform phase in K-TCNQ, a concerted shifting and twisting motion must take place. Structural studies above T_c would be very useful to ascertain the nature of this motion.

Fritchie[192] has suggested inter-columnar interactions dictate the mode of shift in a charge transfer salt. Our study has highlighted such an example. Here, the cation is primarily responsible for the different manner of stacking in the two materials—particularly influencing the mode of overlap between dimeric units. It is likely that the inter-dimer overlap represents a structural barrier to the movement between the high- and low-temperature phases. Consequently, we suggest that it is the cation (or the external cation potential) which is responsible for the striking differences in the TCNQ stacking geometry, and thus, the behavior of the K- and Rb-TCNQ salts through the phase transition.

Finally, although a quantitative and more detailed analysis of the electron-phonon coupling in the mid-infrared will be presented elsewhere, it is interesting to think about the effect of the differences in lattice dimerization between these two materials in terms of probable success of various models of the electron-phonon coupling. Of

the alkali-metal based TCNQ charge transfer salts, Rb-TCNQ is the most strongly dimerized due to the extremely short intra-dimer distance (3.159 Å) as well as the slightly offset ring-ring overlap between TCNQ molecules in the dimer. Between dimers, the structural overlap is a diagonally slipped ring-bond overlap, which is not expected to be conducive to a delocalized electronic wavefunction. A more localized wavefunction and reduced interactions along the TCNQ stack likely result in a smaller bandwidth. Yakushi et al.[106] report values of t, U, and V for Rb-TCNQ which are in very close agreement with those of the potassium salt, also emphasizing the importance of electron-electron interactions in this material. Thus, Rb-TCNQ is probably in the intermediate to large U regime. Given these considerations, it is expected that this compound will have electron-phonon coupling properties that should be closely described by the isolated dimer model in the low-temperature phase.[166] On the other hand, it has already been shown by the Padova group that the isolated dimer model is inappropriate for the K- salt below T_c. This probably results from a combination of considerations, including the longer inter-dimer separation and better ring-ring overlap, both of which result in a greater degree of electronic interaction between dimer units, and the fact that $U \approx 4t$. Hence, a phase phonon based model is expected to be more appropriate for K-TCNQ, as it gives more emphasis to the extended character of the material in the coupling process.

The Lattice Modes

The low frequency lattice modes are also a sensitive probe of the structural changes which accompany a structural phase transition. These features are generally expected to be observed at low energy (near zero wavevector) due to the shape of the acoustic and librational dispersion curves. With the structural distortion occurring along the a axis, lattice modes polarized in the chain direction are expected to be the most useful. Of course, any change in the size of the unit cell should result

in either lattice mode splitting or combination, depending on whether the crystal symmetry is increased or decreased by the phase transition.

We have tentatively assigned many of the weak modes at at low energy as the lattice modes in K- and Rb-TCNQ. These assignments are given in Table 6 and Table 7. The inter-molecular features are further classified as such because they display temperature dependence which is clearly quite different from the features which are known to be intra-molecular in nature. At low-temperature, many of the the lattice modes are split into several subbands. This fine structure is likely a result of the many TCNQ molecules in the unit cell. However, much of the interesting vibrational structure and several weak shoulder bands is lost due to broadening and superposition with nearby modes even at 200 K. As the temperature increases in the low-temperature phase, the mode center red-shifts. Above 300 K, many of the modes become extremely broad, making even a determination of the center frequency difficult. Thus, following the softening further is not easy or reliable. In a very few cases, it is possible to discern splitting again above T_c, indicating a change in selection rule or Brillouin zone size at T_c.

Table 8 and Table 9 display the temperature dependence (300 and 10K) of the lattice modes for K-TCNQ and Rb-TCNQ, respectively. It should be mentioned here that there is also a feature at 40 cm^{-1} in the Rb- salt as well, but it is very weak and distorted due to the close proximately to the low frequency Kramers-Kronig extrapolation regime. A few of the modes display pronounced temperature dependence, and we further classify them as librational modes. In the K- salt, these include the features at 91, 114.7, 129, 135.5, and 146.6 cm^{-1}, while in the Rb- salt, these include the modes at 98.4, 99.8, 113.8, 114.3, and 129.2 cm^{-1}.

Because of the similarities between the two compounds in this study, it was expected that the frequencies of the TCNQ$^-$ librations should be nearly identical. Our

results indicate that this is not the case, suggesting that cation motion is involved (perhaps coupled as a translation) in these infrared active lattice processes as well. However, the cation mass difference does not fully account for the observed frequency differences, suggesting that a more complicated mechanism is at work.

As the *gerade* symmetry designation of the lattice modes permits Raman activity, this provides an opportunity for comparison with low energy Raman measurement on the neutral TCNQ molecular crystal as well as on a K- salt. For the neutral TCNQ molecular crystal, Girlando et al.[21] report Raman active lattice modes at 41, 76, 97, 105, 133, and 144 cm^{-1}, respectively. All are classified as librational. Studies on K-TCNQ suggest that the lattice modes are placed quite differently in this material.[113,114] Truong and Carlone report[113] Raman active lattice mode frequencies of 70, 81, 110, 170, 229, and 295 cm^{-1}, with the lowest three designated as librational features. It has also been reported[114] that these modes decrease in intensity with increasing temperature in the low-temperature phase.

Although Raman data is unavailable for Rb sample, low energy modes were assigned based upon the display of similar characteristics, including the resonance frequency, line shape, polarization, and the red shift as a function of temperature. Thus, as in the K- compound, the most strongly temperature dependent modes in Rb-TCNQ have been classified as librations: 98.4, 99.8, 113.8, 114.3, and 129.2 cm^{-1}, respectively.

A comparison of the Raman results with the data in Table 8 shows poor agreement with the frequencies determined from Raman measurements on the molecular crystal, as well as with those obtained via Raman measurements of the K- salt. The librational frequencies of the Rb- salts (Table 9) are also not in good agreement with those reported from Raman measurements on the TCNQ molecular crystal or the K- salt. It is not entirely unexpected that the frequency of lattice modes in the infrared do

not coincide with those obtained from Raman measurements, due to the unit cell inversion center (and subsequent mutual exclusion of activity) in the alkali-metal charge transfer salts.

If the 395 K structural phase transition in K-TCNQ were purely second order, one of the lattice mode frequencies would be expected to shift toward zero frequency and eventually disappear with increasing temperature. Such a softening occurs when the correlation lengths are becoming infinite and is related to the stability of the lattice. This behavior is not observed in either the K- or Rb- salt, although the extreme line width broadening above 350 K makes it difficult to confirm conclusively. Consequently, although there have been many indications that the phase transition in the K- salt has a strong second order component, the behavior of the lattice modes show that it is not a purely second order process.

Several aspects of this analysis may form the basis for future study in these materials. The softening of the lattice modes polarized along the TCNQ stacking direction may play a special role in the process of the phase transition, and thus, should be the subject of continued study. In addition, the role of the cation in these lattice processes is not clear, although it seems to have an important effect upon the frequency of the lattice and librational features.

Charge Transport

A uniform lattice spacing (closely approximated in the high-temperature phases of the two alkali-metal salts in this study) often results in metallic conductivity. However, the role of the on-site Coulomb interaction is the critical factor in determining the high-temperature phase transport properties in these two materials.

K-TCNQ is in the intermediate coupling regime, where $U \approx 4t$.[94] Thus, the double occupation of the TCNQ sites is unfavorable, resulting in a totally filled lower Hubbard band (of singly-occupied states) and a completely empty doubly-occupied band

states at higher energy. Conduction can proceed only by thermal activation over the Hubbard gap, so the material is a semiconductor. In the Rb- salt, the smaller band-width likely places this material in the large U regime. Hence, the electrons remain localized on their individual sites and this argument is even stronger. Despite the nearly uniform inter-molecular spacing along the TCNQ stack and the reduced oscillator strength of the totally symmetric phonon modes, the spectra of both materials above T_c are characteristic of a semiconductor, displaying sharp vibration features of other symmetry and no evidence of a free carrier contribution to the frequency dependent conductivity. The only evidence for an increased dc conductivity in the high-temperature phase comes from a slight increase in the reflectivity at very low frequency. Below T_c, the spectra of the K- and Rb- salts are also characteristic of a highly localized material, with strong vibrational features, including those of A_g symmetry.

Table 5. A_g Vibrational Modes for K-TCNQ and Rb-TCNQ

A_g Mode ν_a	K-TCNQ ν_a (cm^{-1})	Rb-TCNQ ν_a (cm^{-1})	TCNQ$^-$ ν_a (cm^{-1})
ν_2	2194.9 (2181.4)	2200.7 (2179.5)	2228
ν_3	1592.1 (1575.8)	1591.2 (1577.9)	1602
ν_4	1361.7 (1332.7)	1369.4 (1348.2)	1454
ν_5	1193.9 (1180.4)	1193.9 (1182.3)	1207
ν_6	827.4 (823.6)	829.4 (825.5)	948
ν_7	723.3 (719.4)	721.3 (719.4)	711
ν_8	618.1 (617.2)	618.0 (617.2)	602
ν_9	336.1 (328.3)	333.0 (326.0)	334
ν_{10}	150.0 (148.5)	153.8 (152.9)	-

Theoretical TCNQ$^-$ frequencies obtained from Lipari et al.[83] and Bozio et al.[187] Frequencies in parentheses are the perturbed frequencies, obtained from the maxima in $\sigma(\omega)$.

Table 6. FIR Vibrational Modes for K-TCNQ.

Freq. (cm^{-1})	Polar.	Stength	Symm. Assign.
55.9	EH	vw	lattice
59.0	EV	vw	
80.0 (br)	EV	vw	
91.0	EH	vw	lattice
104.6	EH	vw	lattice
114.7	EV	w	lattice
120.5	EH	w	lattice
129.5	EH	vvw	lattice
135.5	EV	vw	lattice
146.6	EH	vw	lattice
148.5	EV	w	A_g (ν_{10})
178.4	EV	vw	lattice ?
179.8	EH	vw	lattice
231.9	EV	s	B_{3u} (ν_{53})
336.1 (328.3)	EV	vs	A_g (ν_9)
479.8	**EV**, EH	s	B_{3u} (ν_{52})
516.9	EH	vw	B_{3u} (ν_{47})
548.7	EH	vw	B_{1u} (ν_{25})
618.1 (617.2)	EV	w	A_g (ν_8)
723.3 (719.4)	EV	m	A_g (ν_7)

(br) designates an especially broad feature.

Table 7. FIR Vibrational Modes for Rb-TCNQ

Freq. (cm^{-1})	Polar.	Stength	Symm. Assign.
58.5	EV	vvw	lattice or B_{2u} ?
70.4	EV	w	lattice
72.0, 76.7 (sh)	EH	w	lattice
90.1	EH	w	lattice
98.4	EV	vw	lattice
99.8	EH	w	lattice
113.79	EV	vw	lattice
114.3	EH	vw	lattice
129.2	EV	w	lattice
148.5	EH	vw	B_{1u} (ν_{26}) ?
152.9	EV	w	A_g (ν_{10})
155.3	EH	vw	
175.2	EH	vw	lattice
180.0	EV	vw	
237.7,	**EV**, EH	m	B_{3u} (ν_{53})
333.0 (326.0)	EV	vs	A_g (ν_9)
482.7, 473.5	**EV**, EH	s	B_{3u} (ν_{52})
514.4	EH	vw	B_{3u} (ν_{47})
546.6	EV, **EH**	vw	B_{1u} (ν_{25})
618.0 (617.2)	EV	w	A_g (ν_8)
721.3 (719.4)	EV	m	A_g (ν_7)

(sh) designates a shoulder band.

Table 8. Temperature Dependence of FIR Vibrational Modes for K-TCNQ

300 K Freq. (cm^{-1})	10 K Freq. (cm^{-1})	Polarization
55.9	57.86	EH
59.0	59.3	EV
80.0 (br)	80.0 (br)	EV
91.0	98.85, 103.2	EH
104.6	109.5	EH
114.7	124.9, 128.3, 132.1	EV
120.5	123.9	EH
129.5	134.5	EH
135.5	140.3, 146.1	EV
146.6	149.0, 154.8, 171.7	EH
148.5 (ν_{10})	152.8	EV
178.4	181.3	EV
179.8	184.2, 189.0	EH

(br) designates an exceptionally broad feature.

Table 9. Temperature Dependence of FIR Vibrational Modes for Rb-TCNQ

300 K Freq. (cm^{-1})	10 K Freq. (cm^{-1})	Polarization
58.5	60.27	EV
70.4	76.18	EV
72.0; 76.7 (sh)	75.2; 81.5, 86.3	EH
90.1	94.5	EH
98.4	97.9, 105.6	EV
99.8	105.6	EH
113.8	112.8, 120.0	EV
114.3	120.5	EH
129.2	135.0	EV
148.5	149.0	EH
152.9 (ν_{10})	154.7	EV
155.3	156.7	EH
175.2	177.9, 179.9	EH
180.0	180.0	EV

(sh) designates a shoulder feature.
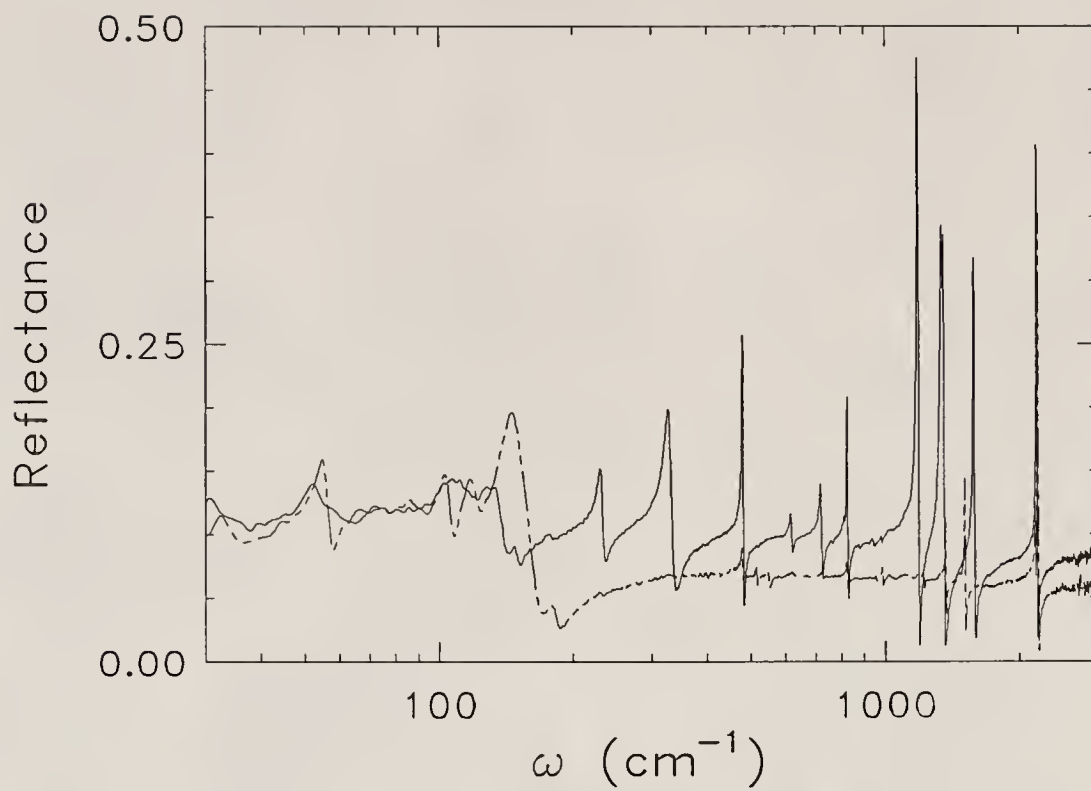
Fig. 39. Room temperature reflectance of K-TCNQ, polarized parallel (solid line) and perpendicular (dashed line) to the stacking axis, a.
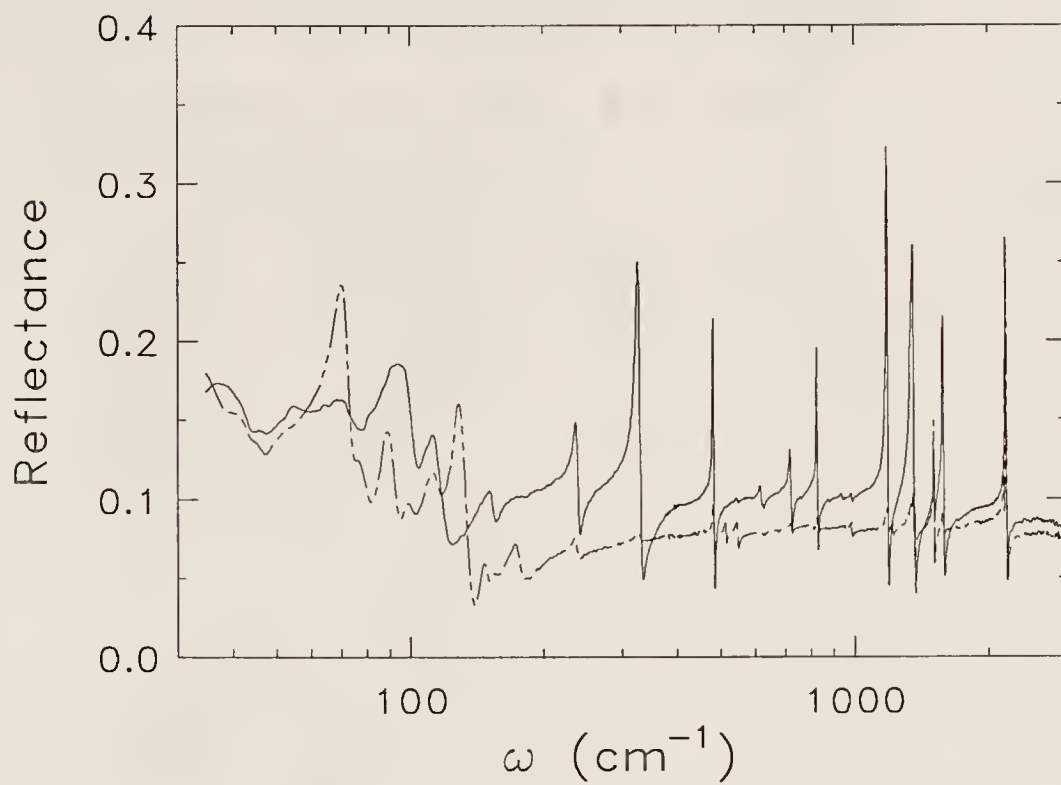
Fig. 40. Room temperature reflectance of Rb-TCNQ, polarized parallel (solid line) and perpendicular (dashed line) to the stacking sxis, *a*.
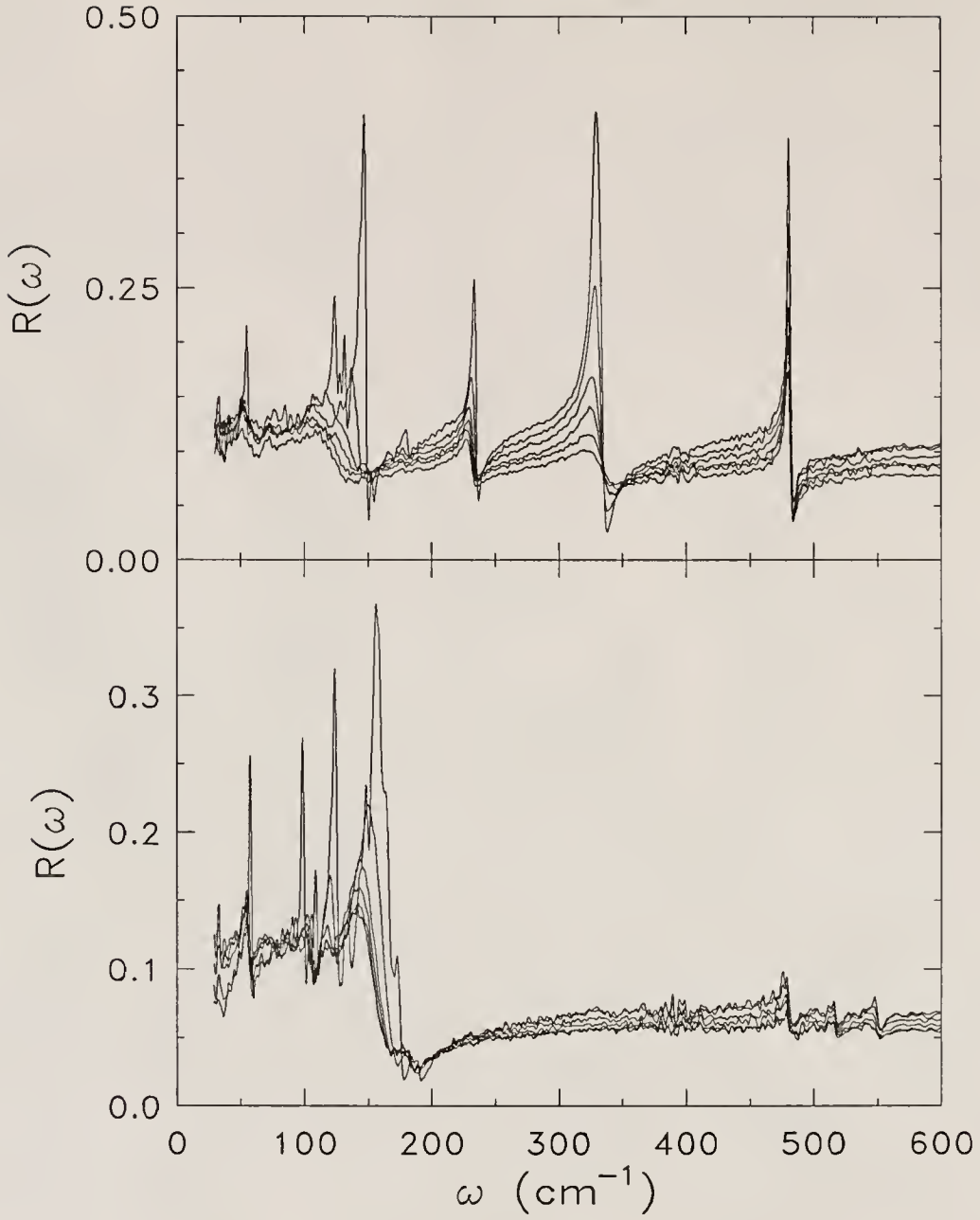
Fig. 41. Upper panel: Temperature dependence of the far infrared reflectance of K-TCNQ along the stacking axis, a; Lower panel: Temperature dependence of the far infrared reflectance of K-TCNQ perpendicular to the stacking axis. Temperatures shown: 10, 200, 330, 390, and 420 K. T_c=395 K.
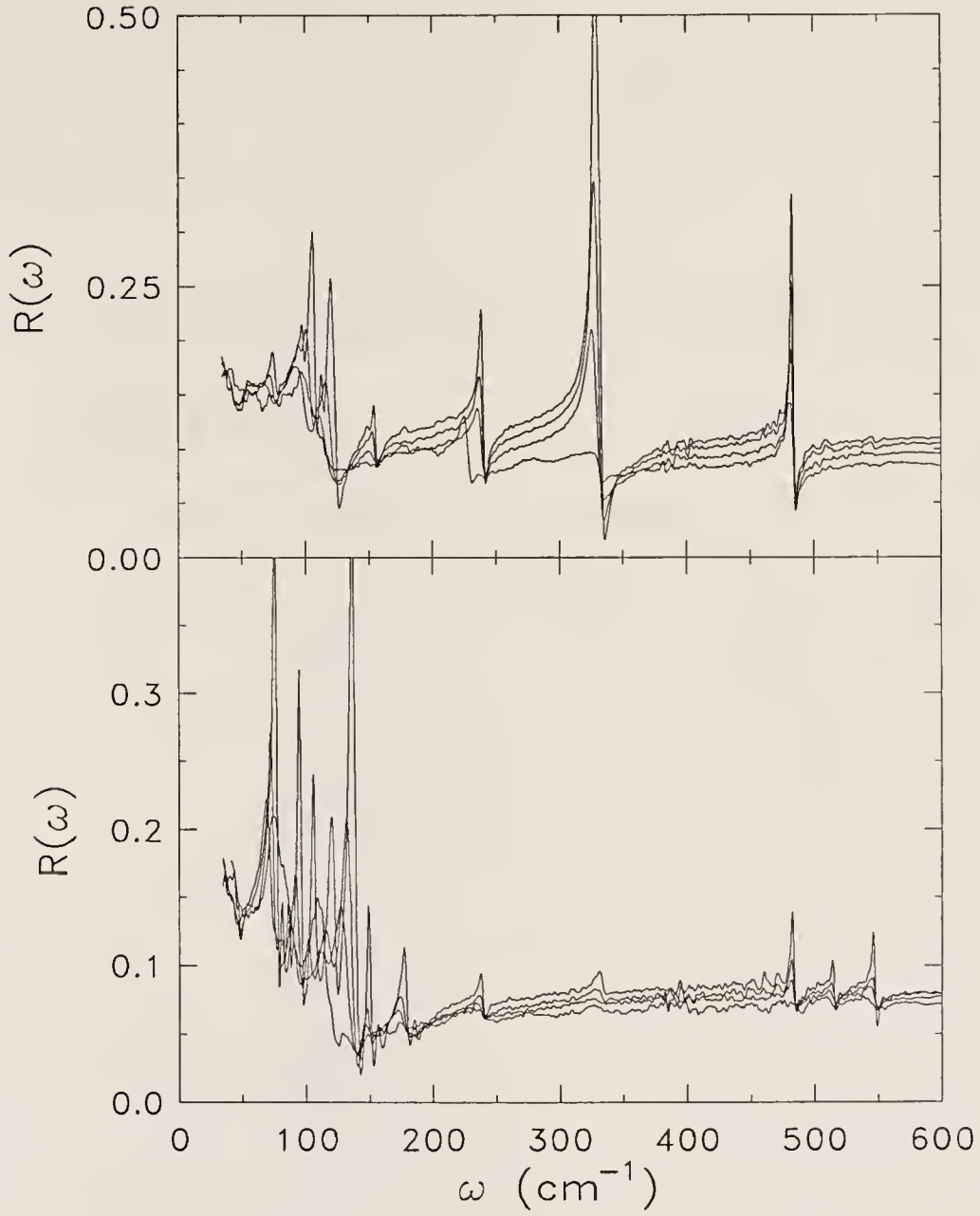
Fig. 42. Upper panel: Temperature dependence of the far infrared reflectance of Rb-TCNQ along the stacking axis, *a*. Lower panel: Temperature dependence of the far infrared reflectance of Rb-TCNQ perpendicular to the stacking axis. Temperatures shown: 10, 300, 370, and 410 K. T_c=381 K.
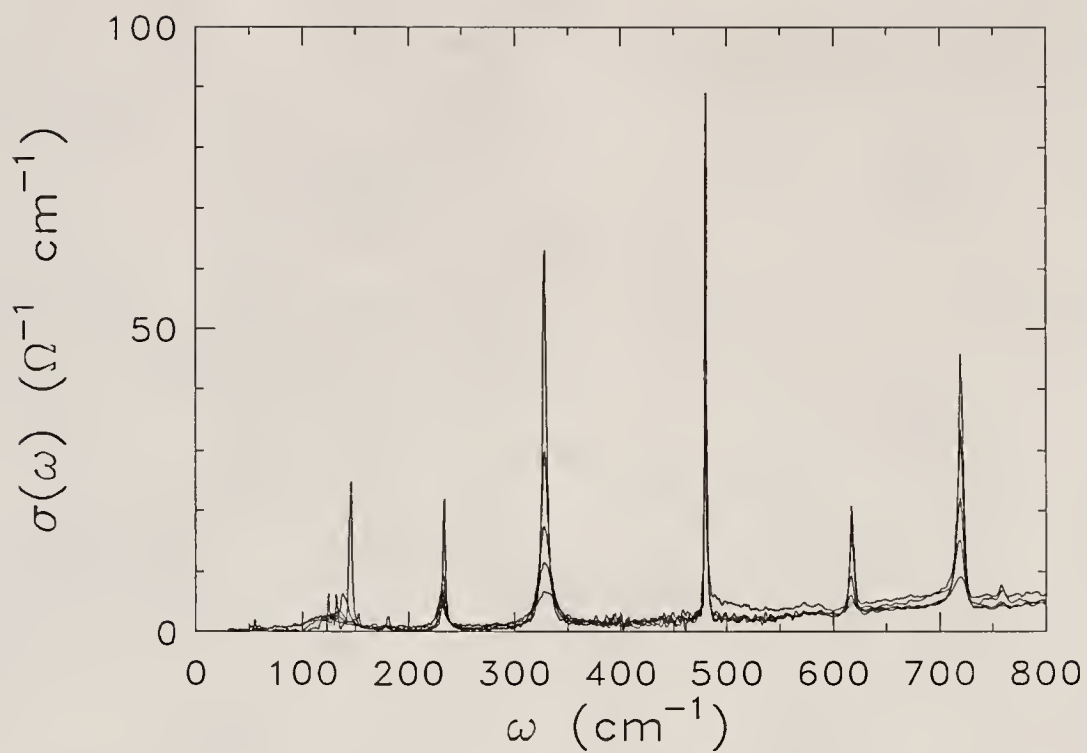
Fig. 43. Temperature dependence of the far infrared frequency dependent conductivity of K-TCNQ along the stacking axis, *a*. Temperatures include: 10, 200, 330, 390, and 420 K.
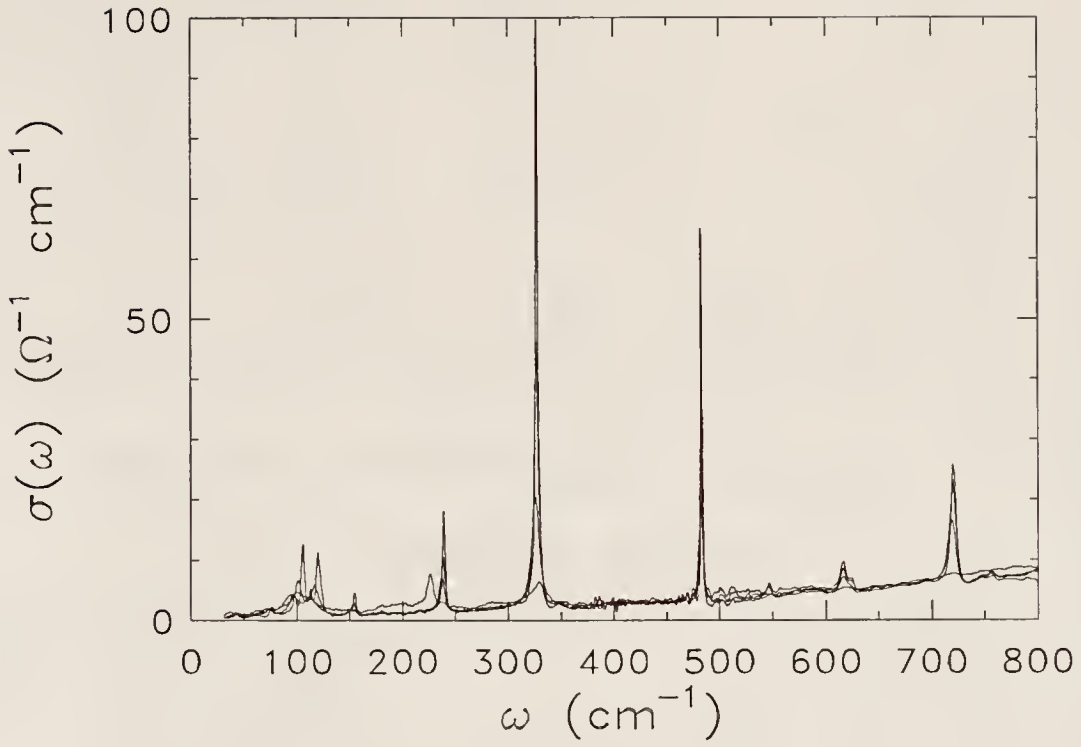
Fig. 44. Temperature dependence of the far infrared frequency dependent conductivity of Rb-TCNQ along the stacking axis, *a*. Temperatures include: 10, 300, 370, and 410 K.
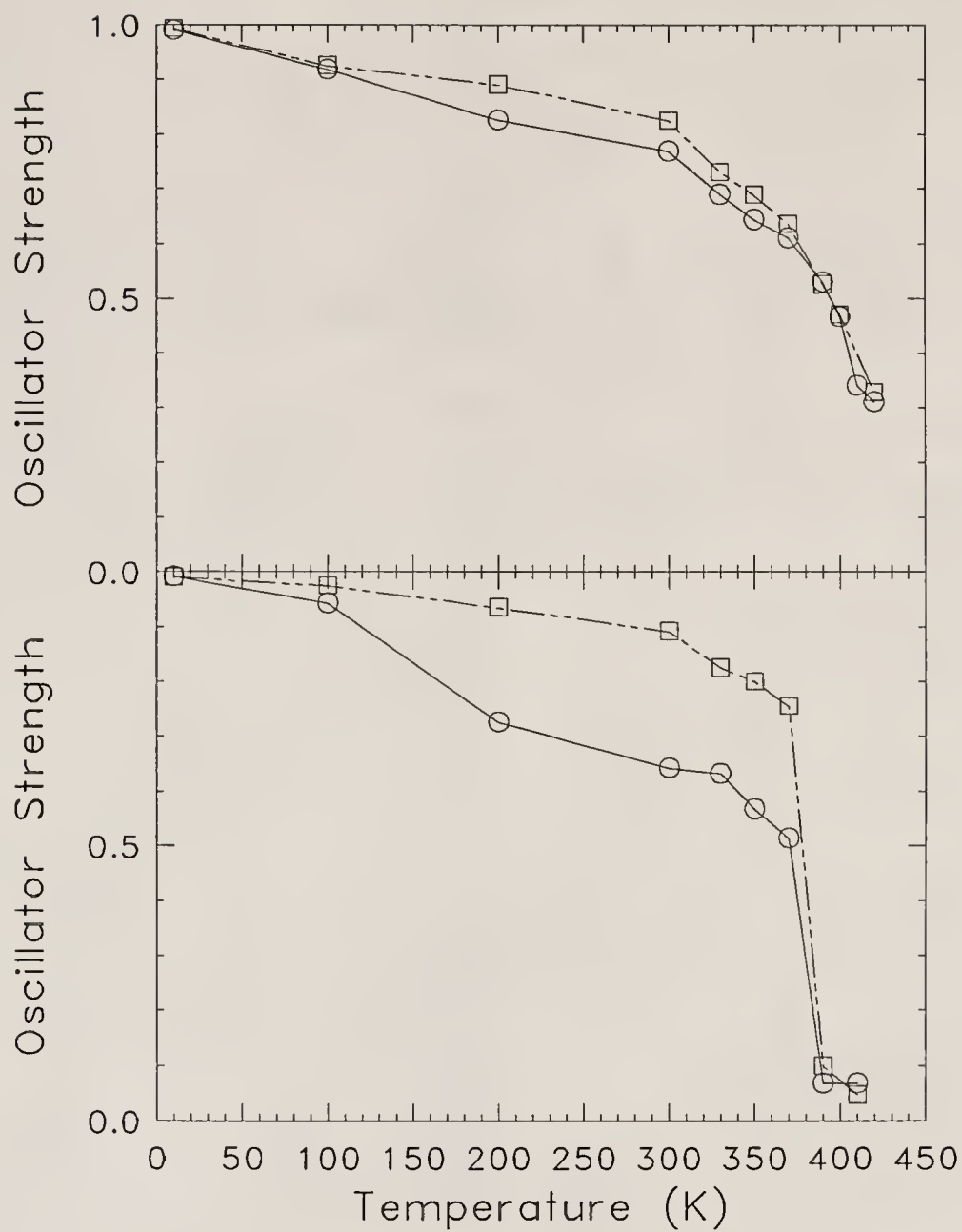
Fig. 45. Upper panel: Integrated oscillator strength *vs.* temperature for K-TCNQ. Lower panel: Integrated oscillator strength *vs.* temperature for Rb-TCNQ. Solid line: 340 cm^{-1} mode; Dashed line: 720 cm^{-1} mode.
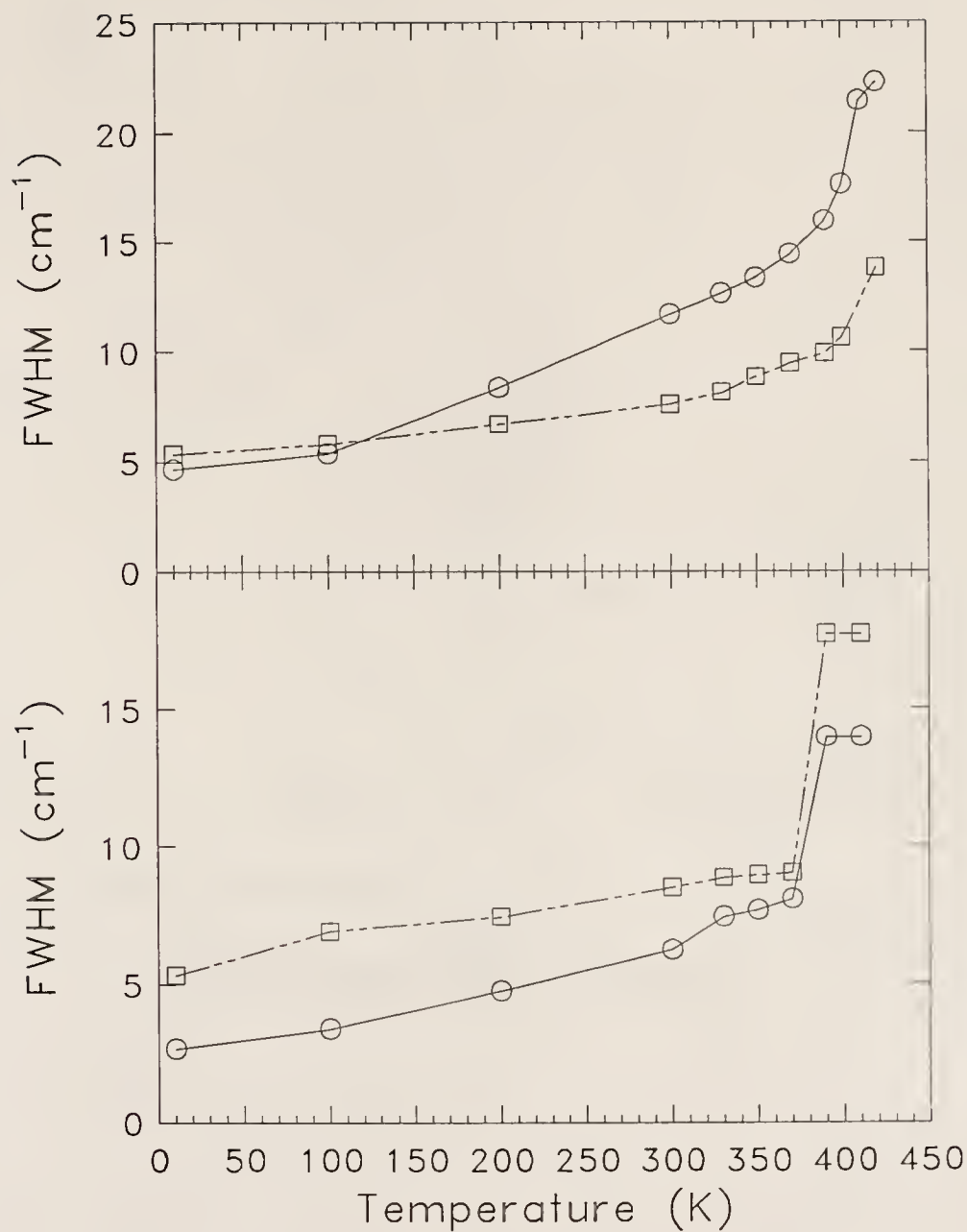
Fig. 46. Upper panel: Line width *vs.* temperature for K-TCNQ. Lower panel: Line width *vs.* temperature for Rb-TCNQ. Solid line: 340 cm^{-1} mode; Dashed line: 720 cm^{-1} mode.

CHAPTER VII
RESULTS AND DISCUSSION—LUMINESCENT POLYMERS

Phenylene Based Polymers

Optical Absorption and Steady State Photo-Luminescence

The optical absorption and steady state photo-emission properties of several potential electro-luminescent phenylene based polymers containing discrete emitter units were determined at room temperature. These measurements allow a systematic investigation of the photo-physical properties of polymers containing electronically isolated emitter units with varying degrees of conjugation. In addition, there is some evidence[31,32,33] that the photo- and electro-luminescence spectra are nearly identical, indicating that the radiative recombination process is similar as well. Thus, we can study the characteristics of the decay process via photo-luminescence and expect the results to be relevant to analogous processes in electro-luminescence. Such characterization is also a necessary preliminary for the investigation of electro-luminescence, as it allows us to screen out less promising candidate materials.

The optical absorption and photo-emission spectra of the PMP cast film are displayed in Fig. 47. In this material, the onset of the $(\pi.\pi^*)$ semiconducting band gap absorption is at ≈ 320 nm (3.87 eV), while the absorption maximum is at ≈ 262 nm (4.74 eV). We estimate that the absorption coefficient is on the order of 10^4 cm^{-1}. The steady state photo-luminescence spectra of PMP is relatively narrow; the band is centered at ≈ 397 nm (3.12 eV). This film is a strong blue-violet emitter when irradiated with an ultraviolet lamp as well. The Stokes shift of the film, calculated as the difference between the absorption and photo-luminescence maxima, is 1.62

eV. Similar results have been obtained in solution[148] and will be discussed in a later section.

The solid state absorption and photo-luminescence spectra of PQP (Fig. 3) have been measured by Pomerantz et al.[149] They report the absorbance maximum to be at $\approx$ 300 nm (4.13 eV) and the emission maximum to be at $\approx$ 401 nm (3.09 eV). Thus, the PQP film exhibits a Stokes shift of 1.04 eV. Nearly identical results were obtained in solution.

The narrow emission spectrum in PMP and PQP, combined with the absence of self-absorption in these materials, suggests that radiative decay is occurring from an impurity level, rather than an intrinsic band state.[56] Additional evidence for this conclusion is given by the fact that with increasing excitation intensity, the emission intensity increases without a change in the shape or center resonance frequency of the spectrum.[56] As previously discussed, the electronic and optical properties of many polymers, most notably doped PPP, are well accounted for by the creation of polaron and bipolaron defects. This has lead many researchers to conclude that radiative light emission from polymers with a non-degenerate ground state is the result of transition between two polaron defect states.[130,60,33,138,62,63,61,193] A similar conclusion seems reasonable for our materials, although it is important to emphasize that PMP and PQP can form only localized polaron defects.

A comparison of our absorbance and photo-luminescence data on PMP and PQP with previous results on the well-studied PPP model compound is of great interest. There have been numerous reports of various methods for the synthesis of PPP and the resulting electronic properties in the literature. Two seemingly relevant reports will be discussed here; both are by the Graz group. In PPP prepared by a precursor method, the Graz group report a band gap of $\approx$ 426 nm (2.9 eV), and an absorption maximum of $\approx$ 333 nm (3.65 eV).[137] In a later report using the same precursor

method, they observe the emission spectrum centered at $\approx$ 488 nm (2.54 eV).[33] Thus, PPP as prepared by the precursor method has a Stokes shift of 1.1 eV.[33] For crystalline samples of PPP, the same group reports a maximum absorbance of 360 nm (3.44 eV), and a Stokes shift of 1.67 eV. It is suggested that variations in the position of the absorption and emission spectra are due to differences in the chain length. Both sets of absorption data compare well to band structure calculations by Brédas et al.[194]

The electronic spectra of PMP and PQP are very similar in character to the data for PPP reported by the Graz group. However, in our samples, reduction of the electronic conjugation along the chain resulted in a wider band gap and an emission spectra that is blue-shifted by a corresponding amount. These spectral shifts occurred without a significant change in the shape of the spectra.

The Stokes shifts reported for these phenylene materials are a similar order of magnitude as well: $\approx$ 1.62 eV for PMP and $\approx$ 1.04 eV for PQP, compared with $\approx$ 1.1/1.69 eV for the two different forms of PPP. Using this data, it is possible to obtain the polaron energy level within the gap, which is commonly calculated as half the Stokes shift.[60,130,139] This places the two polaron levels slightly more than 0.5 eV (0.81, 0.50, and 0.55/0.83 eV for PMP, PQP and PPP, respectively) away from the band edges. This energy for the PPP system should not be construed as an invariant material property because the separation between the band and the defect level is likely to be influenced by the effective conjugation length of the chain as well as other factors pertaining to the method of synthesis.[137,138] However, in the case of PMP and PQP, the conjugation length is invariant, leaving only impurity effects to cause small differences in the position of the polaron band within the gap.

With the exception of PPV, the size of the Stokes shift is also similar to that in other polaron based polymers.[130,60] It has been suggested by a number of researchers

that this large Stokes shift is related to an nonradiative energy transfer which distorts the quasi-one-dimensional lattice, resulting in the formation of polaron and bipolaron charge defects. Despite the strong chemical similarity, the transport properties of PPP and the materials in this study are quite different: while the bipolaron defect can travel along the chain due to good long range conjugation in PPP, the meta-linkages in PMP and the bulky side groups of PQP which twist the chain out of a planar configuration, resulting in a localized defect (Fig. 16). Consequently, the qualitative agreement between the size of the Stokes shift in these phenylene based materials is particularly striking, as it suggests that the degree and mechanism of lattice relaxation is not affected by the ability of the bipolaron charge defect to travel along the chain.

Electro-luminescence

For the electro-luminescence measurements, we concentrated upon the two materials whose photo-physical properties have been described in detail above: poly-m-phenylene (PMP) and the poly-quarterphenylene (PQP). A plot of current vs voltage is displayed in Fig. 48 for the PMP based diode. A plot of electro-luminescent intensity vs voltage is shown in Fig. 49 for PQP.

For the PMP based diode (Fig. 48), we observe a strongly non-linear current-voltage relationship, with the threshold for charge injection at $\approx$ 6 V. Weak light emission (bluish-white) was observed at a current of approximately 0.6 mA. For the PQP based diode (Fig. 49), substantial charge injection begins near 9 V, after which the emitted light intensity increases sharply. It is interesting to note that for both the PMP and PQP diodes, the injection voltage is substantially lower than that which has been reported for devices based upon fully conjugated polymers.

It should be noted here that although these curves are representative descriptions of the charge injection process in the diodes, the reproducibility is not very good due

to processing difficulties—especially with the thin film preparation. Thus, the data in Fig. 48 and Fig. 49 should be considered preliminary.

Due to the device processing difficulties as well as time limitations, we have been unable to obtain the electro-luminescent spectra of these devices. However, a weak blue-white emission was observed from a PMP based device by the author. In addition, there is evidence from measurements on various other polymer based diode devices[31,32,33] that the photo- and electro-luminescence spectra are nearly indistinguishable. Thus, based upon our steady state photo-luminescence spectra, it is likely that both PMP and PQP based diode devices emit blue light. However, some caution must be advised before extrapolating these preliminary findings and similarities with other materials to a conclusion.

Exciton Lifetimes and Luminescent Efficiencies

Photo-luminescence lifetime measurements on PMP and PQP, measured at the steady state photo-luminescence maximum, show very short exciton decay times, on the order of nanoseconds. In both materials, the decay profile was fit with two first order rate equations. These fits gave values of 0.657±0.008 and 2.664±0.073 nsec, and 0.159±0.004 and 3.358±0.119 nsec, for PMP and PQP lifetimes, respectively. In both materials, the primary decay takes place at the shorter time, with the longer lifetime contributing less than 0.02% to the total decay. These values are in reasonable agreement with those obtained for PPV, modified PPV systems, and PPP, which displayed both nsec and psec components for the polaron exciton lifetime.[60,130,131] Thus, confinement of the exciton in discrete emitter segments does not seem to effect its lifetime in these materials.

Electro-luminescent efficiencies for PPV, modified PPV, and PPP based diode devices have been reported to be small, ranging from 0.01–1.0%.[31,32,33] Although we do not have estimates of the electro-luminescent efficiencies for PMP and PQP,

we expect similar values for these materials. The weak light emission indicates that the principal recombination mechanism is nonradiative. Further evidence for this conclusion is given by the short exciton lifetimes.

Structure-Property Relations: Phenylene Based Materials

The absorption and photo-luminescence spectra of several phenylene based polymers containing different numbers of conjugated units in the emitter group were studied to ascertain the effect of structural modification on the electronic properties of these materials. The chemical structures of the polymers are shown in Fig. 2.

The solid state absorption characteristics of the phenylene based polymers are similar to that displayed in Fig. 47. With increasing emitter unit conjugation (from two to five), we observe a red shift of the band gap by $\approx$ 0.5 eV and a decrease in the optical absorbance maxima of 0.4 eV. Analogous behavior is observed in several fully conjugated materials upon increasing the oligomer size from a few units to the extended polymer.[134,132,195] For the polymers with three phenylenes in the emitter unit, the absorption coefficient of the (π,π^*) transition is quite low compared to the others.

The steady-state photo-luminescence properties of the various phenylene materials in Fig. 2 provide dramatic evidence for the important role of relaxational effects in the light emission characteristics of these materials. Each of these materials displays a photo-luminescence maximum in the blue regime, near 400 nm. With increasing conjugation of the emitter unit, the width of the emission spectrum increased slightly on the low energy side of the peak; no difference was observed on the high energy side of the emission spectra. It is worth noting here that the photo-luminescence of polymer 3 was exceptionally strong.

The absorbance and photo-luminescence spectra of these same phenylene based materials in solution (tetrahydrofuran) have been reported elsewhere.[148] With in-

creasing conjugation, both the absorption and emission maxima display a slight red shift.

Figure 50 displays the solution and solid state zero-phonon transitions of the optical absorption and steady-state photo-emission of this series of phenylene based polymers as a function of $\frac{1}{m}$, where m is a measure of the conjugation of the discrete emitter unit. Here, m refers explicitly to the number of phenyl groups which are electronically attached in the emitter segment.

From the data in Fig. 50, we observe a red shift of the absorption maxima with increasing conjugation of the emitter unit; this effect is more pronounced in the solid film. Several studies (on fully conjugated polymers such PPV and modified systems, as well as phenylene oligomers) have noted similar behavior with increasing conjugation.[134,132,195,137] Consequently, we conclude that the trend in our materials is a result of reduced electronic isolation. In addition, the absorption maxima as obtained in solution is blue-shifted from that of the solid film. It is likely that this is due to the effect of ring torsions, which twist the chain out of planarity, and thereby reduce the conjugation within the emitter unit.[134,195]

In the solid film, the photo-luminescence maximum is fairly insensitive to changes in emitter unit conjugation, while in solution, a very slight red shifting is observed with increasing conjugation. The absence of a strong effect of emitter unit conjugation on the position of the emission maxima for these materials suggests that the charge defect levels (between which, emission occurs) retain a relatively constant separation within the gap despite changes in emitter center conjugation, which more strongly affect the size of the band gap. A larger relaxation may be expected in solution (as compared with a solid sample) due to an increased number of conformational degrees of freedom. The role of torsional twisting is an especially important and well documented pathway of relaxation.[60] In addition, it is reasonable to anticipate

that an increased number of vibrational degrees of freedom in the more complicated materials will provide additional pathways for nonradiative decay to take place in solution, and to a lesser extent in a solid film.

We find that the Stokes shift decreases with increasing emitter unit conjugation, both in solution and in the solid film. Such a trend has also been reported in fully conjugated oligomers, such as PPV, where the Stokes shift reaches a minimum for a fully conjugated, infinite chain, polymer.[134]

Together, the absorption and emission measurements reported here establish a fundamental link between the structure and conjugation of the discrete emitting center and the related electronic properties. It would be useful to correlate the conjugation of the emitter unit with emission lifetimes and efficiencies as well.

(2-Thienyl)Phenylene Based Polymers

Some preliminary work has been done on the 1,4-bis(2-thienyl)phenylene (PBTP) polymers (Fig. 4). The optical absorption and steady state photo-luminescence spectra for two PBTP based polymers with hexyl and dodecyloxy side chains 2,5-substituted on the phenylene ring are shown in Fig. 51 and Fig. 52, respectively. The absorption maximum for the material with the hexyl side group is rather broad and centered at $\approx$ 312.5 nm (3.97 eV), whereas α_{max} for the polymer with the more electron-donating dodecyloxy side group is more narrow and at $\approx$ 488 nm (2.54 eV). The absorption edge is much sharper here, as well. The electron-donating and withdrawing properties of side chains have been documented to influence the gap in this well known manner for many materials.[139]

The steady state photo-luminescence spectrum of the the (2-thienyl)phenylene material with the hexyl side chains has a symmetric shape and is centered at $\approx$ 545 nm (2.27 eV). The large Stokes shift (1.7 eV) suggests that a large geometry

relaxation is required before emission from the excited state. In contrast, the steady state emission spectrum of the PBTP material with dodecyloxy side chains had a strongly asymmetrical shape, with maxima at $\approx$ 596 and 650 nm (2.08 and 1.91 eV). This structure likely arises from transitions from the excited electronic state to both the ground and first excited vibrational levels in the ground electronic surface. The energy splitting between these peaks is 1394 cm^{-1}, consistent with the idea of exciton coupling to a C=C stretching vibration within the phenylene ring.[133,135] The lack of mirror image similarity indicates that there is a large geometry difference in the excited state, but the small Stokes shift (0.46 eV) suggests that not much relaxation is necessary before light emission. Although an absolute value of the photo-luminescence efficiency is not known, the material with the electron-withdrawing side chain (hexyl) had noticeably reduced photo-luminescence intensity compared with the dodecyloxy material.

The unsubstituted PBTP repeat unit can probably support a neutral bipolaron exciton charge defect; as such, it is a potential electro-luminescent polymer. While the hexyl side chains act to twist the chain out of the plane, preventing long range conjugation and reducing bipolaron mobility, the dodecyloxy side chains allow the main-chain to be quasi-planar. In this way, discrete emitter units can be engineered for PBTP based materials as well, allowing a more general test of the idea of electronically isolated emitter centers. With this idea in mind, electro-luminescence measurements will be performed on these two compounds in the near future. Exciton lifetime measurements would be useful as well, especially for the dodecyloxy material.

Mechanism of Charge Injection in Electro-Luminescence

Recently, two groups have attempted to address questions pertaining to charge injection. Braun et al have recently proposed that population of the upper polaron state may occur via a tunneling mechanism.[32] The tunneling mechanism of charge

injection can contribute to the population of polaron level only if wavelength of the injected electron is comparable to width of the potential barrier. In the case of a large or wide barrier, the electron has a very small probability of tunneling through, making this mechanism less likely to contribute to populating the excited state.

In the Schottky diode picture, the fact that polymer based diodes need a high field before significant charge injection occurs suggests that the potential barrier is wide. However, a measurement of the PPP/Al barrier size indicate that this is not so.[33] Grem et al[33] report that the Schottky barrier height between PPP and Al contacts and found it to be only 0.4 eV. They conclude that such a small barrier can not be responsible for the 10 V injection threshold observed in PPP based diode devices. Consequently, the authors suggest that the device operates without the existence of a Schottky barrier, but that the high field generated within the device is responsible for the carrier injection.[33]

It has been observed in these and other conjugated polymers that light emission commonly occurs in the non-linear region of the voltage-current curve where small increases in the voltage result in large increases in the current.[31,32,33] This observation has also suggested to us that carrier generation may not be purely due to charge injection phenomena, and that electric field effects may be important in these diode devices. This is in contrast to inorganic based light emitting diodes, which are low field devices; here, population of the impurity band proceeds by carrier injection or in some cases, tunneling.[56] It would be an interesting and timely project to work out the electric field dependence of the tunnelling process in detail. Very high field characteristics would be of special interest.

The mechanism which places electrons in the defect state may be very different from diode devices based upon other materials, and is unlikely to be a tunneling process (through a Schottky barrier) unless the electric field is strongly perturbing

the shape of the barrier as well. We suggest that one of the Schottky diode breakdown mechanisms is in effect in the non-linear regime.

Finally, Braun et al[32] have also reported that for PPV and modified systems, thermal activation plays no role in the carrier injection or emission process. However, Ohmori et al[34] report increased photo- and electro-luminescence intensity at elevated temperature. Whether thermal processes play a role in the light emission of polymers with discrete emitter units should be investigated with temperature dependent photo- and electro-luminescence measurements on a variety of these materials.

<p style="text-align:center">Future Work</p>

Polymers containing discrete emitter units are a new class of potential light emitting materials that offer many interesting aspects of study. The results presented here demonstrate that although the photo- and electro-luminescence may arise from the radiative recombination of the bipolaron exciton as previously suggested, the luminescence does not arise from the extended nature of the conjugated π electron system along the polymer backbone and that such an extended π system is not a necessary preliminary for achieving light emission. In the future, it will be of general interest to develop qualitative ideas for what aspects of the structure result in photo- as well as electro-luminescence in these materials. By examining the effect of the chemical structure on the photo- and electro- luminescence properties, we can also ascertain the effect of the chemical structure on frequency of emitted light, the degree of relaxation, ease of polaron-bipolaron formation, and likelihood of radiative exciton recombination, with the goal of developing a better understanding of the mechanism of electro-luminescence.
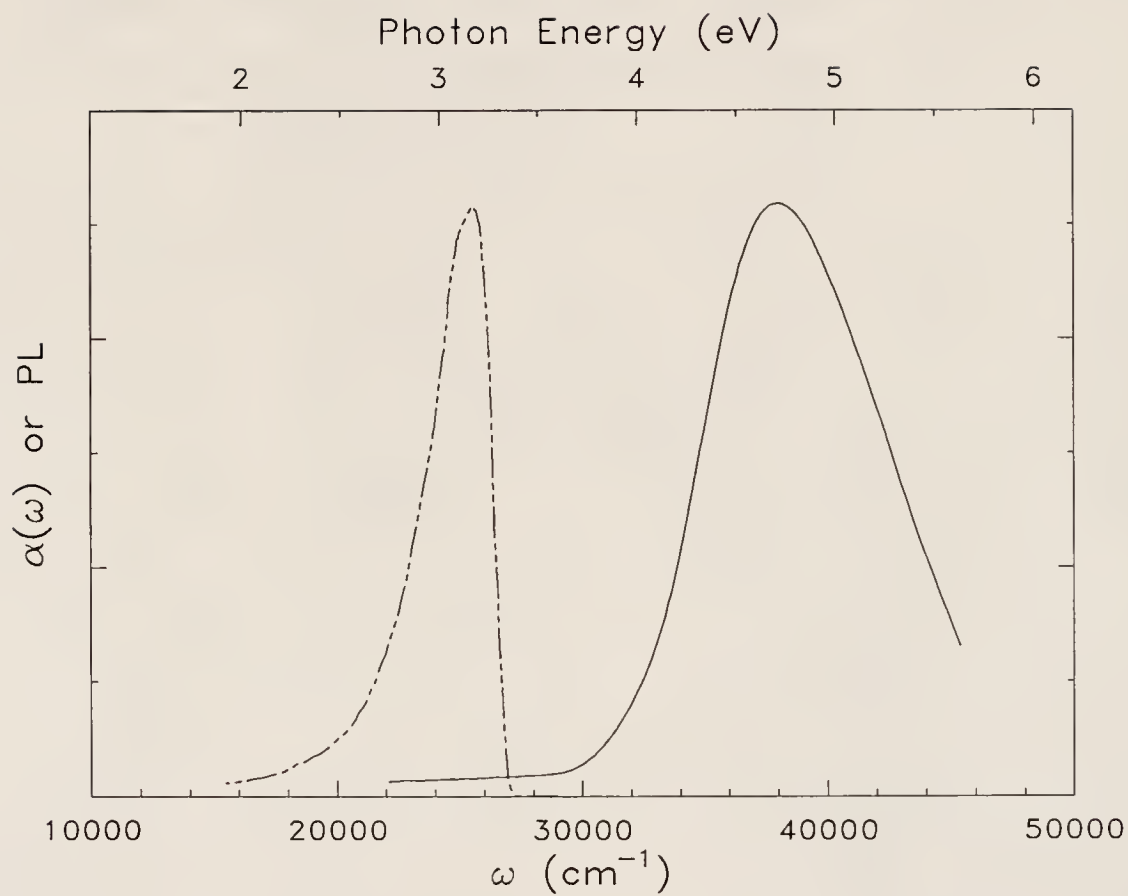
Fig. 47. Optical absorption and photo-luminescence spectra of poly-m-phenylene.

Fig. 48. Current-Voltage characteristics of the PMP based diode device.

Fig. 49. EL Intensity-Voltage characteristics of PQP based diode device.

Fig. 50. Optical absorption and steady state photo-luminescence maxima for phenylene polymers with various conjugation of the discrete emitter unit.

Fig. 51. PBTP based polymer with hexyl side groups.

Fig. 52. PBTP based polymer with dodecyloxy side groups.

CHAPTER VIII
SUMMARY AND CONCLUSIONS

Quasi-One Dimensional Organic Charge Transfer Salts

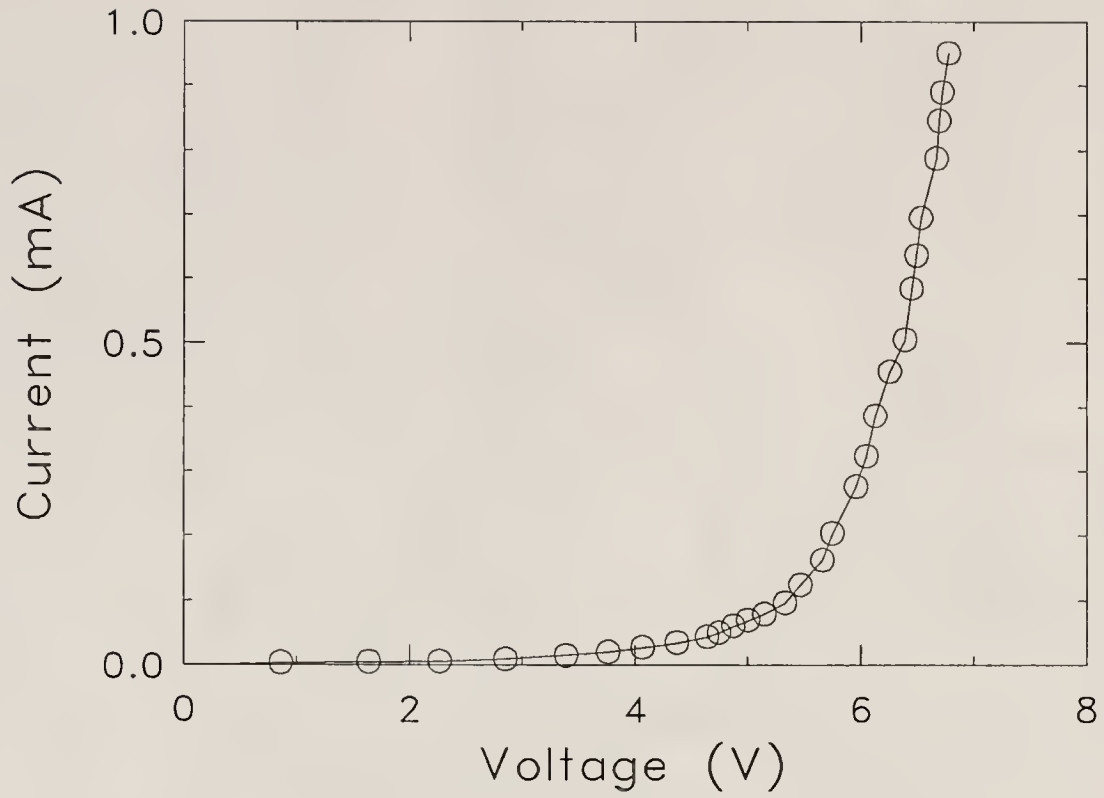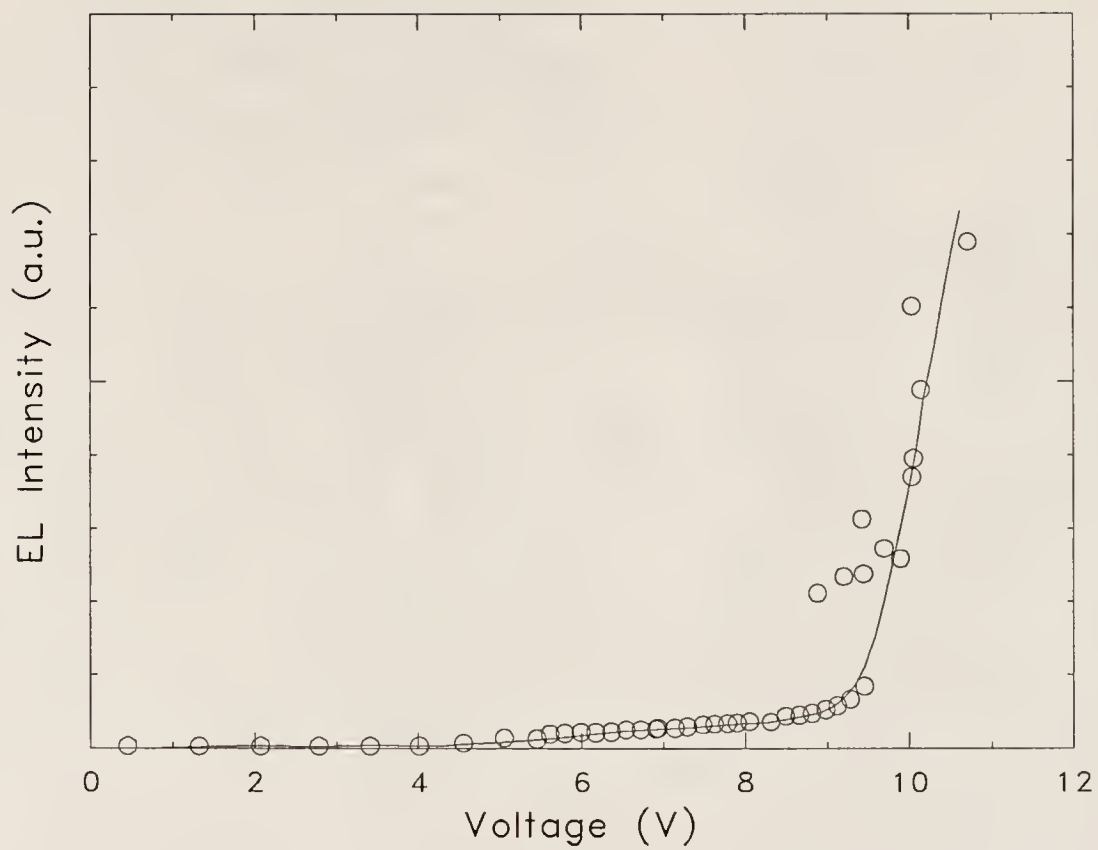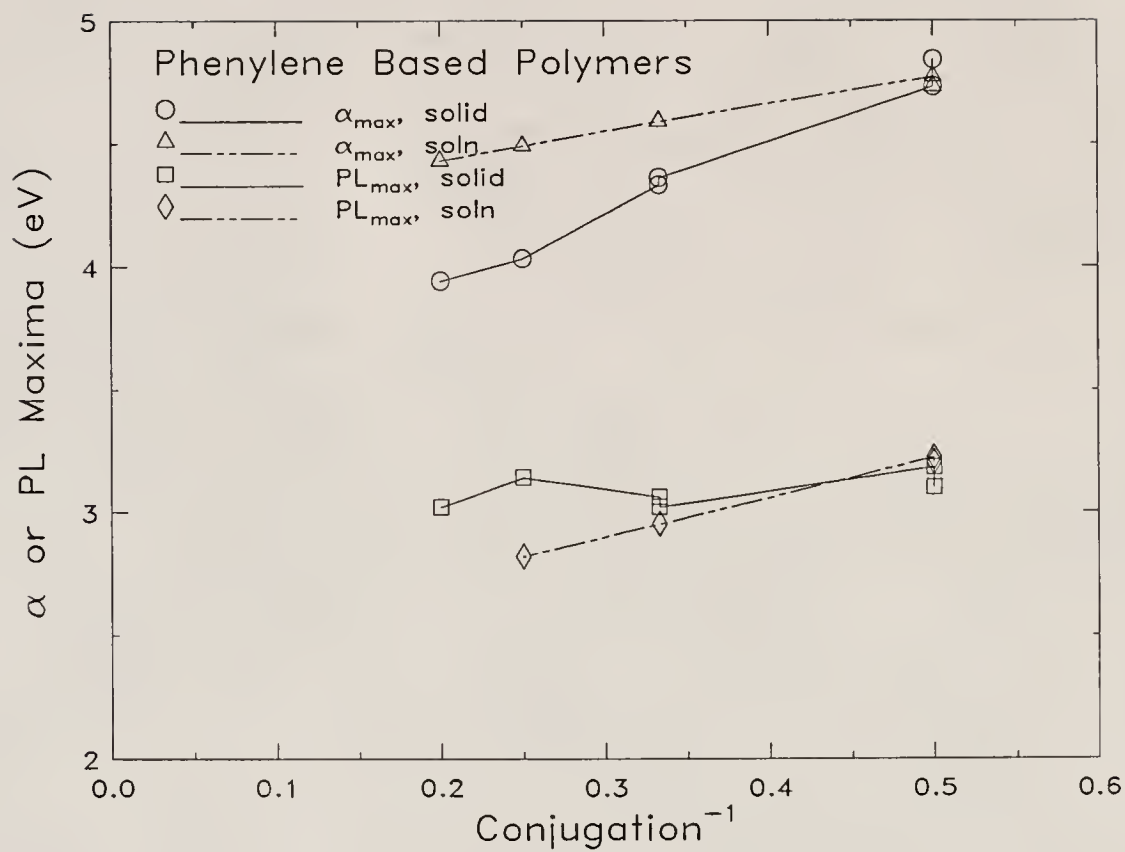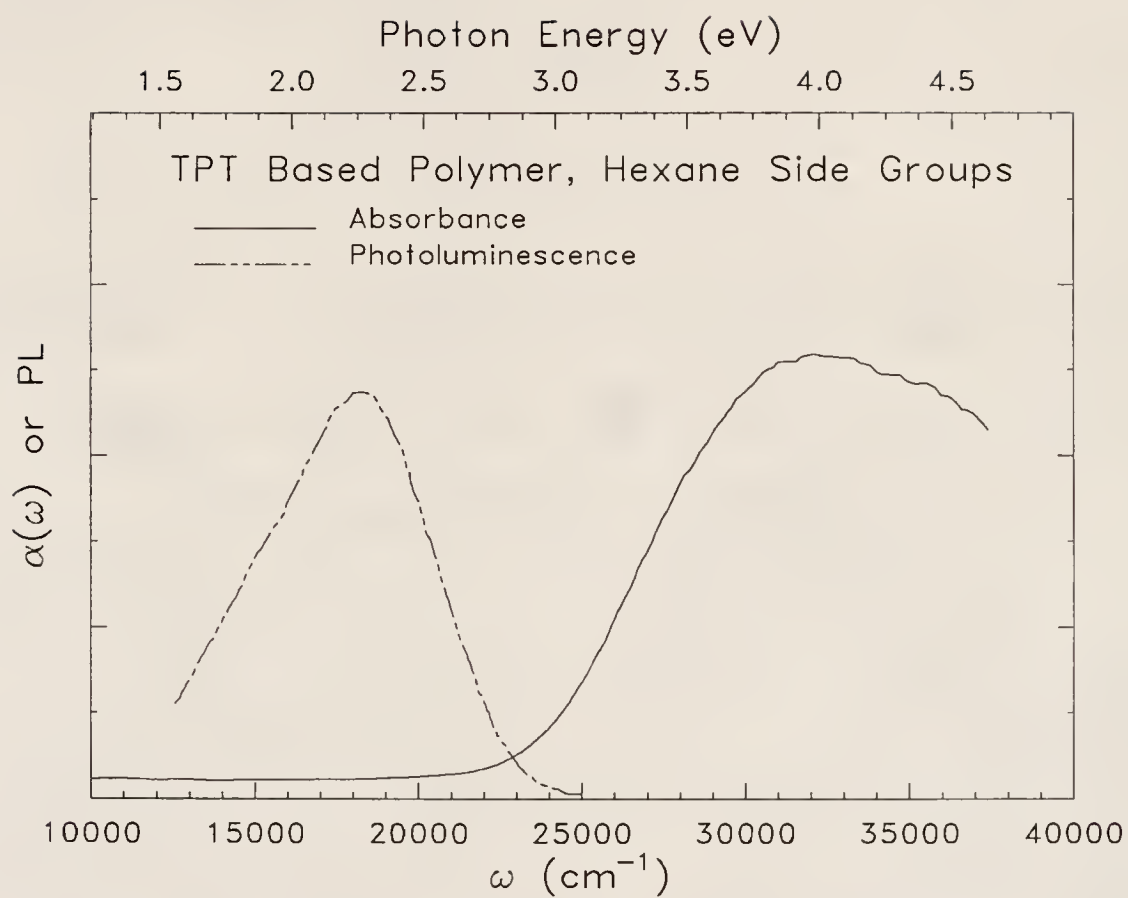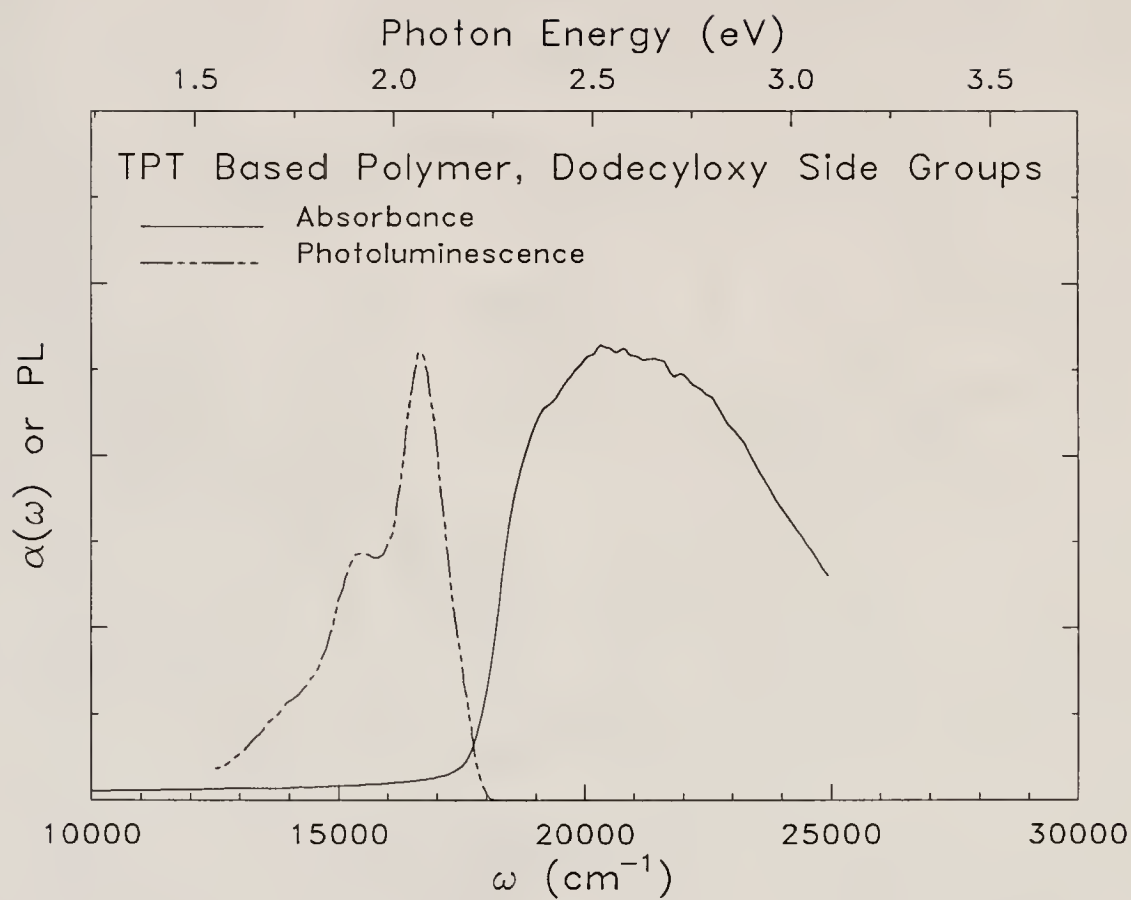I have presented a spectral investigation of two quarter-filled semiconducting organic charge transfer salts, NPrQn(TCNQ)$_2$ and DMTM(TCNQ)$_2$, and two half-filled salts, K-TCNQ and Rb-TCNQ, at various temperatures both above and below T_c in an effort to understand the unusual electrical transport properties in the high- and low-temperature phases and gain insight into the mechanism and characteristics of the unusual structural phase transitions in these two materials.

For NPrQn(TCNQ)$_2$, the high-temperature phase spectra are typical of other quarter-filled 1:2 semiconducting TCNQ charge transfer salts, with a uniform charge distribution on the tetramer above T_c. The broad low energy charge transfer band is attributed to three overlapping excitations. In the low-temperature phase, the low energy charge transfer band is resolved into two separate bands, separated by a minimum in the frequency dependent conductivity. The bands have been attributed to intra- and inter- tetramer charge transfer. The increased oscillator strength of the low energy charge transfer band is evidence of an increased intra-tetramer transfer integral. The doublet fine structure of the phonon modes is indicative of an uneven (and more localized) charge distribution within the tetramer.

Spectrally, NPrQn(TCNQ)$_2$ is a semiconductor in the high-temperature phase. We attribute the weakly metallic transport properties above T_c to the uniform charge distribution within the tetramer and the high degree of overlap between the intra- and

inter- tetramer charge transfer bands. NPrQn(TCNQ)$_2$ is a semiconductor in the low-temperature regime as well, but transport is hindered by charge localization which may reduce the overlap of the low energy charge transfer bands. Recent calculations[52] have suggested that the high-temperature 'metal-like' transport properties are related to the large effective cation potential, and the sharp decrease in the conductivity at T_c is due to an increasing Peierls contribution to the gap with decreasing temperature.

For the DMTM(TCNQ)$_2$ crystal, we have the following conclusions. For light polarized close to the TCNQ stacking direction on the (010) face, the infrared spectra is characteristic of other quarter-filled, dimerized, 1:2 semiconducting TCNQ charge transfer salts, with two charge transfer excitations and prominent A_g vibrational structure. The isolated dimer model of Rice et al.[22] (presented here) and the twofold-commensurate charge density wave model by Bozio et al.[25] were applied to DMTM(TCNQ)$_2$ both above and below T_c. The isolated dimer model gave a reasonable fit to the data in the high temperature phase. However, it is shown elsewhere[8] that the latter model was superior in reproducing the lineshapes below 2Δ but required modification to agree with the high frequency results. Neither model produced completely satisfactory results below T_c. The unperturbed A_g phonon frequencies and the EMV coupling constants were fitted and found to be in good agreement with ab initio calculations and other experimental results in similar TCNQ salts. The electronic spectra, most notably the U band, showed an unusual temperature dependence, and may have important implications for charge transport in the TCNQ stacking direction.

We have also investigated the structural phase transition of DMTM(TCNQ)$_2$ in light of the crystal field distortion theory by Visser et al.[86] For light polarized close to the b crystallographic axis on the (110) crystal face, the spectral data is, overall, not in good agreement with the band structure (Fig. 14) proposed by the aforementioned

authors. The agreement is good in the high-temperature phase, although the origin of the splitting near 10000 cm^{-1} is unclear. However, below T_c, several expected low energy charge transfer bands are absent, most notably the low energy excitation at 430 cm^{-1}. In the absence of spectral evidence for low energy excitation at 430 cm^{-1}, the activation energy for inter-chain transport would be ≈ 0.25 eV both above and below T_c. Consequently, we do not find conclusive spectral evidence that the unusual transport properties of semiconducting DMTM(TCNQ)$_2$ can be explained in terms of low energy inter-chain charge transfer.

Finally, I report the polarized far infrared reflectance spectrum of semiconducting potassium- and rubidium-tetracyanoquinodimethane (K-TCNQ and Rb-TCNQ) at temperatures above and below T_c, with the goal of investigating the role of cation substitution on the structural phase transition in these two closely related compounds. As in the quarter-filled salts, the cations in these materials play an important role in the phase transition, primarily influencing the lattice distortion.

The infrared vibrational features are divided between intra-molecular and inter-molecular modes. We tabulate the (intra-molecular) unperturbed A_g resonance frequencies; they are in good agreement with each other as well as previous measurements and calculations. Other intra-molecular modes of non-A_g symmetry are also tabulated and symmetry designations are assigned. Tentative assignments are made to the low energy lattice modes.

The electron-phonon coupling induced modes display pronounced temperature dependence. In the low-temperature phase of both materials, the spectra polarized along the TCNQ dimer axis display strong vibrational features of A_g origin, characteristic of many weakly conducting dimerized TCNQ salts. These features change gradually with temperature in the potassium sample, whereas in the rubidium sample, little contrast was observed. Above T_c, the far infrared A_g vibrational features in

K-TCNQ are reduced, but not disappeared; they continue to change gradually above T_c. In contrast, the A_g vibrational modes in Rb-TCNQ decrease abruptly (and almost completely) at T_c; no temperature dependence of the far-infrared spectra observed in the high-temperature phase. These observations suggest that while the phase transition is strongly first-order for Rb-TCNQ, it is closer to second-order in K-TCNQ, and that it is modulated almost entirely by the cation potential.

While the electronic properties in these materials are one-dimensional, the lattice properties are multi-dimensional, with librational modes in both of the polarizations studied. A strong red shifting and broadening of the far-infrared lattice modes is observed both K- and Rb-TCNQ with increasing temperature. Librational modes were assigned based upon this temperature dependence.

Luminescent Polymers

The luminescent polymer work detailed in this dissertation was motivated by several goals. The first was to characterize the absorption and emission properties of several potential electro-luminescent materials. Such characterization is a necessary preliminary for the investigation of electro-luminescence. In addition, these measurements allowed us to study the relationship between chemical structure and the absorption and emission properties.

Not surprisingly, the large semiconducting band gap is essential to the subsequent emission of visible light. All of the polymers studied here have an especially large (π,π^*) band gap absorption due to the electronic isolation of the emitter units in the chain backbone. This is particularly true of the phenylene based materials. This broken conjugation has been achieved using *meta* linkages or with the aid or bulky side groups, which act to twist the chain out of a planar configuration. The electron-donating ability of side chain is also critical in determining the location (π,π^*) band gap absorption, as it influences the overall conjugation and electron density within

the chain. Although an optical or near ultra violet band gap is very important, large Stokes shifts were observed in several compounds, suggesting that the vibrational and configurational relaxation plays a more important role in determining the emission frequency than the size of the band gap.

The phenylene based set of materials in Fig. 2 allowed the systematic examination of the effective conjugation length of the isolated emitter unit on the optical absorption and emission properties. Both in the solid state and in solution, the energy of the optical absorption maxima was observed to decrease with increasing emitter unit conjugation. In addition, the solution spectra were blue shifted from those obtained on solid films. Such behavior has been reported elsewhere for fully conjugated systems, and has been attributed to effects of ring torsion.[134] In contrast, the photo-luminescence maxima were relatively independent of conjugation, red shifting by approximately 40 nm in solution, and only slightly in the solid state. These observations suggest that relaxation effects become more important with increasing conjugation, especially in solution where the increased number of vibrational and conformational degrees of freedom likely result in a larger number of nonradiative decay pathways. Based upon these steady state photo-luminescence measurements, we also concluded that many of the phenylene based materials are potentially blue electro-luminescent emitters.

The measurement of electro-luminescence was of particular interest. We concentrated our efforts on poly-m-phenylene (PMP) and polyquarterphenylene (PQP). The current voltage characteristics of these diode devices are similar to those based upon PPV and PPP.[31,33] Both materials displayed the typical rectifying behavior, although the threshold for charge injection, ≈ 6.5 and 9 V, respectively, is substantially less that that reported for PPP or PPV diode devices.[31,32,33] In the case of PMP, bluish-white emission was observed from the diode. In the case of PQP, visible light

was detected by the photomultiplier tube; there was no visual verification. These preliminary results are very encouraging, as they suggest that a wide variety of polymers with discrete emitter centers may be usefully employed as electro-luminescent materials.

It was a final goal of this work was to develop a better understanding of the mechanism for electro-luminescence in polymeric materials. To this end, we have studied the luminescent properties of a variety of common semiconducting polymers whose chemical structure caused electronic localization of the defect was achieved, resulting in discrete emitter centers linked together. We find that although the ability to support bipolaron charge defects is essential to radiative recombination of singlet bipolaron excitons after carrier injection, it is unnecessary for the charged defect to move along the chain in order to achieve radiative recombination. Thus, PMP and PQP may be the first two members of a larger class of wide band gap polymers with discrete emitter units which display visible EL.

We believe that we have demonstrated that electro-luminescence in polymers is not an isolated or rare phenomena, confined only to conducting polymers such as PPV or PPP, and that within certain limitations of chemical structure, photo- and electro-luminescence are intrinsic properties of many conjugated organic polymers. In fact, electro-luminescence is likely to be a common feature of many wide band gap semiconducting polymers.

The future of electro-luminescent polymers promises to be as exciting as the conducting polymer field has been in the past decade. Therefore, there are many directions in which work (specific to my projects) could proceed from here. Electro-luminescence measurements should be carried out on the (2-thienyl)phenylene based polymers, as well as the remainder of the phenylene based materials discussed in this document. Electro-luminescent efficiencies and spectra should be obtained. In

addition, other materials with discrete emitter units should be tested for electro-luminescence, with the goal of developing structure-property relationships from a large data base of materials. An understanding of these aspects would make tunable polymer based diode devices a reality. In addition, there are fundamental mechanistic questions which remain unanswered at this early stage which have important implications for device performance. For example, a better understanding of the mechanisms of nonradiative decay could lead to the design of materials with these pathways inhibited. It would be interesting to compare the lifetime and mobility of the bipolaron exciton in a structure such as PPP with that in a material with discrete emitter units, such as PMP. Correlated with the electro-luminescent efficiency, such a measurement would conclusively demonstrate whether localization of the charged defect results in reduced nonradiative decay. The end result of these mechanistic investigations should result in improved device efficiencies. Finally, better processing techniques, electron transport layers and alternate electrode materials promise to result in more efficient carrier injection and thus, more efficient light emission. These materials promise to have a wide variety of electro-optic applications.

REFERENCES

1. L.R. Melby, R.J. Harder, W.R. Hertler, W. Mahler, R.E. Benson, and W.E. Mochel, *J. Am. Chem. Soc.* **82**, 6408 (1960).

2. L.R. Melby, R.J. Harder, W.R. Hertler, W. Mahler, R.E. Benson, and W.E. Mochel, *J. Am. Chem. Soc.* **84**, 3374 (1962).

3. V.M. Yartsev, *Phys. Stat. Sol.* **B149**, 157 (1988).

4. C.S. Jacobsen in *Semiconductors and Semimetals*, Vol. 27, E.M. Conwell, ed., Ch. 5, (Academic Press, New York, 1985).

5. D.B. Tanner, K.D. Cummings, and C.S. Jacobsen, *Phys. Rev. Lett.* **47**, 597 (1981).

6. H. Okamoto, Y. Tokura, and T. Koda, *Phys. Rev. B* **36**, 3858 (1987).

7. J.L. Musfeldt, K. Kamarás and D.B. Tanner, *Phys. Rev. B* **45**, 10197 (1992).

8. J.L. Musfeldt, C.C. Homes, M. Almeida, and D.B. Tanner, *Phys. Rev. B* **46**, 8777 (1992).

9. C.C. Homes and J.E. Eldridge, *Phys. Rev. B* **42**, 9522 (1990).

10. K. Kornelsen, J.E. Eldridge, H.H. Wang, H. A. Charlier, and J.M. Williams, *Solid State Comm.* **79**, 583 (1991).

11. K. Yakushi, H. Kanbara, H. Tajima, H. Kuroda, G. Saito, and T. Mori, *Bull. Chem. Soc. Jpn.* **60**, 4251 (1987).

12. C.S. Jacobsen, J.M. Williams, and H.H. Wang, *Solid State Comm.* **54**, 937 (1985).

13. M. Erő-Gećs, L. Forro, Gy. Vancso, K. Holczer, G. Milály, and A. Jánossy, *Solid State Comm.* **32**, 845 (1979).

14. A. Jánossy, G. Mihály, L. Forro, J.R. Cooper, M. Miljak and B. Korin-Hamzic, *Mol. Cryst. Liq. Cryst.* **85**, 1623 (1982).

15. S. Oostra, J.L. de Boer, and P. Lange, *J. Phys. Colloq. C3 (Paris)* **44**, 1387 (1983).

16. M. Almeida, L. Alcacer, S. Oostra and J.L. de Boer *Synth. Met.* **19**, 445 (1987).

17. H. Terauchi, *Phys. Rev. B* **17**, 2446 (1978).

18. D.B. Tanner in *Extended Linear Chain Compounds*, Vol. 2, J.S. Miller, ed., Ch. 5, (Plenum Publishing Corp., New York, 1982).

19. V.M. Yartsev and R. Swietlik, *Reviews of Solid State Science* **4**, 69 (1990).

20. R. Bozio and C. Pecile in *Spectroscopy of Advanced Materials*, R.J.H. Clark and R.E. Hester, eds., (John Wiley, Chichester, 1990).

21. A. Girlando and C. Pecile, *Spectrochimica Acta.* **29A**, 1859 (1972).

22. M.J. Rice, V.M. Yartsev, and C.S. Jacobsen, *Phys. Rev. B* **21**, 3437 (1980).

23. V.M. Yartsev, *Phys. Stat. Sol.* **B126**, 501 (1984).

24. M.J. Rice, *Phys. Rev. Lett.* **37**, 36 (1976).

25. R. Bozio, M. Meneghetti, and C. Pecile, *Phys. Rev. B* **36**, 7795 (1987).

26. R.P. McCall, I. Hamberg, D. B. Tanner, J.S. Miller, and A.J. Epstein, *Phys. Rev. B* **39**, 7760 (1989).

27. V.M. Yartsev and C.S. Jacobsen, *Phys. Rev. B* **24**, 6167 (1981).

28. V.M. Yartsev and C.S. Jacobsen, *Phys. Status Solidi* **B145**, K149 (1988).

29. R. Świetlik and A. Graja, *J. de Physique* **44**, C3-1457 (1983).

30. J.M. Williams, H.H. Wang, T.J. Emge, U. Geiser, M.A. Beno, P.C.W. Leung, K.D. Carlson, R.J. Thorn, and A.J. Schultz in *Progress in Inorganic Chemistry, Vol. 35*, S.J. Lippard, ed., (John Wiley, New York, 1987).

31. J.H. Burroughes, D.D.C. Bradley, A.R. Brown, R.N. Marks, K. Mackay, R.H. Friend, P.L. Burns, and A.B. Holmes, *Nature* **347**, 539 (1990).

32. D. Braun and A.J. Heeger, *Appl. Phys. Lett.* **58**, 1982 (1991).

33. G. Grem, G. Leditzky, B. Ullrich, and G. Leising, *Adv. Mater.* **4**, 36 (1992).

34. Y. Ohmori, M. Uchida, K. Muro, and K. Yoshino, *Solid State Comm.* **80**, 605 (1991).

35. E.M. Conwell in *Semiconductors and Semimetals*, Vol. 27, E.M. Conwell, ed., Ch. 1, (Academic Press, New York, 1985).

36. E.M. Conwell in *Semiconductors and Semimetals*, Vol. 27, E.M. Conwell, ed., Ch. 4, (Academic Press, New York, 1985).

37. J.S. Pedersen and K. Carneiro, *Reports on Progress in Physics* **50**, 995 (1987).

38. J. Hubbard, *Phys. Rev. B* **17**, 494 (1978).

39. N.W. Ashcroft and N.D. Mermin, *Solid State Physics*, (Holt, Rinehart and Winston, Philadelphia, 1976).

40. M.J. Rice, *Solid State Comm.* **31**, 91 (1979).

41. S. Mazumdar and A.N. Bloch, *Phys. Rev. Lett.* **50**, 287 (1983).

42. R.E. Peierls, *Quantum Theory of Solids*, (Clarendon Press, Oxford, England, 1955).

43. C.B. Duke in *Extended Linear Chain Compounds*, Vol. 2, J.S. Miller, ed., Ch. 2, (Plenum Publishing Corp., New York, 1982).

44. J.W. Bray, L.V. Interrante, I.S. Jacobs, and J.C. Bonner in *Extended Linear Chain Compounds*, Vol. 3, J.S. Miller, ed., Ch. 7, (Plenum Publishing Corp., New York, 1982).

45. D.B. Tanner, J.S. Miller, M.J. Rice, and J.J. Ritsko, *Phys. Rev. B* **21**, 5835 (1980).

46. V. Fano, *Phys. Rev. B* **124**, 1866 (1961).

47. V.M. Vartsev and M.J. Rice, *Phys. Stat. Sol.* **B100**, K97 (1980).

48. V.M. Yartsev and A. Graja, *Chemical Physics* **130**, 159 (1989).

49. V.M. Yartsev and A. Graja, *Materials Science* **14**, 95 (1988).

50. M. Meneghetti and C. Pecile, *Phys. Rev. B* **42**, 1605 (1990).

51. M. Meneghetti and C. Pecile, *Phys. Rev. B* **40**, 12187 (1989).

52. C.C. Homes, J.L. Musfeldt, and D.B. Tanner, *in preparation*.

53. P. Pringsheim and M. Vogel, *Luminescence of Liquids and Solids and its Practical Applications*, (Interscience Publishers, Inc., New York, 1943).

54. G.G. Guilbault in *Practical Fluorescence: Theory, Methods, and Techniques*, (Marcel Decker, Inc., New York, 1973).

55. S.G. Schulman in *Molecular Luminescence Spectroscopy, Part 1*, in the Chemical Analysis Series, Vol. 77, P.J. Elving, J.P. Winefordner and I.M. Kolthoff, ed. (J. Wiley and Sons, New York, 1985).

56. J.I. Pankove in *Electroluminescence*, Topics is Applied Physics Series, Vol. 17, J.I. Pankove, ed., (Springer-Verlag, Berlin, 1977).

57. G.Q. Stokes, *Phil. Trans.* **142 II**, 463 (1952).

58. G.Q. Stokes, *Phil. Trans.* **143 III**, 385 (1853).

59. D. Rendell in *Fluorescence and Phosphorescence Spectroscopy*, D. Mowthorpe, ed., (J. Wiley and Sons, London, 1987).

60. R.H. Friend, D.D.C. Bradley, and P.D. Townsend, *J. Phys. D.* **20**, 1367 (1987).

61. M.J. Rice and S.R. Phillpot, *Phys. Rev. Lett.* **58**, 937 (1987).

62. U. Rauscher, H. Bassler, D.C.C. Bradley, and M. Hennecke, *Phys. Rev. B* **42**, 9830 (1990).

63. U. Rauscher, L. Schultz, A. Greiner, and H. Bassler, *J. Phys.: Condens. Matter* **1**, 9751 (1989).

64. A.J. Heeger, S. Kivelson, J.R. Schrieffer, and W-P Su, *Rev. of Mod. Phys.* **60**, 782 (1988).

65. A.S. Sendra and K.C. Smith in *Microelectronic Circuits*, 3rd Ed., (Saunders, Philadelphia, 1991).

66. M.J. Cohen, L.B. Coleman, A.F. Garito, and A.J. Heeger, *Phys. Rev. B* **10**, 1288 (1974).

67. D. Jerome, *Condensed Matter News* **1**, 11 (1992).

68. E.M. Engler, V.Y. Lee, R.R. Schumaker, S.S. Parkin, R.L. Green, and J.C. Scott, *Mol. Cryst. Liq. Cryst.* **107**, 19 (1984).

69. D. Jerome and H. Schultz, *Adv. Phys.* **31**, 299 (1982).

70. C.S. Jacobsen, D.B. Tanner, and K. Bechgaard, *Phys. Rev. B* **28**, 7019 (1983).

71. P.S. Flandrois and E.D. Chasseau, *Acta. Cryst.* **B33**, 2744 (1977).

72. J.S. Chapell, A.N. Bloch, W.A. Bryden, and A.J. Heeger, *Phys. Rev. B* **13**, 3381 (1976).

73. D.B. Chestnut, *J. Chem. Phys.* **40**, 405 (1964).

74. H.M. McConnell, in *Molecular Biophysics*, B. Pullman and M. Weissbluth, eds., (Academic Press, New York, 1965).

75. A. Brau, P. Breüsch, J.P. Farges, W. Hinz, and D. Kuse, *Phys. Status Solidi* **B62**, 615 (1974).

76. D.B. Tanner, J.E. Deis, A.J. Epstein, and J.S. Miller, *Solid State Comm.* **31**, 671 (1979).

77. K.D. Cummings, D.B. Tanner, and J.S. Miller, *Phys. Rev. B* **24**, 4142 (1981).

78. D.B. Tanner, C.S. Jacobsen, A.A. Bright, and A.J. Heeger, *Phys. Rev. B* **16**, 3283 (1977).

79. J. Tanaka, M. Tanaka, T. Kawai, T. Takabe, and O. Maki, *Bull. Chem. Soc. Jap.* **49**, 2358 (1976).

80. R.P. McCall, D.B. Tanner, J.S. Miller, and A.J. Epstein, *Phys. Rev. B* **35**, 9209 (1987).

81. M.J. Rice, L. Pietronero, and P. Brüesch, *Solid State Commun.* **21**, 757 (1977).

82. A. Painelli, A. Girlando and C. Pecile, *Solid State Commun.* **52**, 801 (1984).

83. N.O. Lipari, M.J. Rice, C.B. Duke, R. Bozio, A. Girlando, and C. Pecile, *Int. J. Quant. Chem.* **11**, 583 (1977).

84. R Świetlik and A. Graja, *J. Physique* **44**, 617 (1983).

85. A. Graja, P.V. Huong, and J.C. Cornut, *Solid State Comm.* **39**, 929 (1981).

86. R.J.J. Visser, S. van Smaalen, J.L. de Boer, and A. Vos, *Mol. Cryst. Liq. Cryst.* **120**, 167 (1985).

87. T. Sundaresan and S.C. Wallwork, *Acta. Cryst.* **B28**, 1163 (1972).

88. G. Rindorf, N. Thorup, and K.Kamarás, *Synth. Met.* **25**, 189 (1988).

89. R.J.J. Visser, J.L. de Boer, and A. Vos, *Acta. Cryst.* **C46**, 864 (1990).

90. P. Kamminga and B. van Bodegom, *Acta. Cryst.* **B37**, 114 (1981).

91. F. Rachdi, T. Nunes, M. Ribet, P. Bernier, M. Helme, M. Mehring, and M. Almeida, *Phys. Rev. B., accepted.*

92. G. Zimmer, A.C. Kolbert, F.Rachdi, P. Bernier, M. Almeida, and M. Mehring, *Phys. REv. B., accepted.*

93. G. Zimmer, A.C. Kolbert, F. Rachdi, P. Bernier, M. Almeida, and M. Mehring,

94. S.K. Khanna, A.A. Bright, A.F. Garito, and A.J. Heeger, *Phys. Rev. B* **10**, 2139 (1974).

95. M. Konno, T. Ishii, and Y. Saito, *Acta. Cryst.* **B33**, 763 (1977).

96. A. Hoekstra, T. Spoelder, and A. Vos, *Acta. Cryst.* **B28**, 14 (1972).

97. M. Konno and Y. Saito, *Acta. Cryst.* **B30**, 1294 (1974).

98. M. Konno and Y. Saito, *Acta. Cryst.* **B31**, 2007 (1975).

99. J.G. Vetger, T. Hibma, and J. Kommandeur, *Chem. Phys. Lett.* **3**, 427 (1969).

100. N. Sakai, I. Shirotani, and S. Minomura, *Bull. Chem. Soc. Jpn.* **45**, 3321 (1972).

101. J.G. Vetger and J. Kommandeur, *Mol. Cryst. Liq. Cryst.* **30**, 11 (1975).

102. N. Watanabe, Y. Iwasa, and T. Koda, *Phys. Rev. B* **44**, 11111 (1991).

103. S. Hiroma, H. Kuroda, and H. Akamatu, *Bull. Chem. Soc. Jpn.* **44**, 9 (1971).

104. C. Carlone, R. Laidig, E. Kisela, and N.K. Hota, *Solid State Comm.* **37**, 253 (1981).

105. K. Yakushi, T. Kusaka, and H. Kuroda, *Chem. Phys. Lett.* **68**, 139 (1979).

106. K. Yakushi, S. Miyajima, and H. Kuroda, *Chem. Phys. Lett.* **114**, 168 (1985).

107. G.R. Anderson and J.P. Devlin, *J. Phys. Chem.* **79**, 1100 (1975).

108. Z. Iqbal, C.W. Christoe, and D.K. Dawson, *J. Chem. Phys.* **63**, 4485 (1975).

109. R. Bozio and C. Pecile, *J. Chem. Phys.* **67**, 3864 (1977).

110. R. Bozio, I. Zanon, A. Girlando and C. Pecile, *J. Chem. Soc. (Faraday Trans. II)* **74**, 235 (1978).

111. A. Girlando, R. Bozio and C. Pecile, *Chem. Phys. Lett.* **25**, 409 (1974).

112. C.K. Chi and E.R. Nixon, *Spectrochimica Acta.* **31A**, 1739 (1975).

113. K.D. Truong and C. Carlone, *Phys. Rev. B* **20**, 2238 (1979).

114. A.D. Bandrauk, K.D. Truong, and S. Jandl, *Can. J. Chem* **60**, 1881 (1982).

115. Y. Takaoka and K. Motizuki, *J. Phys. Soc. Jpn.* **47**, 1752 (1979).

116. Y. Lépine, A. Caillé, and V. Larochelle, *Phys. Rev. B* **18**, 3585 (1978).

117. Y. Lépine, *Phys. Rev. B* **28**, 2659 (1983).

118. M. Uchigoshi, K. Tsutsi, and S. Furukawa, *Jpn. J. Appl. Phys.* **30**, L444 (1991).

119. S.Yamaga, *Jpn. J. Appl. Phys.* **30**, 437 (1991).

120. M. Isshiki, T. Itoga, K. Masumoto, K. Mochisuki, and W. Uchida, *Jpn. J. Appl. Phys.* **30**, 623 (1991).

121. V. Gridin, C. Casl, J.D. Comins, and R. Beserman, *J. Appl. Phys.* **71**, 6069 (1992).

122. T. Kimoto, H. Nishino, T. Ueda, A. Yamashita, and H. Matsunami, *Jpn. J. Appl. Phys.* **30**, L289 (1991).

123. T. Minami, T. Miyata, S. Takata, and I. Fukuda, *Jpn. J. Appl. Phys.* **30**, L117 (1991).

124. K. Onisawa, Y. Abe, T. Nakayama, and M. Hanazono, *Jpn. J. Appl. Phys.* **30**, 314 (1991).

125. L.T. Canham, *Appl. Phys. Lett.* **57**, 1046 (1990).

126. C. Adachi, S. Tokito, and S. Saito, *Jpn. J. Appl. Phys.* **27**, L269 (1988).

127. C. Adachi, T. Tsutsui and S. Saito, *Appl. Phys. Lett.* **56**, 799 (1990).

128. M. Uchida, Y. Ohmori, and K. Yoshino, *Jpn. J. Appl. Phys.* **30**, L2104 (1991).

129. H. Masui and M. Takeuchi, *Jpn. J. Appl. Phys.* **30**, L864 (1991).

130. W.J. Feast, I.S. Millichamp, R.H. Friend, M.E. Horton, D. Phillips, S.D.D.V. Rughooputh, and G. Rumbles, *Synth. Met.* **10**, 181 (1985).

131. Z. Vardeny, E. Ehrenfreund, O. Brafman, M. Nowak, H. Schaffer, A.J. Heeger, and F. Wudl, *Phys. Rev. Lett.* **56**, 671 (1986).

132. J.J. Aaron, S. Aeiyach, and P.C. Lacaze, *J. of Lumin.* **42**, 57 (1988).

133. R.F. Mahrt and H. Bassler, *Synth. Met.* **45**, 107 (1991).

134. H.S. Woo, O. Lhost, S.C. Graham, D.C.C. Bradley, R.H. Friend, C. Quattrochi, and J.L. Brédas, *J. Chem. Phys., submitted.*

135. H.S. Woo, S.C. Graham, D.A. Halliday, D.C.C. Bradley, R.H. Friend, P.L. Burn, and A.B. Holmes, *Phys. Rev. B, submitted.*

136. J. Poplawski and E. Ehrenfreund in *Electronic Properties in Conjugated Polymers III*, Spring Series in Solid State Sciences, Vol. 91, H. Kuzmany, M. Mehring, and S. Roth, eds., (Springer–Verlag, Heidelberg, 1989).

137. G. Leising, K. Pichler, and F. Stelzer in *Electronic Properties in Conjugated Polymers III*, Spring Series in Solid State Sciences, Vol. 91, H. Kuzmany, M. Mehring, and S. Roth, eds., (Springer–Verlag, Heidelberg, 1989).

138. G. Leising, O. Leitner, F. Aldrain, and H. Kahlert, *Synth. Met.* **17**, 635 (1987).

139. S. Zalis and M. Kertesz, *Synth. Met.* **47**, 179 (1992).

140. M.S. Kiani and G.R. Mitchell, *Synth. Met.* **46**, 293 (1992).

141. P.L. Burn, A.B. Holmes, A. Kraft, D.D.C. Bradley, A.R. Brown, R.H. Friend, and R.W. Gymer, *Nature* **356**, 47 (1992).

142. C. Adachi, T. Tsutsui, and S. Saito, *Appl. Phys. Lett.* **55**, 1489 (1989).

143. J. Littman and P. Martic, *J. Appl. Phys.* **72**, 1957 (1992).

144. C. Adachi, T. Tsutsui, and S. Saito, *Appl. Phys. Lett.* **56**, 799 (1989).

145. C.W. Tang, S.A. VanSlyke, and C.H. Chen, *Appl. Phys. Lett.* **65**, 3610 (1989).

146. Y. Cao, G.M. Treacy, P. Smith, and A.J. Heeger, *Appl. Phys. Lett.* **60**, 2711 (1992).

147. D. Moses, *Appl. Phys. Lett.* **60**, 3215 (1992).

148. J. Ruiz and J.R. Reynolds, *unpublished results.*

149. M. Pomeranz and J. Wang, *unpublished results.*

150. O. Inganas, M. Sundberg, G. Gustafsson, J.O. Nilsson, S. Stafstrom, and B. Sjogren in *Electronic Properties in Conjugated Polymers III*, Spring Series in

Solid State Sciences, Vol. 91, H. Kuzmany, M. Mehring, and S. Roth, eds., (Springer–Verlag, Heidelberg, 1989).

151. M. Logdlund, R. Lazzaroni, W.R. Salaneck, S. Stafstrom, J.O. Nilsson, X. Shuang, J.E. Osterholm, and J.L. Brédas in *Electronic Properties in Conjugated Polymers III*, Spring Series in Solid State Sciences, Vol. 91, H. Kuzmany, M. Mehring, and S. Roth, eds., (Springer–Verlag, Heidelberg, 1989).

152. J.P. Ruiz, J.R. Dharia, J.R. Reynolds, and L.J. Buckley, *Macromolecules* **25**, 849 (1992).

153. R.J. Bell, *Introductory Fourier Transform Spectroscopy*, (Academic Press, New York, 1972).

154. R.L. Henry and D.B. Tanner, *Infrared Phys.* **19**, 163 (1979).

155. D.B. Tanner and R.P. McCall, *Applied Optics* **23**, 2363 (1984).

156. C.D. Porter and D.B. Tanner, *Intern. J. Infrared and Millimeter Waves* **4**, 273 (1983).

157. K.D. Cummings, Ph.D. Dissertation, The Ohio State University, Columbus, OH. (1981).

158. E.D. Palik and J.R. Stevenson, *NRL Report 6177*, U.S. Navel Research Laboratory, (1964).

159. M. Almeida, L. Alcácer, *J. Cryst. Growth* **62**, 183 (1985).

160. M. Almeida, L. Alcácer, and A. Lindegaared-Andersen, *J. Cryst. Growth* **72**, 567 (1985).

161. F. Wooten, *Optical Properties of Solids*, (Academic Press, New York, 1972).

162. J.I. Pankove, *Optical Processes in Semiconductors*, (Dover Publications, Inc., New York, 1971).

163. Y. Iida, *Bull. Chem. Soc. Jap.* **42**, 637 (1969).

164. A. Girlando and C. Pecile, *Spectrochim. Acta.* **A29**, 1859 (1975).

165. R. Bozio, I. Zanon, A. Girlando, and C. Pecile, *J. Chem. Soc. Faraday Trans. II* **74**, 235 (1978).

166. M.J. Rice, V.M. Yartsev, and C.S. Jacobsen, *Phys. Rev. B* **21**, 3437 (1980).

167. V.M. Yartsev and C.S. Jacobsen, *Phys. Rev. B* **24**, 6167 (1981).

168. V. Železný, J. Petzelt, and R. Šwietlik, *Phys. Stat. Sol.* **B140**, 595 (1988).

169. M.V. Belousov, A.M. Vainrub, and R.M. Vlasova, *Fiz. tverd.* **18**, 2637 (1976).

170. R. Šwietlik and A. Graja, *J. Physique* **44**, 617 (1983).

171. K. Kamarás, C.S. Jacobsen, V. Železný, J.L. Musfeldt, and D.B. Tanner, *Synth. Met.* **42**, 1839 (1991).

172. R.P. McCall, D.B. Tanner, J.S. Miller, A.J. Epstein, I.A. Howard, and E.M. Conwell, *Mol. Cryst. Liq. Cryst.* **120**, 59 (1985).

173. R.P. McCall, D.B. Tanner, J.S. Miller, A.J. Epstein, I.A. Howard, and E.M. Conwell, *Synth. Met.* **11**, 231 (1985).

174. E.M. Conwell and I.A. Howard, *Phys. Rev. B* **31**, 7835 (1985).

175. E.M. Conwell and I.A. Howard, *Synth. Met.* **13**, 71 (1986).

176. A.J. Epstein, R.W. Bigelow, J.S. Miller, R.P. McCall, and D.B. Tanner, *Mol. Cryst. Liq. Cryst.* **120**, 43 (1985).

177. A.N. Bloch, R.B. Weisman, and C.M. Varma, *Phys. Rev. Lett.* **28**, 753 (1972).

178. A.J. Epstein, E.M. Conwell, D.J. Sandman, and J.S. Miller, *Solid State Comm.* **23**, 355 (1977).

179. A.J. Epstein, E.M. Conwell, D.J. Sandman, and J.S. Miller, *Solid State Comm.* **24**, 627 (1977).

180. R. Bozio and C. Pecile, *Solid State Comm.* **37**, 193 (1981).

181. R. Bozio and C. Pecile, *J. Phys. C* **13**, 6205 (1980).

182. R.H. Boyd and W.D. Phillips, *J. Chem. Phys.* **43**, 2927 (1965).

183. R. Bozio, A. Girlando, and C. Pecile, *J. Chem. Soc. Faraday Trans. II* **71**, 1237 (1975).

184. C.S. Jacobsen, D.B. Tanner, and K. Bechgaard, *Phys. Rev. B* **28**, 7019 (1983).

185. E.B. Wilson, Jr., J.C. Decius, and P.C. Cross, *Molecular Vibrations: The Theory of Infrared and Raman Vibrational Spectra,* (Dover Publications, Inc., New York, 1955).

186. F.A. Cotton, *Chemical Applications of Group Theory, 2nd Ed.*, (John Wiley and Sons, Inc., New York, 1971).

187. R. Bozio, A. Girlando, and C. Pecile, *J. Chem. Soc. Faraday Trans. II* **71**, 1237 (1975).

188. R. Bozio, A. Girlando, and C. Pecile, *J. Chem. Soc. Faraday Trans. II* **74**, 235 (1978).

189. H. Gutfreund and M. Weger, *Phys. Rev. B* **16**, 1753 (1977).

190. H. Morawitz, *Phys. Rev. Lett.* **34**, 1096 (1975).

191. F.E. Bates, J.E. Eldridge, and M.R. Bryce, *Can. J. Phys.* **59**, 339 (1981).

192. C.J. Fritchie, *Acta. Cryst.* **20**, 892 (1966).

193. K. Fesser, A.R. Bishop, and D.K. Campbell, *Phys. Rev. B* **27**, 4804 (1983).

194. J.L. Brédas, and H. Kuzmany in *Electronic Properties in Conjugated Polymers III*, Spring Series in Solid State Sciences, Vol. 91, H. Kuzmany, M. Mehring, and S. Roth, eds., (Springer–Verlag, Heidelberg, 1989).

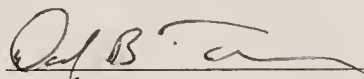195. B. Tian, G. Zerbi, R. Schenk, and K. Mullen, *J. Chem. Phys.* **95**, 3191 (1991).

BIOGRAPHICAL SKETCH

Janice Lynn Musfeldt was born on Easter Sunday in 1965. She has spent most of her life living in the suburbs of Chicago, where she attended primary and secondary school. In 1983, she entered the University of Illinois in Urbana-Champaign to pursue a degree in chemical engineering. In Prof. P.H. Geil's group, she worked on several projects, including the viscoelastic behavior of PEEK and the effect of water adsorption on the glass transition temperature in J2 copolymer.

Jan is happy to finally complete her doctoral studies at the University of Florida in Gainesville. In the future, she hopes to continue and expand upon her work in the field of infrared, optical and luminescent properties of novel materials. She is going to miss her research group very, very much.
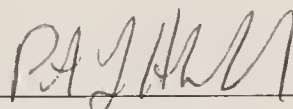
Jan has many diverse interests, including her husband (whom she does not see very often due to his own research interests), classical music and classical music performance, Renaissance art, travel, cooking, tennis and aerobic dance. She has not had the time or money to pursue most of these things in the past five and a half years, as she has been busy in the lab.

I certify that I have read this study and that in my opinion it conforms to acceptable standards of scholarly presentation and is fully adequate, in scope and quality, as a dissertation for the degree of Doctor of Philosophy.

David B. Tanner, Chairman
Professor of Physics and Chemistry

I certify that I have read this study and that in my opinion it conforms to acceptable standards of scholarly presentation and is fully adequate, in scope and quality, as a dissertation for the degree of Doctor of Philosophy.

Peter J. Hirshfeld
Assistant Professor of Physics

I certify that I have read this study and that in my opinion it conforms to acceptable standards of scholarly presentation and is fully adequate, in scope and quality, as a dissertation for the degree of Doctor of Philosophy.
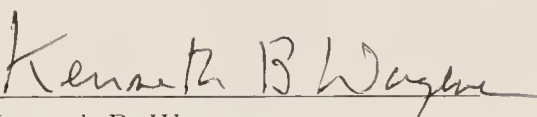
Willis B. Person
Professor of Chemistry

I certify that I have read this study and that in my opinion it conforms to acceptable standards of scholarly presentation and is fully adequate, in scope and quality, as a dissertation for the degree of Doctor of Philosophy.

Martin T. Vala
Professor of Chemistry

I certify that I have read this study and that in my opinion it conforms to acceptable standards of scholarly presentation and is fully adequate, in scope and quality. as a dissertation for the degree of Doctor of Philosophy.

Kenneth B. Wagener
Professor of Chemistry

This dissertation was submitted to the Graduate Faculty of the Department of Chemistry in the College of Liberal Arts and Sciences and to the Graduate School and was accepted as partial fulfillment of the requirements for the degree of Doctor of Philosophy.

December 1992

_____
Dean, Graduate School